Manufacturing of a Fiber-Reinforced Thermoplastic Composite Micro-Generating Wind Turbine Blade

by

Milos Zivkovic

A thesis
presented to the University of Waterloo
in fulfillment of the
thesis requirement for the degree of
Master of Applied Science
in
Mechanical and Mechatronics Engineering

Waterloo, Ontario, Canada, 2023

© Milos Zivkovic 2023

Author’s Declaration

I hereby declare that I am the sole author of this thesis. This is a true copy of the thesis, including any required final revisions, as accepted by my examiners.

I understand that my thesis may be made electronically available to the public.

Abstract

In response to climate legislation attempting to curb global greenhouse emissions, renewable energy technologies have seen rapidly increasing global demand over the past two decades, with significant attention paid to the wind energy sector. Large, MW-scale wind turbines routinely exceed 100-meters in blade length, enabling reliable clean energy to be accessed by urban communities. However, such structures are often not feasible in remote communities that are not connected to the electrical grid. In Northern Canada, these communities are often reliant on diesel generators for reliable energy despite their inefficiency and emission of harmful pollutants. Thus, the development of renewable energy solutions that can be applied to smaller communities – such as small-scale, micro-generating wind turbine blades that produce up-to 100 KW of power – are a timely engineering problem.

Generally, high-performance blade structures take advantage of fiber-reinforced plastic (FRP) composite materials that allow for high strength-to-weight ratios and excellent fatigue performance. However, legacy turbine blade material systems suffer from poor end-of-life recyclability due to issues with recovering conventional thermosetting epoxy polymer resin systems that cannot be melted and reformed. Thus, the composites industry is rapidly transitioning to alternate plastic formulations that maximize performance while considering holistic product lifecycles. In-situ polymerizable thermoplastic resins represent one such alternative. These novel resin systems comprise monomers that polymerize in-situ during part production. The low flow viscosity of these resins enables their use with cost-effective processes such as vacuum assisted resin-transfer molding (VARTM). Unlike thermosetting polymers (such as epoxy) that undergo irreversible curing during processing, thermoplastic materials can be melted and reformed at sufficiently high temperatures, allowing for full reclamation of the composite material system at the conclusion of its service life.

The goal of this thesis was to manufacture a full-scale micro-generating wind turbine blade comprising glass-fiber reinforced in-situ polymerizable thermoplastic resin shells using a VARTM process in a cost-effective manner. Three main objectives were identified to complete this project. The first objective was to optimize a baseline VARTM process to reliably produce flat panels with optimized fiber volume fraction (V_f) and void volume fraction (V_c). Second, a suitable adhesive joining system for the composite was to be identified, with Mode I double cantilever beam and

Mode II end notched flexural tests performed at room and low temperatures to simulate the expected ambient conditions in remote Northern Canadian communities, with a consideration for bond-line thickness effects. Finally, the findings from the first two tasks were to be synthesized and adapted to enable the production of full-scale, high-quality micro-generating wind turbine blades by joining two separately produced shells.

A process study was performed to minimize void formation during flat panel manufacturing stemming from transverse flow, dual-scale flow, and race-tracking, while maintaining sufficient compaction during polymerization. Microscopic analysis and visual inspection were used to measure fiber volume fraction and observe void formations. The optimized high-quality panels exhibited an average fiber volume fraction of 46.28 (±1.2)%. The removal of a polymeric veil from the unidirectional non-crimp fabric architecture contributed to an increase in fiber volume fraction of 8.2%. The observed fiber volume fractions with the optimized VARTM process are within 2.5% of literature results for E-glass UD-NCF composite panels produced with SCRIMP processes. Adhesive test results showed that the methyl methacrylate (MMA) adhesive experienced ductile cohesive failure at room temperature (RT; 23°C), and brittle failure within the adhesive and substrate at low temperature (LT; -40°C) depending on the load condition. RT DCB tests showed an increase of 45% in fracture energy in the adhesive joint with increasing bond-line thickness, while LT test specimens exhibited lower loads and an oscillatory crack tip propagation pattern implying accumulated residual stresses in the adhesive layer due to thermal expansion incompatibility with the composite substrate. ENF specimens showed a reduced load capability at LT conditions with a higher elastic stiffness and failure within the substrate.

Fabrication of a full-scale proof-of-concept blade showed that accommodating fabric drapability was critical for a high-quality infusion, and that the material system can be successfully adapted for production pending revisions to the adhesive surface geometries.While the trailing edge of the blade allowed for a robust adhesive joint, the blade shell concavities along the leading edge meant that the shells mated along the thickness of the composite, creating a weak bond with significant cracks and porosities in the adhesive layer. Future trials should incorporate a representative fabric stacking sequence (instead of the $[0_4]$ layup used for the proof-of-concept blade) and modified joint geometries to compare the static deflection of the updated thermoplastic material system with legacy carbon fibre-reinforced epoxy composite blades.

Acknowledgements

I would like to extend my sincerest gratitude to Professor John Montesano and the Composites Research Group (CRG) for giving me the opportunity to join the team as an Undergraduate Research Assistant in 2020 and subsequently welcoming me back as an MASc student with a challenging industrially applicable research project. His guidance and feedback throughout my work has been invaluable in my development as a researcher and engineer, and the opportunity to present at conferences and travel abroad for workshop opportunities has broadened my horizons and ambitions.

I would like to thank my industrial sponsors at Borrum Energy Solutions for giving me the opportunity to work on a substantive and innovative wind energy project for my MASc degree. I would also like to thank the National Science and Engineering Research Council of Canada (NSERC) and the Ontario Center of Innovation (OCI) for providing funding for this project, and Bostik SA, Johns Manville, and SAERTEX GmbH & Co.KG for the kind donation of material and supplies for my experiments.

Special thanks are also given to Professors Duane Cronin and Michael Worswick for allowing me to use the equipment in the Forming & Crash Lab, Professor Hamid Jahed for allowing me to access the Fatigue and Stress Analysis Lab, and Professor Marco Alfano for his insight and guidance during many of my experimental trials. My sincere thanks to the technicians and engineers throughout the engineering faculty at the University of Waterloo, including Tom Gawel, James Farnsworth, Eckhard Budziarek, Richard Morrison, and the machinists in the EMS and ESMS (with special appreciation extended to Andrew Urschel, who has been a mentor to me since my undergraduate studies), for their time, expertise, and help with all my questions and queries.

To my friends and colleagues at the CRG, including Valerie Ajayi, Ramin Dehaghani, Mehdi Ghazimoradi, Devon Hartlen, Ben Harvey, Sanaz Hashemi, Zohreh Mohammadi, Renan Portela, Khizar Rouf, Farzad Sharifpour, Victor Shi, Aaditya Suratkar, and Yu Zeng, thank you for brightening my day each time I am in the office, and for our constructive and detailed discussions during each of our group meetings. Thank you to Ramin and Devon for your help with training and insight into lab processes, and a very special thanks to Victor, with whom I have shared this project from the start and who has selflessly helped me throughout my research tasks.

This thesis has been the culmination of 7 years spent at the University of Waterloo starting with my BASc degree, and I would like to thank my family and friends for supporting me unconditionally throughout my academic career. To my parents, Lora and Louis, and my brothers, Lazar and Aleksandar, thank you from the bottom of my heart for your love and patience on this journey.

Table of Contents

Author's Declaration ..... **ii**

Abstract ..... **iii**

Acknowledgements ..... **v**

List of Figures ..... **xi**

List of Tables ..... **xiv**

Chapter 1: Introduction **1**

1.1. Research Motivation 1

1.2. Research Objectives 5

1.3. Outline of Thesis 6

Chapter 2: Background and Literature Review **7**

2.1. Composite Materials 7

2.1.1. Matrix Systems 7

2.1.2. Fiber Reinforcement 9

2.2. Composites Manufacturing 11

2.2.1. Darcy's Law 13

2.2.2. Conventional VARTM Processes 16

2.2.3. VARTM Process Variants 22

2.3. Adhesive Joining 28

2.3.1. Adhesive Systems 28

2.3.2. Adhesive Joint Failure Modes 30

2.3.3. Effect of Bond-line Thickness on Adhesive Performance 35

2.3.4. Effect of Temperature on Thermoplastic Adhesive Performance 35

2.4. Wind Turbine Blade Manufacturing 37

2.4.1. VARTM Processes for Wind Turbine Blades 37

2.4.2. Thermoplastic FRP Composites in Wind Turbine Blade Applications 39
2.4.3. Wind Turbine Blade Assembly 40
Chapter 3: Flat Panel VARTM Processing 42
3.1. Panel Materials 42
3.1.1. Resin System 42
3.1.2. Fiber Reinforcement 43
3.2. Flat Panel Manufacturing – Baseline VARTM Process 44
3.2.1. Mold Preparation 44
3.2.2. Vacuum Infusion Supplies Preparation – Material Stack 44
3.2.3. Vacuum Infusion Supplies Preparation – Infusion Lines 45
3.2.4. Laminate Layup 45
3.2.5. Application of Vacuum Bag 46
3.2.6. Resin Mixing 47
3.2.7. Resin Infusion and In-Situ Polymerization 48
3.2.8. Panel Demolding and Mold Cleaning 48
3.2.9. Baseline Panel Quality 48
3.3. Flat Panel Manufacturing – VARTM Process Improvements 49
3.3.1. Vacuum Pump Test 50
3.3.2. Flow Rate Test 50
3.3.3. Degassing Chamber 52
3.3.4. Resin Reservoir 53
3.3.5. Line Inlet vs. Point Inlet 54
3.3.6. Distribution Mesh Adjustments 56
3.3.7. Vacuum Bag Pleats 58
3.3.8. Caul Plate Trials 61

3.3.9. Summary of Optimized VARTM Setup 64
3.4. High-Quality Panel Characterization 66
3.4.1. Void Assessment 67
3.4.2. Fiber Volume Fraction Assessments via Microscope Analysis 67
Chapter 4: Adhesive Joint Testing 70
4.1. Specimen Preparation and Test Setup 70
4.1.1. Specimen Preparation 71
4.1.2. Experimental Setup 73
4.1.3. Climate Chamber Setup – Low Temperature 75
4.1.4. Mode-I SERR Data Reduction Scheme 76
4.1.5. Mode-II SERR Data Reduction Scheme 79
4.2. DCB and ENF Test Results 81
4.2.1. DCB Test Results 81
4.2.2. ENF Test Results 84
4.2.3. Comparative Epoxy Adhesive DCB Tests 86
4.3. Fracture Surface Analysis 88
4.3.1. RT DCB Specimens 88
4.3.2. LT DCB Specimens 88
4.3.3. RT ENF Specimens 92
4.3.4. LT ENF Specimens 92
4.4. RT DCB Test Simulations 94
Chapter 5: Turbine Blade Manufacturing 97
5.1. Blade Shell Mold Modification 97
5.2. Blade Shell Processing 98
5.2.1. Vacuum Infusion Materials Setup 101

5.2.2. Blade Shell Vacuum Bagging 104
5.2.3. Resin Mixing and Infusion 105
5.2.4. Demolding and Cleaning 105
5.2.5. Trimming and Post-Processing 105
5.3. Blade Shell Process Overview 106
5.4. Blade Shell Assessment 107
5.5. Blade Bonding and Post-Processing 108
5.6. Blade Shell Bonding Results 109
Chapter 6: Discussion 112
6.1. Flat Panel VARTM Processing 112
6.2. Adhesive Testing 113
6.3. Blade Manufacturing 114
Chapter 7: Conclusions 116
7.1. Recommendations for Future Work 117
References 119
Appendix A1 134
Appendix A2 136
Appendix A3 138

List of Figures

Figure 1.1: Roadmap for supporting energy projects 2
Figure 1.2: Projected annual waste from decommissioned composite wind turbine blades 3
Figure 2.1: General schematic of the addition polymerization process 8
Figure 2.2: Comparison between unidirectional non-crimp fabric and woven fabric 10
Figure 2.3: Schematic of unidirectional non-crimp fabric 10
Figure 2.4: Generalized VARTM procedure 12
Figure 2.5: Schematic of conventional VARTM process 16
Figure 2.6: Transverse flow phenomenon 18
Figure 2.7: Dual scale flow phenomenon 19
Figure 2.8: Race-tracking effect 20
Figure 2.9: Resin starvation during VARTM processing 21
Figure 2.10: Comparison of VARTM variants 22
Figure 2.11: Schematic of VARTM process with dynamic pressure chamber 26
Figure 2.12: Summary of stress state conditions for adhesive joints 31
Figure 2.13: Adhesive joint failure modes 32
Figure 2.14: Fracture mechanics failure modes 33
Figure 2.15: DCB and ENF specimen schematics 34
Figure 2.16: Bilinear traction-separation law 34
Figure 2.17: Temperature effect on polyurethane (thermoplastic) adhesive performance at quasi-static loading conditions 36
Figure 2.18: Cross-section of generic wind turbine blade 37
Figure 2.19: Virtual process chain that can be applied to VARTM optimization 38
Figure 2.20: VARTM layout for small-scale wind turbine blade 39
Figure 2.21: Adhesive joint configurations 41
Figure 3.1: Dimensions of E-glass UD-NCF 43
Figure 3.2: Baseline VARTM setup 47
Figure 3.3: Panels produced via baseline VARTM setup 49
Figure 3.4: Weak vacuum pump trial 50
Figure 3.5: Flow rate trials 52
Figure 3.6: Degassing chamber trial 53

Figure 3.7: Resin reservoir trial 54
Figure 3.8: Line infusion setup trials 56
Figure 3.9: Distribution mesh setup trial 58
Figure 3.10: Order of operations during pleated flat panel vacuum bag preparation 59
Figure 3.11: Pleat *A* technique 60
Figure 3.12: Pleat *B* technique 60
Figure 3.13: Vacuum bag before and after wrinkle adjustment 61
Figure 3.14: Oversized caul plate trial 62
Figure 3.15: Undersized caul plate trial 63
Figure 3.16: Panel produced with optimized VARTM process 66
Figure 3.17: High-quality panel void assessment 67
Figure 3.18: High-quality panel volume fraction assessment 69
Figure 4.1: Microscopic bond-line thickness measurement for bonded specimen 72
Figure 4.2: Test frame grip fixture with DCB specimen 74
Figure 4.3: 3-Point Bend fixture with ENF specimen 75
Figure 4.4: DSLR camera setup for adhesive testing 76
Figure 4.5: Schematic of "Δ" calibration parameter for the Modified Beam Theory 77
Figure 4.6: Crack tip following algorithm demonstration 78
Figure 4.7: Progression of ductile process zone 79
Figure 4.8: Problems with crack tip identification during ENF testing 80
Figure 4.9: Strain field monitoring of ENF samples 81
Figure 4.10: Load-Displacement curves of RT and LT DCB specimens 82
Figure 4.11: Overlay of average Load-Displacement curves for DCB tests at RT and LT 83
Figure 4.12: Load-Displacement curves of RT and LT ENF specimens 85
Figure 4.13: Overlay of average Load-Displacement curves for ENF tests at RT and LT 86
Figure 4.14: Simultaneous interfacial failure between both thermoplastic FRP substrates and epoxy adhesive 87
Figure 4.15: Interfacial failure between epoxy adhesive and thermoplastic FRP substrate 87
Figure 4.16: Ductile fracture surface of RT DCB specimens 88
Figure 4.17: Fracture surface analysis of LT DCB specimens 89
Figure 4.18: 3D depth display for LT DCB adhesive fracture surfaces 90

Figure 4.19: 3D depth display for RT DCB adhesive fracture surfaces 91
Figure 4.20: Comparison of un-bonded fracture surface with adhesive fracture surface for LT DCB specimen 92
Figure 4.21: Fracture surface analysis of RT ENF specimens at low magnification 92
Figure 4.22: Fracture surface of LT ENF specimens 93
Figure 4.23: Meshed DCB model 94
Figure 4.24: RT DCB experimental results vs. numerical simulation 96
Figure 5.1: Blade shell mold overview with measurements 98
Figure 5.2: Schematic of full-scale turbine blade shell infusion setup 100
Figure 5.3: Fabric cutting and ply staggering for drapeability 102
Figure 5.4: Fabric and peel ply layup setup 103
Figure 5.5: Distribution mesh and infusion line layouts 104
Figure 5.6: Blade shell after trimming and sanding 106
Figure 5.7: Comparison between poor- and high-quality blade shell root 108
Figure 5.8: Bonded micro-generating wind turbine blade 109
Figure 5.9: Comparison between the bonding surfaces for trailing edge and leading edge 110
Figure 5.10: Defects observed during adhesive joining of micro-generating wind turbine blade shells 111
Figure A3.1: Regions of the blade with poor adhesive joining surface geometries 138
Figure A3.2: Solution #1 to improve the leading-edge bonding surfaces 139
Figure A3.3: Solution #2 to improve the leading-edge bonding surfaces 140
Figure A3.4: Solution #3 to improve the leading-edge bonding surfaces 141

List of Tables

Table 3-1: Mechanical properties of polymerized Elium® 188 polymer 42
Table 3-2: E-glass UD-NCF technical specifications 43
Table 3-3: Overview of adopted VARTM parameters for optimized setup 64
Table 3-4: Summary of additional VARTM process optimization trials 65
Table 3-5: Comparison of volume fractions for FRP samples 69
Table 4-1: Non-veiled E-glass UD-NCF/Elium® panel properties 71
Table 4-2: DCB test specimen dimensions 73
Table 4-3: ENF test specimen dimensions 73
Table 4-4: G_{IC} calculations using MBT method for RT-DCB specimens 84
Table 4-5: Calibrated traction separation law parameters 95

Chapter 1: Introduction

1.1. Research Motivation

Driven by the need to reduce carbon emissions, there have been widespread global initiatives to transition from traditional fossil fuel energy sources to renewable technologies. Unfortunately, remote communities are often disconnected from the energy grid and may not receive the benefits of novel renewable energy solutions. Thus, remote communities in Canada are often reliant on diesel generators for reliable energy despite their expensive running costs and problems with pollution. In Canada, 218 remote communities rely on diesel generators, while only 18 rely on sustainable resources and remain susceptible to blackouts [1]. The Canadian Federal Government is actively investigating innovative energy solutions for Northern communities through the Clean Energy for Rural and Remote Communities (CERRC) program and has announced $300 million for funding in April 2022 through to 2027 [2]. The Pembina Institute estimates that similar policies enacted to limit diesel usage in remote communities have saved 12.3 million liters of oil per year between 2015 and 2020 [3]. This was nearly equal to the total oil saved over the preceding 40 years. Nonetheless, considering that remote Canadian communities are still reliant on approximately 682 million liters of oil annually, there is still significant room for emissions reduction. A roadmap for launching rural green energy initiatives provided by the Pembina Institute is shown in Figure 1.1 [3].

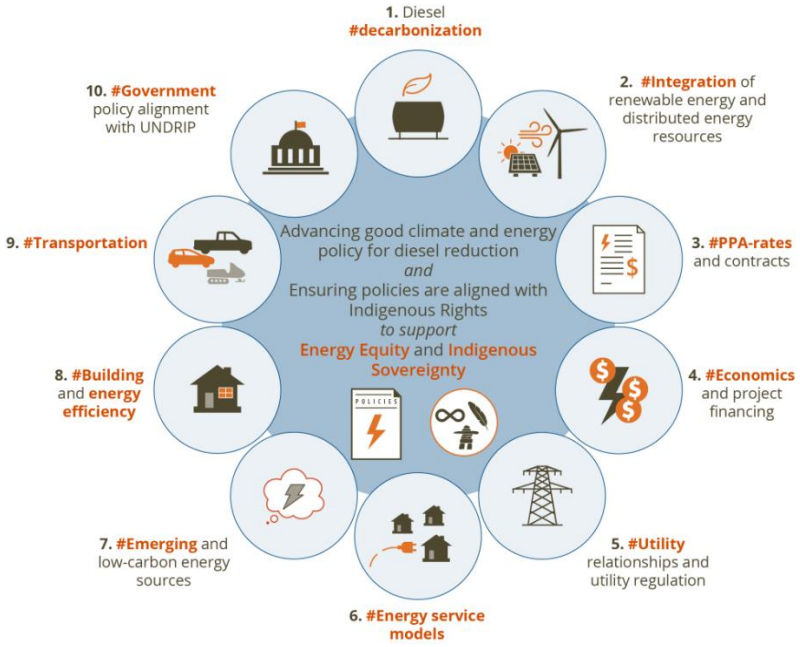


Figure 1.1: Roadmap for supporting energy projects and promoting diesel reduction in indigenous communities [3].

As part of the broader push towards renewable energy, the global wind energy sector has seen substantial growth during the past decade. In 2019, wind energy was responsible for around 9.0% of total energy production in the United States, and this number continues to trend upwards [4]. However, industrial-scale wind turbines find limited economic feasibility in small communities that are often hundreds of kilometers removed from neighboring towns and cities [2]. Multiple logistical challenges arise with large-scale turbines including difficulties with transporting the structures across country, assembling the structures on-site, and connecting the turbines to surrounding communities via the grid [1], [5]. Thus, localized energy installations that serve a single community at a time become a very practical alternative to large wind turbines. Borrum Energy Solutions is a Canadian company from Waterloo, Ontario that has developed a localized renewable energy generator in the form of their Anorra micro-generating wind turbine [5]. Micro-generating wind turbines generate between 20 W and 100 KW of power, compared to MW-scale power production that can be generated from large-scale wind turbines [6], [7]. A 1.5KW turbine produces sufficient power for a medium sized home and allows for market opportunities outside of remote communities such as rural cottages and farms. The Anorra turbines use blades between 1-2m in length depending on specification, allowing for easy transport and assembly in a wide range of environments [5].

While growth in the share of wind energy usage has alleviated some burdens on fossil fuel reliance, there remain ecological concerns associated with the end-of-life recyclability of traditional wind turbine blades. Typically, wind turbine blades are manufactured from glass or carbon fiber-reinforced plastic (FRP) composite materials comprising thermosetting resins (e.g., epoxy) using a vacuum infusion (VI) process [8], which are not readily recyclable. The projected annual composite waste from decommissioned wind turbine blades is expected to reach 50 million metric tons by 2050, as shown in Figure 1.2 [9].

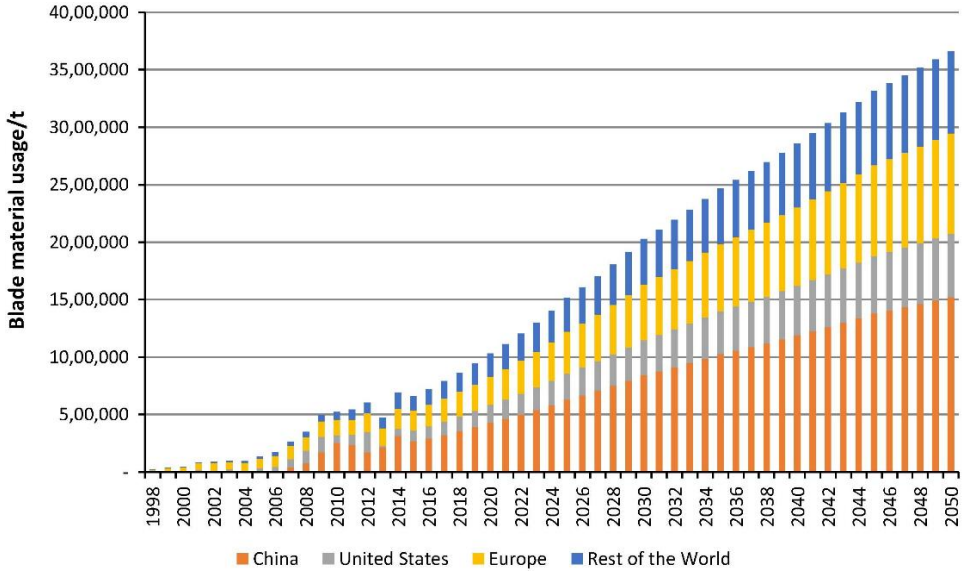


Figure 1.2: Projected annual waste from decommissioned composite wind turbine blades [9].

Currently, poor end-of-life recyclability is a necessary compromise from a performance standpoint since lightweight structural optimization increases blade efficiency. For large, industrial-scale blade structures, lowering the gravitational load becomes a key engineering requirement for good design [6]. With these considerations, a lightweight FRP composite that can be recycled is an ideal material for wind turbine blades. Contrary to epoxy-based composites that cure irreversibly by forming molecular cross-links, thermoplastics resins polymerize into structures that can be melted and re-formed at the end of their lifecycle [10]–[13]. Adding to these ecological benefits, thermoplastics demonstrate competitive mechanical properties in FRP applications. Specifically, fiber-reinforced thermoplastic resins have demonstrated superior tensile, flexural, and interlaminar shear properties, and improved fracture toughness when compared to equivalent fiber-reinforced thermosetting plastics, as well as improved fatigue

resistance in extreme cold environments – a common scenario in Northern Canadian communities [14], [15].

The Anorra blade is a candidate for a redesigned blade material system that leverages the recyclability and increased fracture toughness provided by thermoplastic polymer matrix systems. The Anorra blade has gone through multiple design and manufacturing iterations during the product development cycle, starting with a prepreg carbon fiber-reinforced polymer (CFRP) material system with an epoxy matrix and autoclave curing. The current iteration of the Anorra blade uses a vacuum infused (VI) carbon fiber/epoxy material system to reduce production costs. On the hierarchy of FRP materials, carbon fibers have the highest strength-to-weight ratio and are routinely used in high-performance applications [11], [13]. Comparatively, glass fibers have reduced performance, but their relatively low cost contribute to frequent usage in marine and non-structural vehicle body panel applications [12], [16]. Incorporating a thermoplastic matrix to increase the low temperature fatigue performance would partially offset the reduction in strength caused by a transition from carbon to glass fibers. Furthermore, micro-generating wind turbine blades experience smaller loads compared to large-scale installations, reducing the inherent strain on the material system [6]. However, conventional thermoplastics are not compatible with vacuum infusion processes.

A major advantage of reactive thermoplastic resin systems is their potential as a drop-in replacement for traditional epoxy resin systems from a manufacturing perspective [17], [18]. Low viscosity reactive thermoplastics can be used in vacuum assisted resin transfer molding (VARTM) processes, eliminating the need for presses and autoclaves and enabling the production of high-quality components. However, there are technical challenges designing fiber-reinforced thermoplastic composite blade shells, and the joining of the blade shell components may require a specialized methacrylate adhesive system due to the reduced surface energy of thermoplastic matrices compared to traditional thermosetting epoxies [19]. Thus, optimizing the blade assembly procedure must be considered in conjunction with the remaining manufacturing steps [20]. The implementation of a holistic manufacturing solution for a glass fiber thermoplastic resin system that can be applied to a micro-generating wind turbine blade is not trivial. Vacuum infusion process development must first include the reliable fabrication of flat-panel geometries before transferring the manufacturing techniques to full-scale blade shells. Concurrently, the testing and verification

of the adhesive joint at the expected operating conditions is also necessary to ensure that the projected benefits of the fracture toughness of the thermoplastic composite can be maximized in real use cases.

1.2. Research Objectives

The goal of this research project is to develop a holistic manufacturing process to completely fabricate a full-scale glass-fiber reinforced thermoplastic composite micro-generating wind turbine blade. Preliminary trials target the production of high-quality, flat composite panels, before applying the lessons learned from the flat panels to full-scale blade shells. Fully formed, high-quality shells will be bonded together with a suitable methacrylate adhesive to form the full-scale micro-generating wind turbine blade. The main objectives of this project are summarized below.

- Develop a reliable VARTM process for flat composite panels comprising glass fiber-reinforced thermoplastic constituents that yields high fiber volume fractions (V_f), low void volume fraction (V_c), and consistency between manufacturing trials.
- Develop a suitable adhesive joint for the glass fiber-reinforced thermoplastic composites. Assess fracture performance through Mode I and Mode II tests at room and low temperature conditions to simulate the expected ambient conditions in remote Northern Canadian communities.
- Adapt the flat panel manufacturing process and adhesive test results to enable the production of full-scale, high-quality micro-generating wind turbine blades.

1.3. Outline of Thesis

This thesis is structured as a series of Chapters that gradually build towards a reliable manufacturing process for full-scale wind turbine blade. Chapter 2 reviews the relevant literature related to vacuum infusion manufacturing of composite materials and the adhesive bonding of thermoplastic composites and relates these findings to industry standards in wind energy solutions. Chapter 3 comprises a comprehensive overview of flat panel VARTM processes and summarizes the iterative approach needed to optimize part quality. Chapter 4 focuses on the adhesive joining of thermoplastic composites by characterizing a methacrylate adhesive using Mode I double-cantilever beam (DCB) and Mode II end-notched flexural (ENF) tests. Chapter 5 synthesizes the findings in the preceding two chapters and details the complete manufacturing and assembly of a turbine blade. Chapter 6 will discuss the key findings of the thesis and highlight the limitations of the current work for production-ready parts. Finally, Chapter 7 concludes the thesis and provides recommendations for future work.

Chapter 2: Background and Literature Review

In this chapter, a general overview of composite materials is provided in Section 2.1, before focusing on the production of composite materials using VARTM processes in Section 2.2. Section 2.3 focuses on the mechanics and testing of adhesive bonding systems. Finally, Section 2.4 reviews the production of wind turbine blades.

2.1. Composite Materials

A composite material can be defined as a system with multiple constituent entities that are physically and chemically distinct, separated by an interface, and arranged in such a manner that the bulk properties of the composite material are distinct from the individual compounds [13]. Generally, a composite material is composed of a *matrix* phase and a *reinforcement* phase. A common composite material solution for structural applications includes high stiffness reinforcement fibers and a polymer matrix, yielding a *fiber reinforced plastic* (FRP) [11]–[13].

2.1.1. Matrix Systems

The matrix phase protects the fiber reinforcement from environmental and chemical degradation and allows loads to be transferred into the fibers via shear stresses at the fiber-matrix interfaces [21]. A wide variety of polymers are used in FRP parts to accommodate requirements related to production volume, costs, or part geometries. Polymers can be classified as either thermosetting or thermoplastic depending on their molecular structure [12]. Thermosetting polymers such as epoxies are commonly used in high-performance FRP composite structures. Compared to thermoplastics, thermosetting polymers have shorter molecular chains (i.e., lower degree of polymerization) with limited chain interactions, which allows the bulk compound to exist in a liquid form at ambient temperatures [22]. Because several thermosets are low-viscosity liquids at room temperature, they can be processed at room temperature without relying on high-pressure and high-temperature equipment [11]. Thermosetting polymers are then combined with a curing agent in-situ to initiate a chemical reaction that promotes irreversible cross linking between molecular chains where covalent bonds are formed. These cured thermoset polymers cannot return to a liquid form when heated, meaning they are unrecyclable [12].

Due to their characteristically longer molecular chains and extensive chain interactions, thermoplastic polymers remain solid at room temperature. Thermoplastics exhibit either

amorphous or semi-crystalline molecular structures with molecular chains bonded via secondary van der Waals forces [11]. Due to these secondary bonds between molecular chains, thermoplastics exhibit high molecular chain mobility when exposed to elevated temperatures, which enables melting and reshaping of the polymer (i.e., they are recyclable). Thermoplastics also exhibit higher ductility and fracture toughness when compared to unmodified thermosets by orders of magnitude [12], [13]. However, the mechanical benefits associated with thermoplastic polymers generally come at the expense of processability. Since thermoplastic polymers are solid at room temperature, the polymer must be heated above its melting temperature to allow the resin to wet out the fibers, which necessitates expensive tooling [12].

In-situ reactive thermoplastic resins – that polymerize low viscosity monomer or oligomer precursors during part production – have been developed to counter the processing difficulties associated with traditional thermoplastic polymers [18], [23]. Thus, reactive thermoplastic resins benefit from a low viscosity ($\approx 0.2\ Pa \cdot s$) enabling the adoption of traditional thermosetting FRP manufacturing processes while maintaining the mechanical and recyclability advantages associated with thermoplastic polymers [24]. Despite the added manufacturing flexibility, early reactive thermoplastic resins – such as caprolactam, laurolactam, or cyclic butylene terephthalate – require high processing temperatures to catalyze the polymerization reactions [18], [23], [24]. The Elium® 188 XO resin system (Arkema, France) is the only commercially available thermoplastic resin that polymerizes in-situ at room temperature [18], [23], [24]. This acrylic resin system is composed of 2-Propenoic acid, methyl methacrylate monomers (MMA), and acrylic copolymers that undergo free-radical polymerization into their polymethyl methacrylate (PMMA) form in the presence of a benzoyl peroxide initiator system [18]. The Elium® 188 XO system has been designed to minimize exothermic temperature increase to reduce the damage to the mold during processing [25]. The free radical vinyl polymerization reaction yielding PMMA is shown in Figure 2.1 [10].

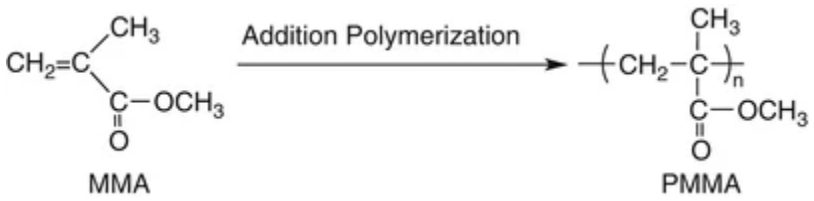


Figure 2.1: Addition polymerization reaction yielding PMMA from MMA monomer [10].

2.1.2. Fiber Reinforcement

The main objective during the design of continuous fiber-reinforced composites is to maximize the load transfer from the matrix system to the fiber reinforcement [11]. Typically, continuous fiber reinforcements in FRP structures are carbon, glass, or aramid, where glass fibers are the most widely used owing to their cost effectiveness [11]. The concentration of fibers or fiber volume fraction (V_f) is an important characteristic of composite materials that governs their mechanical properties [21]. The fiber volume fraction can be determined from samples of the composite material as per the following:

$$V_f = \frac{M_f}{M_i} \cdot 100 \cdot \frac{\rho_c}{\rho_f} \quad (1)$$

where M_f is the mass of the fibers, M_i is the initial mass of the sample, ρ_c is the density of the composite, and ρ_f is the density of the fibers.

Continuous fibers are arranged into *bundles* (called *rovings* or *tows*) during fabrication and multiple bundles are combined to form a fabric [11], [13]. Fiber bundles are often described as light- or heavy- depending on their linear density (TEX number). Reinforcement fabrics are required to manufacture FRP part using LCM processes and are fabricated into various forms. Unidirectional non-crimp fabrics (UD-NCFs) comprise tows that are all aligned along a single direction without any crimping of the fibers. Conversely, woven fabrics comprise intertwined longitudinal and transversely oriented tows, which create crimping in the fibers [26], [27]. To tailor the in-plane anisotropy of FRP composites, fabric layers can be stacked to create a *laminate*. A comparison between a UD-NCF and woven fabric is shown in Figure 2.2 [11].

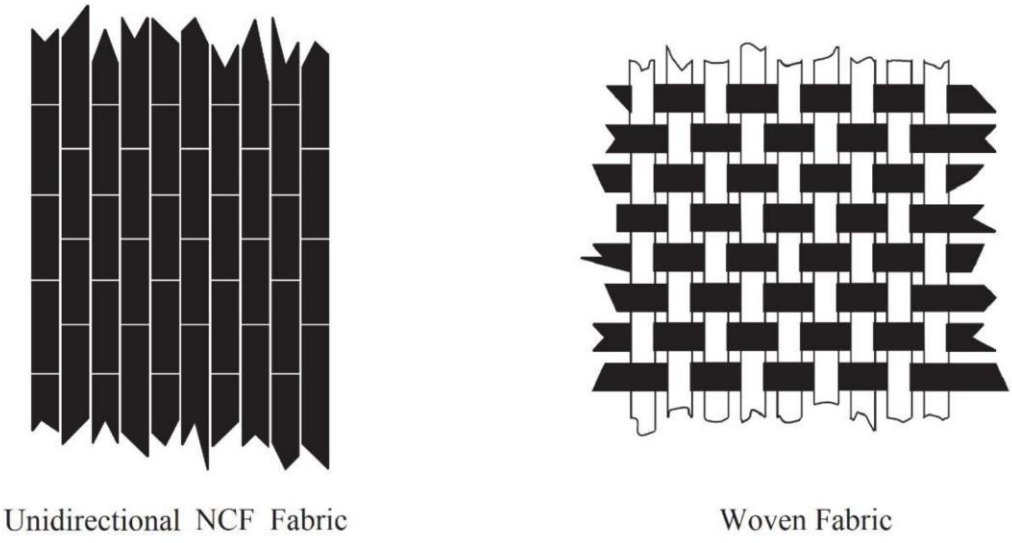


Figure 2.2: Comparison between unidirectional non-crimp fabric and woven fabric [11].

UD-NCFs rely on transverse supporting yarns to provide required integrity during handling, while polymeric stitching bonds the tows and supporting yarns [28], [29]. A polymeric veil is often stitched directly onto NCFs to aid with interlayer resin flow during manufacturing to reduce cycle times [30]. The veil temporarily reduces laminate compaction but melts away at elevated processing temperatures. A schematic of a UD-NCF fabric is shown in Figure 2.3 [31].

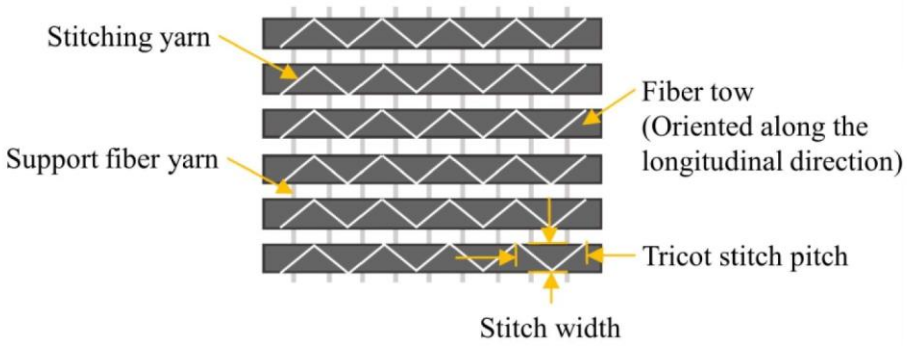


Figure 2.3: Schematic of unidirectional non-crimp fabric showing load-bearing longitudinal fiber tows and supporting stitching and transverse fiber yarns [31].

The fabric architecture influences FRP processing by affecting the drapability and resin permeability through the dry laminate. Generally, a lower ply areal weight is desirable as lighter fabrics have improved drapability [26]. Bilge et al. showed that lighter tows in glass fiber UD-NCFs improve the tensile strength of an FRP composite [32]. Schirmaier et al. showed that UD-

NCFs do not undergo shear-locking like woven fabrics since pure shear is not an intrinsic deformation mode during draping [28]. Thus, UD-NCFs can experience defects during draping including tow waviness and gapping that affect the localized mechanical properties [33]. Fabric architecture also affects nesting and compaction under pressure, which affects how tightly a laminate can be packed together and the resulting fiber volume fraction. As the interlayer compaction increases, localized resin pooling and tow waviness decrease [34], [35]. For NCF structures, Yousaf et al. found that increased inter-tow spacing and stitching thread thickness improves the fiber nesting, reducing the ply thickness per layer [36]. Similarly, Martin et al. observed that an increase in stitch density can improve the V_f from 50% to 55% by improving the dimensional stability of the fabric [29]. Rosso observed that the anisotropy of UD-NCF fabrics affects the resin flow front, and flow through the transverse fiber direction reduces the propensity of void formation compared to the faster flow along the longitudinal fiber direction [21].

2.2. Composites Manufacturing

According to Advani, composites manufacturing processes can be categorized by the associated resin transport mechanism [11]. Liquid composite molding (LCM) processes involve impregnating reinforcement fabrics with liquid resin and are typically reserved for thermoset polymers owing to their low viscosity. LCM encompasses a wide range of processes where a stack of dry fabric layers or a preform is placed in a mold and infused with resin after mold closure. Although reactive thermoplastic polymers solidify in a different mechanism from thermosets, their low viscosity during processing means that they can be processed using LCM processes.

Resin transfer molding (RTM) is an LCM process whereby a stack of preformed dry fabric layers is enclosed within a rigid two-part mold cavity before being infused with resin under pressure, which cures via chemical initiators at room or elevated temperatures. The resin is injected through a series of strategically placed inlet gates and allowed to fill the mold cavity. A more cost-effective variant of RTM replaces one of the rigid mold halves with a vacuum bag and pushes the resin through the fabric under vacuum at atmospheric pressure. This variant, interchangeably referred to as vacuum-assisted resin transfer molding (VARTM), vacuum infusion (VI), or resin infusion (RI), reduces the capital expenditure associated with RTM tooling and allows for even larger parts to be fabricated since the mold is not limited by the size of a press. Thus, large-scale

industrial wind turbine blades, boat hulls, and bridge sections are all fabricated using VARTM methods. Figure 2.4 shows an overview of the generalized VARTM process [11].

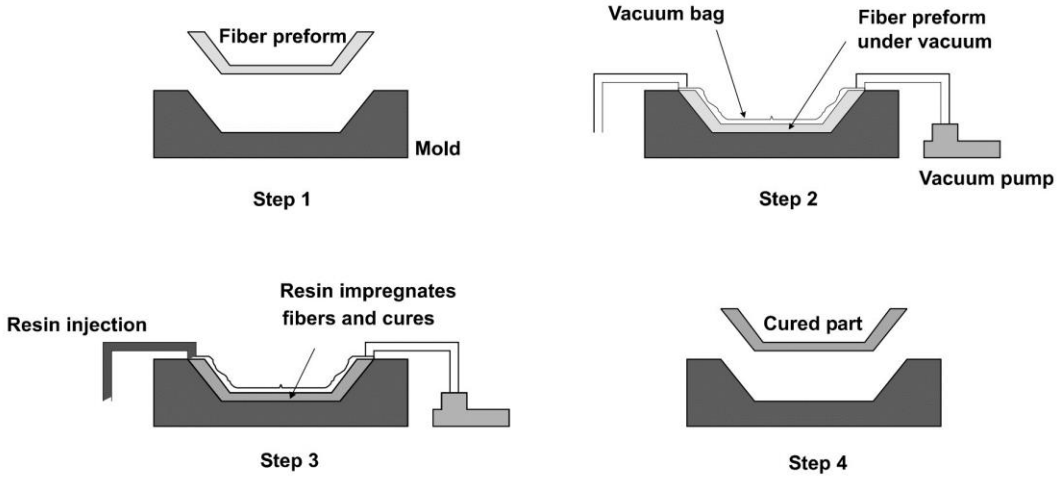


Figure 2.4: Generalized VARTM procedure [11].

VARTM simultaneously eliminates the requirements for high-pressure injection systems and two-part molds associated with RTM processes while still producing structural FRP parts [6]. However, VARTM processes suffer from poor surface finishes on the flexible vacuum bag side of the part and higher cycle times due to the low potential for automation. Furthermore, the low infusion and compaction pressures reduce the maximum allowable V_f, while the flexibility of the bagging film can induce thickness variability in the finished part between the inlet and outlet [37]. From a technical standpoint, the major issue with LCM processes is ensuring that the resin completely impregnates the dry fabric stack. Thus, low viscosity resins are preferred to ensure that the flow through the dry laminate stack is unobstructed, and resin systems are often designed with ample open time prior to gelation and solidification. Generally, VARTM process improvement is conducted via an experimental iterative approach, although simulation tools are increasingly being used to optimize the inlet and outlet locations for the mold [38].

The VARTM process, which is the focus of this thesis, provides a good compromise between cost effectiveness and part performance. The following sections introduce the physical models that explain VARTM (and most LCM processes in general) before focusing on various industrial innovations that aim to improve the standard VARTM process.

2.2.1. Darcy's Law

FRP manufacturing processes obey constitutive models that explain the interaction between the polymer and reinforcement as a function of temperature, pressure, cure kinetics, and other physical parameters [39], [40]. Fundamentally, VARTM is a problem of incompressible fluid flow through a porous medium. Thus, the velocity of the flow front can be explained by Darcy's law. The following representation of Darcy's law is adopted from Correia et al. and Polowick to describe 1D flow through a porous preform [39], [40]. The volumetric flow rate with Darcy's law can be expressed as:

$$Q = \frac{KA}{\mu}\frac{dP}{dx} \tag{2}$$

where Q is the volumetric flow rate through a cross-sectional area A, K is the permeability of the laminate stack, μ is the viscosity of the resin, and $\frac{dP}{dx}$ is the instantaneous spatial gradient of the fluid pressure. Equation (2) can be rearranged to assume the form:

$$u_x = -\frac{K}{\mu}\frac{dP}{dx} \tag{3}$$

where u_x is the superficial flow velocity, often referred to as the Darcy velocity. The basic formulation for Darcy's law in 1D holds in 3D space, but a variety of geometric assumptions can be applied to the fabric permeability [39]. Equation (3) can be expanded into matrix form to express the flow field in 3D as follows:

$$\begin{Bmatrix} \bar{u}_x \\ \bar{u}_y \\ \bar{u}_z \end{Bmatrix} = -\frac{1}{\mu}\begin{bmatrix} K_{xx} & K_{xy} & K_{xz} \\ K_{yx} & K_{yy} & K_{yz} \\ K_{zx} & K_{zy} & K_{zz} \end{bmatrix}\begin{Bmatrix} \partial P/\partial x \\ \partial P/\partial y \\ \partial P/\partial z \end{Bmatrix} \tag{4}$$

If the coordinate axes of the permeability tensor coincide with the principal material directions, the diagonal coefficients K_{xx}, K_{yy}, and K_{zz} are the only non-zero terms in the permeability tensor in Equation (4). For transversely isotropic cases (i.e, UD-NCF laminates), the principal directions

of the permeability tensor coincide with the longitudinal and transverse fiber orientations. Assuming a negligible laminate thickness compared to the planform area, the resin flow through the thickness can also be neglected [39]. Thus, the permeability tensor in 3D can be reduced to a 2D planar flow field as shown by Equation (5):

$$\begin{Bmatrix} \bar{u}_x \\ \bar{u}_y \end{Bmatrix} = -\frac{1}{\mu}\begin{bmatrix} K_{11} & 0 \\ 0 & K_{22} \end{bmatrix}\begin{Bmatrix} \partial P/\partial x \\ \partial P/\partial y \end{Bmatrix} \quad (5)$$

This formulation invokes the following boundary conditions for VARTM processes:

- Pressure at the inlet equals the atmospheric pressure, $P_{inlet} \approx P_{atm}$
- Pressure at the flow front equals the vacuum pressure, $P_{flow\ front} = P_{vacuum} \approx 0$

Thus, Equation (5) is a generalized version of Darcy's law that can be used to describe a resin flow through a flat, unidirectional dry fabric reinforcement during LCM processing [39]. In the following sections, the effect of permeability and compaction on the VARTM model will be discussed.

2.2.1.1. Through-Thickness Permeability

The negligible through-thickness permeability assumption in Equation (5) is possible due to the large dimensional discrepancy between the laminate thickness and the planform area. Nonetheless, there are multiple cases where the through-thickness permeability cannot be neglected, such as with 3D corner geometries [39]. The influence from the corner geometry on permeability is two-fold:

1. Flow around a corner increases the centripetal acceleration of the fluid. Centripetal acceleration can induce swirls in the fluid and subsequently cause pressure losses.
2. The fluid pressure will vary from the inner wall to the outer wall of a corner. The difference in radius between the inner wall and outer wall will cause a higher centripetal acceleration along the outer wall, inducing a pressure gradient on the fluid through the laminate thickness.

Additionally, VARTM variants have been developed that place a high permeability distribution mesh above the laminate stack to lower the resin flow time. The distribution mesh allows the resin

to cover the entire planform area quickly before penetrating through the thickness of the laminate instead of traversing the entire geometry of the part through the low permeability fabric reinforcement [11]. Thus, the resin flow front is non-uniform through the thickness, and the assumption regarding K_{zz} in Equation (5) cannot be applied since the upper surface of the laminate will be infused prior to the bottom surface.

2.2.1.2. Flat-Panel Compaction and Permeability Models

The flexibility of the vacuum bag used for VARTM processes adversely affects the uniformity of the laminate thickness and the compaction pressure during the infusion [39]. Since the total pressure within the laminate during VARTM is limited to the atmospheric pressure, the pressure can be expressed as:

$$P_{atm} = P_{comp} + P_{resin} \tag{6}$$

where P_{atm} is the atmospheric pressure, P_{comp} is the compaction pressure on the laminate stack, and P_{resin} is the fluid pressure within the resin. The fluid pressure gradient is non-uniform between the inlet vent and the flow front; thus, the compaction pressure on the laminate stack is also non-uniform and can be expressed as a function of the V_f according to the following relation:

$$V_f = V_{f0} {P_{comp}}^{B} \tag{7}$$

where, V_{f0} is the fiber volume fraction when the compaction pressure is 1 Pa, and the parameter B is experimentally determined [39]. Therefore, it can be shown that V_f is constantly changing with the compaction pressure on a laminate during resin impregnation.

Similarly, the permeability of the laminate can also be expressed as a function of V_f. Kozeny [40] assumed a capillary flow model to explain how the pressure loss in a fluid through a porous medium relates to the decrease in the permeability of the medium. Physically, the Kozeny model explains how the laminate permeability decreases as the intralaminar flow channels are gradually filled.

2.2.2. Conventional VARTM Processes

With VARTM conventional processes, a laminate stack is placed in a rigid mold and a sealed vacuum bag encloses the mold. Dry fabric is placed directly on the mold surface, yielding a smooth surface finish on the mold side of the panel [41]. Above the dry fabric, a peel ply layer is often used to aid demolding after part solidification. The peel ply conforms to the contours of the fabric, preventing a smooth surface finish from forming on the vacuum bag side [39]. If a smooth surface finish is required for a VARTM process, a rigid caul plate can be placed above the peel ply to mask the contours of the fabric tows [11]. To improve conformity of the bagging film, the bag is often over-sized compared to the planform area of the laminate, allowing pleats to be used. Pleats are excess wrinkles in the bagging film that can be manipulated to prevent the proliferation of vacuum bag bridging and wrinkle flow channels from forming on the laminate [42]. Strategically placed inlet gates and outlet vents allow resin to flow into the mold and traverse the dry reinforcement to completely impregnate the part [43]. The inlet line is connected to the resin source, while the outlet line is connected to a resin trap (or catch pot) that is itself connected to the vacuum. A schematic of a conventional VARTM process is shown in Figure 2.5 [44].

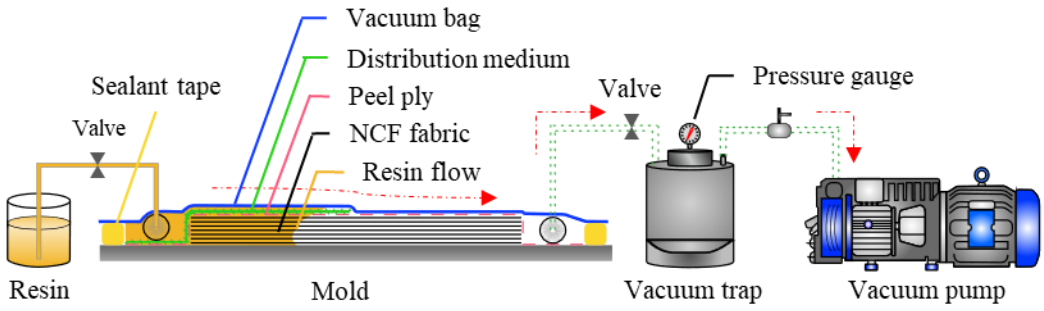


Figure 2.5: Schematic of conventional VARTM process with emphasis on the ordering of the laminate stack [44].

Composite parts may develop *voids* during processing due to entrapment of air in the resin or outgassing of volatiles, which can be characterized using the void volume fraction, V_c. A combination of high inlet pressure and low vent pressure with a low-viscosity resin has been shown to produce high-quality VARTM parts [45], [46]. Siginer observed that back pressure on the inlet side creates a larger pressure differential through the laminate, allowing the resin to transport entrapped voids towards the outlet vent without causing fiber misalignment [37]. However, excessive back pressure can also lead to uncontrollable V_f variations throughout the part [47]. Kuentzer et al. investigated the correlation of void distribution in a VARTM part with flow

resistance by continuously bleeding resin into the outlet vent after the part was fully infused [48]. Bleeding the outlet vent allowed the fabric to continue saturating in the resin and minimized void formation, while decreasing the diameter of the outlet vent – i.e, adding a resistance – slowed the bleeding rate and increased the resin pressure in the mold during saturation. Combining these two techniques can lower the void content throughout the laminate while increasing part uniformity [48]. Droste et al. [49] similarly observed that VARTM processing with a glass fiber UD-NCF fabric benefits from resin bleeding at the outlet, contributing to higher V_f with greater thickness homogeneity. However, it was also observed that bleeding the inlet line after full infusion can lower the V_f as excess resin is fed into the part. Dhimole et al. summarized how the various stages of the VARTM process can induce voids in the final part [50]. During pre-infusion, the moisture and gas in the resin must be minimized; thus, mixing in a degassing chamber is often recommended. During the infusion, the resin flow, pressure, and timing for multiple injection ports must be considered. During post-infusion, void formation is affected by the timing of the shut-off valve.

The VARTM process is also sensitive to ambient temperature during processing and curing. The viscosity of the resin can be reduced with increasing process temperatures, improving the penetration of the resin through the laminate stack. Elevated temperatures during curing can also improve the cross-linking of the matrix and simultaneously improve mechanical properties, at the expense of overhead costs. Modifications to the underlying VARTM process aim to simultaneously maximize V_f while minimizing V_c and the cycle time of the part. With these considerations for part quality summarized, the following sections will investigate common defects that may arise during VARTM processing.

2.2.2.1. Defects Resulting from Transverse Flow

Transverse flow occurs when the permeability through the laminate stack is non-uniform, causing a discrepancy in the flow velocity between the surfaces of the laminate [11]. Certain variants of the VARTM process may include a high-permeability distribution medium that allows resin to quickly cover the planform area of the laminate before gradually seeping through the surface. In these cases, the discrepancy in the through-thickness resin velocity can entrap voids along the laminate surfaces. These voids become surrounded by resin without a means to be transferred through the mold, causing defects in the solidified part (Figure 2.6).

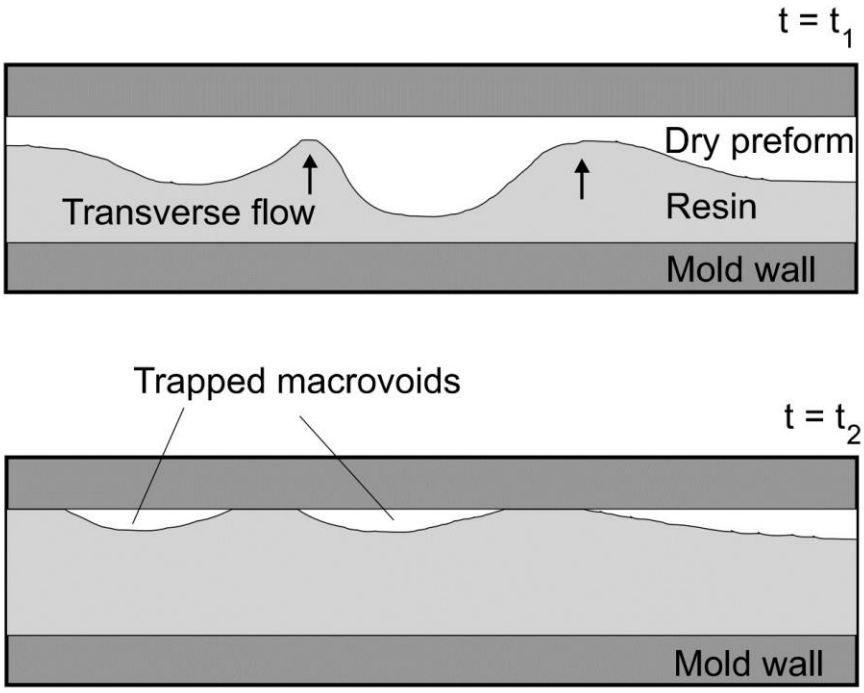


Figure 2.6: Schematic of void entrapment during VARTM processing. Large discrepancies in through-thickness flow velocity increases the likelihood of void entrapment [11].

2.2.2.2. Dual-Scale Flow-Induced Defects

Dual-scale flow occurs when the permeability of the fabric is non-uniform throughout the microstructure [11]. Generally, the inter-layer (macro) resin flow experiences a higher velocity than the intra-layer (micro) resin flow because of the increased permeability between the fabric layers. If the discrepancy between these dual-scale flows is sufficiently large, the macro flow can penetrate the fiber tows downstream of the micro flow and form micro-voids within the tow (Figure 2.7). The discrepancy between inter- and intra-bundle flow becomes even greater as the laminate compaction decreases and the inter-tow flow channels become larger, causing increasingly severe void formation. Alternatively, if the pressure gradient between the inlet and outlet is sufficiently small, the resin will experience a faster flow within the tows due to capillary action, creating inter-bundle voids and simultaneously increasing the infusion time.

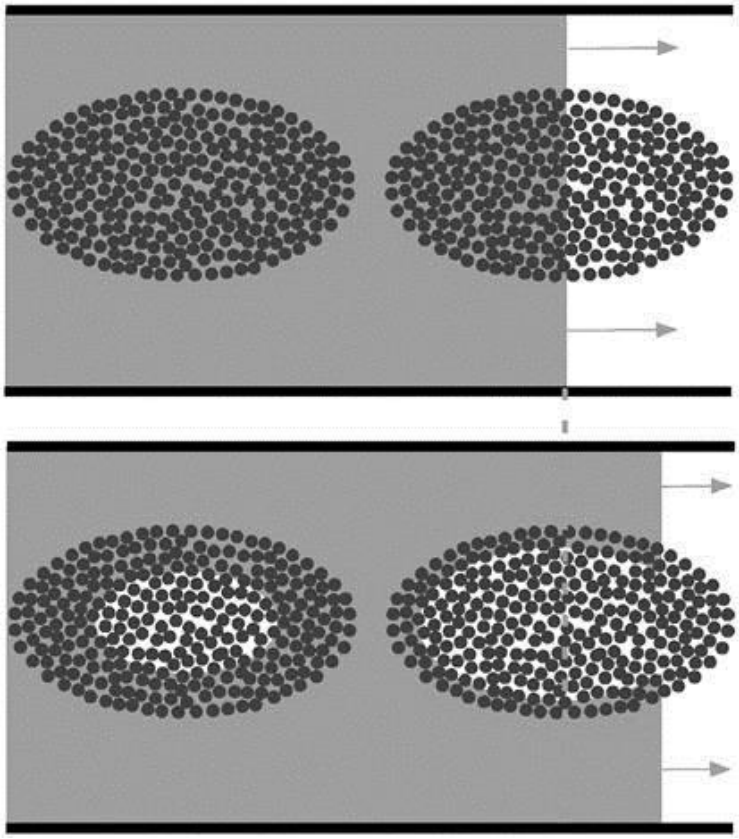


Figure 2.7: A comparison between an idealized uniform flow front during LCM processing compared to a more accurate model that considers delayed saturation due to localized variations in fabric permeability. This dual-scale flow phenomenon can entrap voids in parts [11].

2.2.2.3. Race-tracking and Resin Starvation

Race-tracking occurs when gaps between the laminate, mold, and vacuum bag create a high-permeability flow channel that accelerates the localized resin flow front in a non-uniform manner [11]. In an idealized framework, perfect drapeability and mold filling would unify the porosity and permeability of a dry fabric, and this assumption can generally be applied to resin flow through a laminate stack placed on a flat panel. However, in complex mold geometries, the drapeability of a laminate around sharp corners is non-uniform. In these situations, preferential flow channels can form under vacuum and create non-uniform flow fronts during processing. Race-tracking can also occur along mold walls, laminate edges, or along bag wrinkles where small void pockets cannot be eliminated. A schematic of a corner geometry in a part that can become susceptible to race-tracking is shown in Figure 2.8 [11].

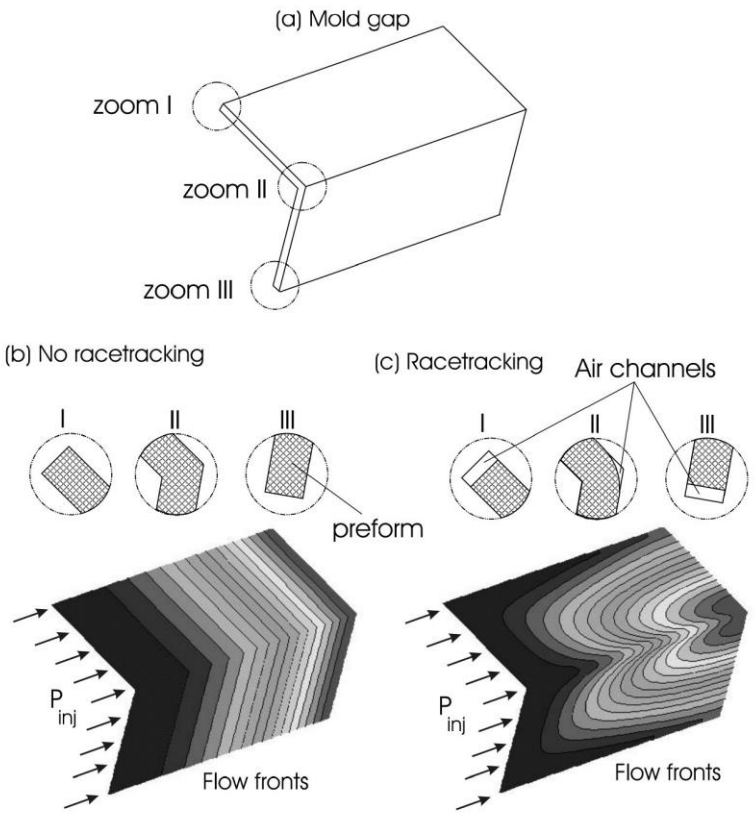


Figure 2.8: Comparison between idealized flow through a preform with uniform flow front and realistic flow that considers higher permeability air channels, contributing to a race-tracking effect [11].

Race-tracking can cause resin starvation in a part by encircling a dry pocket and not allowing inlet pressure or an outlet vacuum to transfer the voids out of the mold [11]. This pocket can become dominated by resin, contributing to resin pooling defects. Resin starvation can also occur due to a poor inlet gate and outlet vent layout strategy where multiple flow fronts can reattach downstream of a dry spot, permanently entrapping voids. If the layout of the laminate consistently causes resin starvation, the mold must be redesigned. Figure 2.9 shows resin starvation due to a multi-gate setup where the resin from one inlet reaches the outlet vent before the second half of the mold can be fully impregnated [11].

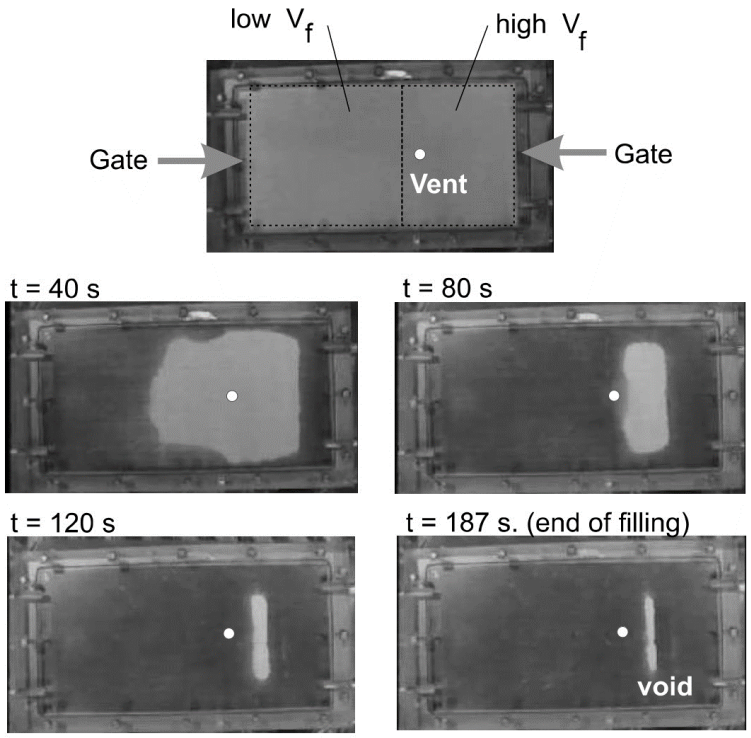


Figure 2.9: Resin starvation during VARTM processing due to race-tracking effects and poor gate/vent selection [11].

2.2.2.4. Non-uniform compaction

To attain a high-quality part with minimal thickness variation, a consistent laminate compaction must be maintained throughout a part [51]. Laminate compaction increases the V_f of a part by compressing the dry fabric together; however, non-uniform compaction can influence defect formation. Insufficient compaction may occur due to vacuum bag bridging around a concave corner, allowing the part to become susceptible to dual-scale flow phenomena. Alternatively, excessive laminate compaction around a convex corner may contribute to resin starvation if the atmospheric pressure is not sufficiently high to transport the resin through the constriction. For VARTM processes, laminate compaction uniformity can be aided with pleats in the vacuum bag that prevent the bag from bridging. Bloom et al. provided a comprehensive study on the effect of pleats on the laminate pressure distribution [42]. The effect of sharp corners, bag wrinkles, and bag bridging on the fluid pressure was demonstrated as the resin impregnated the fibers. Insufficient bagging material around a convex corner increased the localized fluid pressure as the bag was stretched and pulled around the edge of the corner, while concave corners with insufficient bagging material experienced bridging and poor fluid pressure, reducing the quality of

the infusion. Bloom et al. observed that low-pressure regions in the bag contributed to void formation and a loss of dimensional accuracy in the cured part [42].

2.2.3. VARTM Process Variants

The following sections highlight modified VARTM solutions reported in the literature. Many of the ensuing sections reference data from Bodaghi et al. and van Oosterom et al., who provided comparison studies between modified VARTM processes and high injection pressure RTM (HIPRTM) and traditional VARTM, respectively [47], [52]. Figure 2.10 below from van Oosterom et al. shows a detailed schematic of the VARTM variants [52].

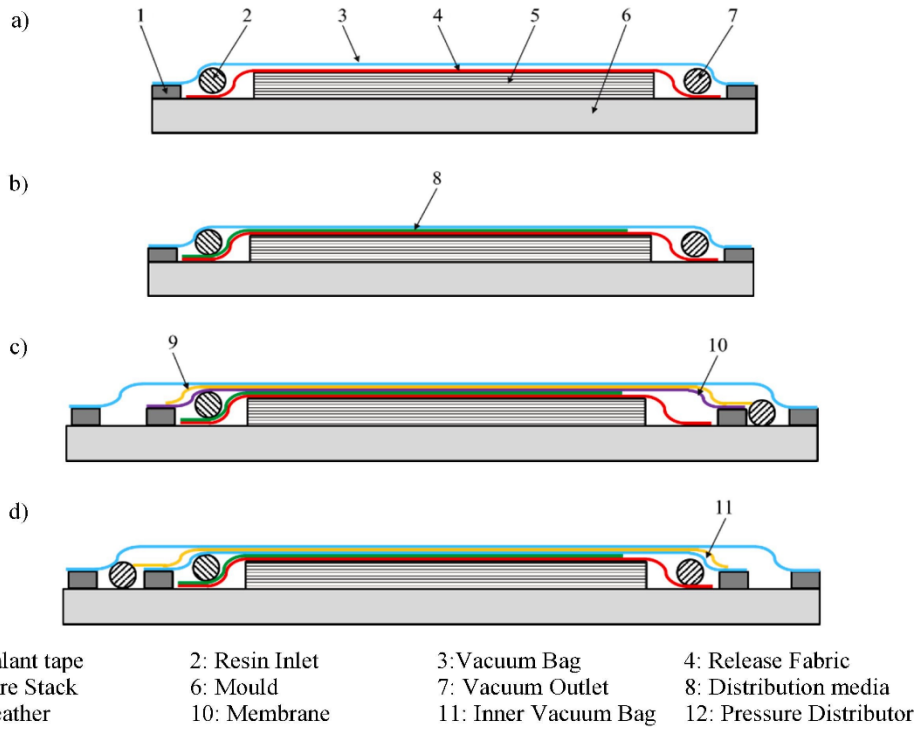


Figure 2.10: Comparison of VARTM variants from van Oosterom et al. [52]*; (a) VARTM, (b) Seeman's Composites Resin Infusion Molding Process (SCRIMP) and controlled atmospheric pressure resin infusion (CAPRI), (c) vacuum-assisted process (VAP), and (d) double bag vacuum infusion (DBVI).*

2.2.3.1. SCRIMP

The Seeman's Composites Resin Infusion Molding Process (SCRIMP) is the most widely adopted variant of the VARTM process in industry [52]. The SCRIMP system incorporates a series of porous spiral infusion lines to quickly direct resin towards various locations in the mold before allowing the resin to flow through a high-permeability distribution mesh and impregnate the entire part. Because of an increase in permeability of the distribution mesh by 2-3× when compared to

the laminate stack, the SCRIMP method allows for significantly reduced processing times compared to the standard VARTM method, particularly if multiple injection ports and infusion lines are used [11]. The high-permeability distribution mesh also enables the production of larger parts as the increased flow velocity reduces the risk of premature gelation. A disadvantage associated with the SCRIMP process is the increased propensity for void content due to the transverse flow phenomenon described in Section 2.2.2.1.

Van Oosterom et al. showed that the SCRIMP process can reduce the infusion time by 20% compared to conventional VARTM methods [52]. Additionally, the increased permeability of the distribution mesh reduces the pressure and thickness gradients from the inlet to the outlet; the variation in laminate thickness from the inlet to the outlet with SCRIMP was 0.3%, compared to 5% for VARTM. However, the SCRIMP process may become susceptible to increased V_c due to the transverse flow phenomenon if the fluid flow velocity is excessive. Thus, strategic placement of the distribution mesh and choking of the inlet vent may be required during process optimization. An optimized SCRIMP process can produce parts with a void content as low as 0.2% [52]. While V_f is not noticeably improved with SCRIMP processes compared to VARTM, short beam strength and combined loading compression strength tests for SCRIMP samples did not show a statistically significant difference compared to other VARTM variants that specifically target increased V_f values [47].

2.2.3.2. Double vacuum bag infusion (DBVI)

Double vacuum bag infusion (DBVI) utilizes two separate vacuum bags placed on top of one another. The two vacuum bags are separated by a breather cloth that is used to allow air or volatiles to escape the mold and prevent defects [47], [52]. The influence of DBVI processes on V_c has shown conflicting results in the literature [52], and Bodaghi et al. observed that DBVI may not lead to a reduction in V_c during resin infusion [47]. While the inclusion of a breather cloth attempts to aid the extraction of volatiles, the second vacuum bag can hinder the through-thickness permeability and air transport. Similar discrepancies in the literature have been observed with V_f; Bodaghi et al. observed that a second vacuum bag can increase the fiber nesting during compaction depending on the fabric structure, while van Oosterom et al. observed that DBVI may reduce V_f compared to VARTM and SCRIMP methods, and that the second vacuum bag does not noticeably aid laminate compaction [47], [52]. Additionally, van Oosterom et al. observed that the thickness

variation in the part caused by the DBVI process can increase compared to other VARTM variants due to a non-uniform pressure distribution caused by the breather cloth [52]. Summarily, literature review yields contradictory opinions about the validity of the DBVI process.

2.2.3.3. Vacuum assisted process (VAP)

The vacuum assisted process (VAP) was initially developed by AIRBUS and utilizes a gas permeable membrane to entrap the infused resin in the mold without bleeding the resin into the outlet vent [47]. Like the DBVI method, VAP is designed to provide uniform compaction on a preform to minimize the thickness variation while continuously degassing the resin to remove voids and other volatiles [47]. The VAP process has been adopted for large aerospace structures including the AIRBUS A400M cargo door. Krehl et al. observed that the VAP process can lead to an 80% reduction in V_c and 77% reduction in thickness variation compared to conventional VARTM for a 15-ply woven E-glass FRP laminate [53]. However, VAP can also reduce the through-thickness laminate permeability and increase the filling time.

Bodaghi et al. showed that the VAP process can lead to an increased part thickness due to the continuous introduction of resin at the inlet and restricted flow at the outlet caused by the gas permeable membrane [47]. Thus, to increase the V_f of the part, the required resin content must be calculated in advance or detected via sensor to choke the inlet flow at the right moment. While the operating principle of VAP and DBVI is similar (i.e, using a gas permeable interface to control resin flow without transferring resin into the outlet vent), VAP has consistently provided low V_c figures in the literature, unlike DBVI.

2.2.3.4. Controlled atmospheric pressure resin infusion (CAPRI)

Controlled atmospheric pressure resin infusion (CAPRI) is a variant of the VARTM process initially developed for aerospace applications by Boeing. With CAPRI, the dry laminate is cyclically bulked and debulked under vacuum to increase fiber nesting and compaction prior to infusion. Droste et al. demonstrated that cyclic compaction on a glass fiber UD-NCF can decrease the laminate thickness for VARTM parts [49]. In addition to cyclic debulking, the CAPRI process uses two vacuum pumps placed at the inlet and the outlet to reduce the overall pressure gradient. One pump produces a full vacuum on the outlet while the second pump creates a partial vacuum on the inlet side, allowing the CAPRI process to theoretically produce autoclave quality parts at the expense of increased cycle time [47], [52]. Niggemann et al. completed the most detailed

assessment of the CAPRI process and found that 400 debulking cycles – each for 10 seconds – can increase the quality of the final part compared to other VARTM variants at the expense of an increased cycle time. While the setup is identical to the SCRIMP method, the cyclic debulking and partial vacuum at the inlet has been shown to increase V_f by 5% compared to SCRIMP while reducing V_c below 1% [54].

Bodaghi et al. showed that CAPRI can provide a good balance between increased V_f, reduced V_c, and minimized thickness variation [47]. In the study by van Oosterom et al. with veil-less UD-NCF glass fibers, the CAPRI process consistently delivered the highest V_f of all VARTM variants [52]. Additionally, because the gas permeability of the laminate is not inhibited, CAPRI processes decrease V_c by enabling off-gassing of volatiles. The competitive physical properties of the CAPRI samples recorded by van Oosterom et al. came at the expense of a 60% increase in infusion time due to increased laminate compaction [52].

2.2.3.5. VARTM with Dynamic Pressure Control (DPC)

Since VARTM parts are sensitive to inlet back-pressure, compaction pressure, and vacuum level, there has been ongoing research into dynamic pressure control (DPC) for VARTM. DPC allows increased control over the vacuum bag relaxation properties to enable a shorter infusion cycle time while subsequently increasing bag compaction during the curing phase. Instead of relying on atmospheric pressure for bag compaction, the mold is placed in a two-way pressurized chamber during DPC [51]. Infusing the resin in a vacuum chamber allows the flow rate to be optimized for minimum cycle time and V_c simultaneously. With a variable vacuum chamber pressure, operators can avoid accelerating the resin too quickly through the mold and create voids in the final part. Once the resin has completely impregnated the dry fabric, positive pressure can be applied in the chamber to compress the vacuum bag onto the laminate and aid compaction. Figure 2.11 from Yalcinkaya et al. shows a schematic of VARTM with DPC [51].

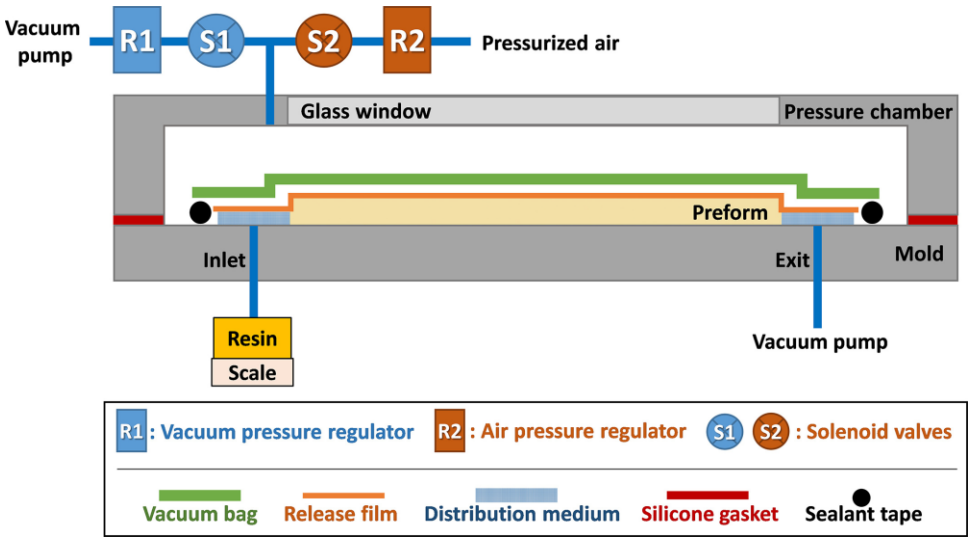


Figure 2.11: Schematic of VARTM process with dynamic pressure control (DPC) in a two-way adjustable vacuum chamber [51].

Yalcinkaya et al. compared DPC to an infusion trial with static pressure (where the vacuum pressure was not adjusted during the pre-infusion, infusion, and post-infusion stages) and found that DPC reduced the infusion time by 48% due to the increased flow rate allowed by the vacuum environment. Compared to conventional VARTM processes that yielded a thickness variation of 15%, DPC panels were produced with a thickness variation of approximately 1%. The V_f and V_c were 64% and <1%, respectively, for a glass fiber composite panel. Further research into DPC studied the integration of fluid pressure sensors and heating elements in the mold to change the viscosity of the resin in real-time for even greater process control [51]. While the pressure chamber may impose restrictions on part size and would increase the cost of production, DPC allows VARTM processes to produce near-RTM quality parts.

2.2.3.6. Light-RTM

Light-RTM is a variant of LCM that borrows elements from RTM and VARTM by combining two-part reusable molds with a resin infusion under atmospheric pressure. Light-RTM combines a rigid bottom mold with a semi-flexible upper mold that is supported by a rigid periphery. The rigid periphery from the upper mold creates a vacuum seal with the bottom mold [55]. Because the upper and lower molds are vacuum sealed – instead of forced together via press – the infusion pressure is limited to the atmospheric pressure. Hutchinson et al. compared a Light-RTM process with VARTM and found that the VARTM process could produce parts with a 3% higher V_f due to the increased compliance of the bagging film [56]. Conversely, the semi-rigid

upper tool used in Light-RTM imposed a minimum cavity height on the part. Since the infusion pressure is limited to the atmospheric pressure, the cavity height cannot be set as aggressively as RTM processes, limiting the V_f. Nonetheless, Light-RTM parts demonstrate improved thickness uniformity, smooth surface finishes on both sides of the part, and a consistently lower V_c compared to parts produced with a disposable vacuum bag. Hutchinson et al. compared the mechanical properties of the VARTM and Light-RTM parts and observed that the disparities were minimal but favorable towards the Light-RTM parts [56].

2.2.3.7. Reusable Silicone Vacuum Bagging

A cheaper variant of the Light-RTM process incorporates a reusable silicone vacuum bag. The silicone vacuum bag fabrication process involves spraying silicone on a laminate stack placed in the rigid mold and using wax strips and infusion mesh to create the resin flow channels. The cured bag is then able to conform to the mold without complex bagging techniques [57]. The benefits of the reusable silicone bagging technology are threefold: a significant reduction in cycle times compared to disposable vacuum bags, a very fast pay-off in capital investment (estimates as low as 10 molding cycles), and a longer-term reduction in labour costs due to the simplicity of the setup [57]. However, the surface finish is generally not improved with a reusable silicone bag, and bag production requires additional optimization of the flow channel setup [39]. Sunilpete et al. observed that silicone vacuum bags offered marginal improvements in mechanical properties and V_f compared to baseline VARTM processes [58]. The main advantage with silicone vacuum bags is the cost savings associated with their reusability, particularly at large production volumes.

2.2.3.8. VARTM Laminates with Magnetic Consolidation

Magnetic consolidation for VARTM processes places a series of magnets on the laminate stack (outside of the mold) to aid fabric compaction during curing. Magnetic compaction effectively incorporates an out-of-mold caul plate that sits on the bag side and simultaneously increases pressure on the laminate [59]. Thus, magnetic consolidation employs a conventional VARTM setup that benefits from an above-atmospheric pressure distribution at the expense of increased tooling costs. To test the magnetic consolidation concept, Amirkhosravi et al. manufactured 6, 12, and 18 ply laminates that were each split into trials without magnetic compaction, with magnetic compaction applied before the infusion, and with magnetic compaction applied after the infusion [59]. Magnetic compaction reduced the average thickness of the parts by

20% while increasing the V_f by 6% compared to trials without any magnets added to the laminate stack. At a compaction pressure of 0.2 MPa or higher, the V_c of the panels was reduced to below 0.5% for the trials where magnetic compaction was applied before the infusion (the void content of the samples was not improved by applying magnetic compaction after the infusion). However, the cycle time for samples with magnetic compaction applied prior to the infusion increased from 3 minutes to 18 minutes [59], [60]. Magnetic compaction during VARTM processing improved the flexural strength and the surface quality of the panels compared to the uncompacted trials [59].

2.3. Adhesive Joining

Adhesives represent an alternative to mechanical fasteners or thermal welding for material joining. Unlike mechanical fasteners, adhesive systems ensure that stresses are uniformly transferred between joined parts. Generally, adhesives are applied as a paste onto the target surfaces (substrates) and allowed to chemically react or physically cure, which creates a solid layer [61]. The relative surface energies between the constituents governs the interactions between the adhesive and the substrates. Substrates with high surface energies completely absorb liquids with low surface tension [62]. Conversely, low-surface energy substrates – deemed hydrophobes – do not readily accept a liquid at the interface and are more difficult to bond [61].

Prior to adhesive bonding, various surface treatments can be performed on a substrate to increase the surface energy and remove contaminants that may affect the bond strength [62]. A simple solvent degreasing procedure – where alcohol is wiped on the surface to remove contaminants – can increase the surface energy of a substrate by removing the weak boundary layer formed by environmental volatiles. Alternatively, the surface roughness can be increased by abrading the substrate to increase mechanical interlocking with an adhesive system. For FRP composite processing, the presence of a peel ply leads to roughening of the solidified surface such that further mechanical treatments are unnecessary for subsequent adhesive bonding [63]. In high-performance applications, more intensive procedures such as chemical acid etching or plasma treatment may be required to further increase the substrate surface energy.

2.3.1. Adhesive Systems

Adhesives can be optimized for a variety of functional requirements. Klingen characterizes adhesives by their overlap shear strength using the following criteria [61]:

- *Structural bonding in aerospace applications*: 30-40 MPa
- *Structural bonding in industry and trade*: 15-25 MPa
- *Elastic bonding with Polyurethanes and Silicones*: <5 MPa
- *Elastic bonding with acrylic foam tapes*: <1 MPa

Due to their inherently strong bond, and chemical and temperature resistance, epoxy adhesives are widely used in industry [61]. However, studies have shown that epoxy adhesives may not be capable of structurally bonding thermoplastic composite materials due to their low rate of diffusivity [64]. The primary mechanism of adhesion when the adherend and the adhesive are both polymers is through diffusion, which occurs when adhesive molecules penetrate the substrate and form a new layer that is not identical to either bulk composition. The low diffusivity rate of an epoxy pre-polymer into a thermoplastic polymer – caused by the chemical inertness of the thermoplastic substrate due to the length of the polymer chains – limits the total intermolecular diffusion, resulting in an insufficient formation of epoxide groups that could react with the thermoplastic substrate [64].

Davies et al. showed that the joint strength of an FRP thermoplastic composite bonded with a conventional epoxy adhesive depends greatly on the surface treatment [65]. An alcohol degreasing procedure was shown to yield a lap shear strength of 5 MPa, whereas a more intensive acid or oxygen plasma etching technique increased the lap shear strength to 30 MPa for the same material combination. Thus, the surface treatment elevated the adhesive joint from an elastic bond to a structural bond as defined by Klingen. Thermoplastic surfaces do not become very chemically reactive after abrasion since mechanical treatments are not as effective at breaking the intermolecular bonds of the polymer chains on the surface, necessitating investment in more costly surface treatments [66].

An alternative to conventional epoxy adhesive systems for structural bonding of thermoplastic materials are methyl methacrylate (MMA) adhesives. Due to their higher rate of diffusivity, MMA adhesives can easily etch the surface of plastic materials [67]. Therefore, MMA adhesives are highly compatible with oily and greasy surfaces and provide high-strength and fast processing due to their rapid polymerization rates [68], [69]. MMA adhesives have additional benefits including the ability to cure at room temperature while retaining non-slump properties during processing. Combined with an ability to achieve a “green strength” quickly, this allows

parts to be moved and stored as the adhesive cures without sliding and affecting the final alignment [68]. MMA adhesives cure via free-radical polymerization of methyl methacrylate and various additives – such as polymerizable isocyanate compounds – can be added to improve adhesion with lower-energy plastic surfaces. MMA adhesives are commonly used in the wind energy industry due to their limited surface pre-treatment requirements [19], [68], [70], [71].

In cases where PMMA is bonded to itself, the substrates can be solvent cemented by allowing an acid (generally glacial acetic acid) or chlorinated solvent (such as methylene dichloride) to soften and swell the surfaces and allow the materials to fuse together as the solvent diffuses and evaporates [72]. The principle of solvent cementing eliminates the need for complex surface treatments; PMMA adhesives undergoing solid cementing generally require an abrasion treatment with 180-400 grit sandpaper and isopropanol degreasing to clean the surface of contaminants [62]. MMA adhesives undergo a variant of solvent cementing where the methacrylate monomer (instead of a solvent) is responsible for dissolving the PMMA substrate before polymerizing in the joint, allowing for high-strength structural bonding of large surface areas.

2.3.2. Adhesive Joint Failure Modes

Alongside the adhesive and substrate material systems, the strength of an adhesive joint is dependent on the geometry, which can affect the stress distribution throughout the adhesive layer [63]. For instance, the strength of the adhesive joint increases with the overlap length and is also sensitive to the bond-line thickness [73]. Generally, adhesives can be exposed to 5 different stress conditions [74], namely tensile, shear, cleavage, peel, and compressive stresses (Figure 2.12).

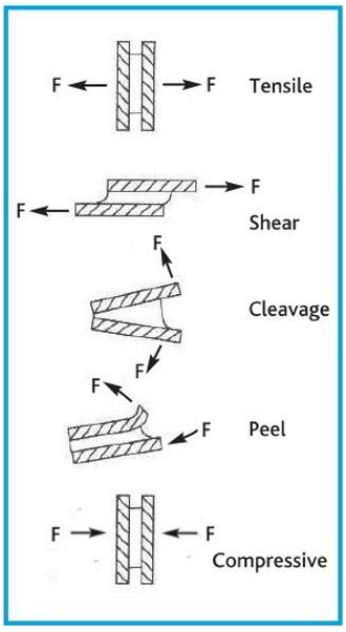


Figure 2.12: Summary of stress state conditions for adhesive joints adapted from Petrie [74].

Pure tensile stresses occur when both substrates are being pulled apart perpendicular to the plane of the joint, ensuring that the load is distributed evenly across the entire bonding surface. Adhesives show good resistance to purely tensile loading condition, but these situations are not common in practical applications since adhesive joints are generally exposed to mixed-mode loading. Thus, load cases where the substrates are being pulled apart often induces simultaneous bending moments resulting in cleavage or peel stresses. Peel and cleavage stresses are undesirable since the load is concentrated on a portion of the bond instead of the entire surface [74]. Therefore, shear loading scenarios are desirable in practical adhesive joint designs. Unlike peel and cleavage stresses, joints undergoing shear loadings ensure that the load is distributed evenly across the entire bond surface.

Banea et al. report six common failure modes for adhesive bonded composite joints [75], namely cohesive, thin-layer cohesive, adhesive (interfacial), fiber-tear, light-fibre-tear, and stock-break (Figure 2.13). In general, cohesive failure modes – where the failure occurs entirely within the adhesive layer – indicate that the strength of the adhesive was maximized, and that the interfacial strength between the adhesive and the substrate was not the limiting factor during failure. Additionally, failure within the adhesive layer causes uniform and predictable crack

propagation, and cohesive failure modes are generally desirable. Conversely, adhesive failure is observed if the failure occurs at the adhesive/substrate interface and indicates that the strength of the adhesive was not maximized. For a composite joint, fiber-tear is a common observation if a high-strength adhesive is used. In these cases, the relatively low thickness of the composite skins leads to through-thickness stresses and failure within the substrate, and the fracture surface will show exposed fibers. A stock-break failure occurs when the applied load exceeds the strength of the substrate entirely.

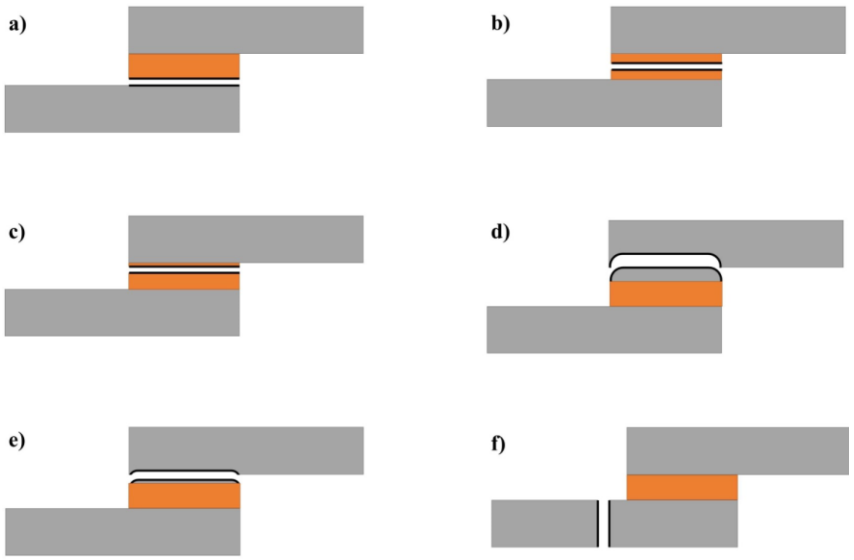


Figure 2.13: Adhesive joint failure modes from Dehaghani [63]*; (a) adhesive (interfacial) failure, (b) cohesive failure, (c) thin-layer cohesive failure, (d) fiber-tear failure, (e) light fiber-tear failure, and (f) stock-break failure.*

2.3.2.1. Adhesive Joint Testing

Fracture mechanics principles are commonly applied to adhesive joint characterization. Adhesives can be characterized by three failure modes where Mode I is an opening failure caused by normal loading, Mode II is sliding failure caused by in-plane shear loading, and Mode III is tearing failure caused by out-of-plane shear loading (Figure 2.14) [76]. Various standardized experimental setups have been developed to characterize the fracture toughness of an adhesive in mixed and/or pure Mode I, II, and III loading conditions.

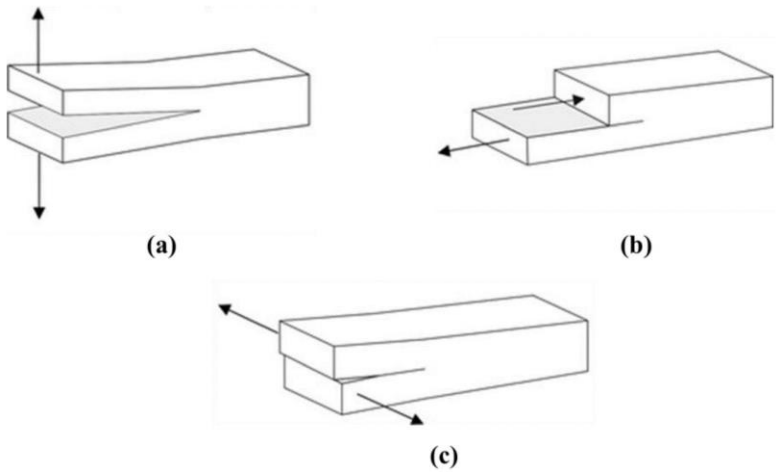


Figure 2.14: Fracture mechanics failure modes [76]*; (a) Mode I (opening), (b) Mode II (sliding), and (c) Mode III (tearing).*

Standardized experiments in fracture mechanics for adhesive joints aim to extract either the stress intensity factor or the strain energy release rate (SERR), which are both measures of fracture toughness. The latter approach states that a pre-existing crack will propagate when the required internal energy of the system is released, i.e., the SERR reaches a critical value (G_C; critical SERR) [77]. The fracture toughness of the adhesive depends on the failure mode; the Mode I critical SERR (G_{IC}) is generally not equal to the Mode II (G_{IIC}) or Mode III (G_{IIIC}) critical SERR values. To assess Mode-I and Mode-II fracture toughness, the two most common tests are the double cantilever beam (DCB) and end-notched flexural (ENF) methods, respectively [78], [79]. DCB and ENF tests require bonding of two substrates with equal length and width using a constant thickness adhesive layer. Due to the existence of a pre-crack, the energy imparted on the specimens is concentrated to enable crack propagation within the adhesive layer.

Both the DCB and ENF test methods incorporate a variety of data reduction schemes within the associated ASTM Standards to determine the critical SERR values. The G_{IC} parameter from DCB testing can be determined via image capture of the crack propagation using the modified beam theory (MBT), or by considering the effective stiffness of the substrates and solving analytically (i.e, compliance calibration or CC) [63], [80]. However, the ENF test setup is not very receptive to video capture of the crack propagation since the crack tip during sliding is difficult to observe. Thus, new data reduction methods are being investigated that use digital image correlation (DIC) techniques to more accurately assess the location of the crack tip during in-plane shear

deformation [81]. Schematics of the DCB and ENF specimens for Mode I and Mode II testing are provided by Ribeiro et al. and shown in Figure 2.15 [82].

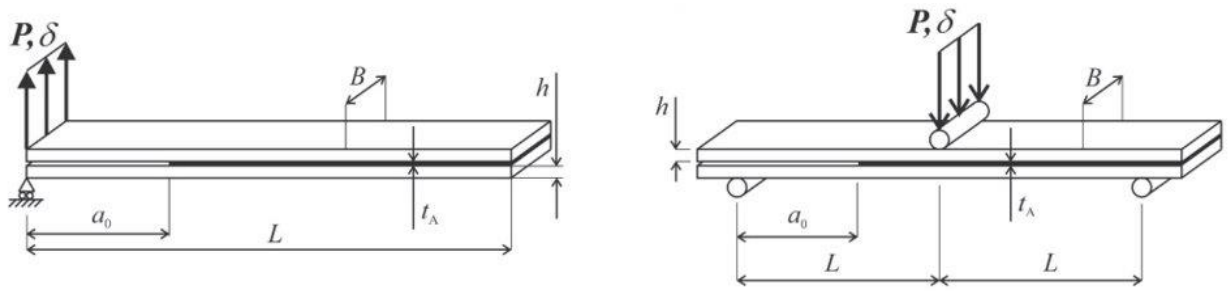


Figure 2.15: DCB and ENF specimen schematics [82].

For DCB tests, the calculated G_{IC} value can be used to numerically model the adhesive joint using a cohesive zone model and the associated traction separation law (TSL). The TSL captures the stress and displacement of the adhesive within the fracture process zone ahead of the crack tip. A bilinear TSL is the most widely used where the deformation of the adhesive can be expressed via the elastic stiffness, the peak traction, and the fracture energy (or displacement) [63]. For DCB tests, G_{IC} captures the energy required for separation, and an inverse parameter fitting can be performed to calibrate the remainder of the TSL with experimental data. A schematic of the bilinear TSL is shown in Figure 2.16 [63].

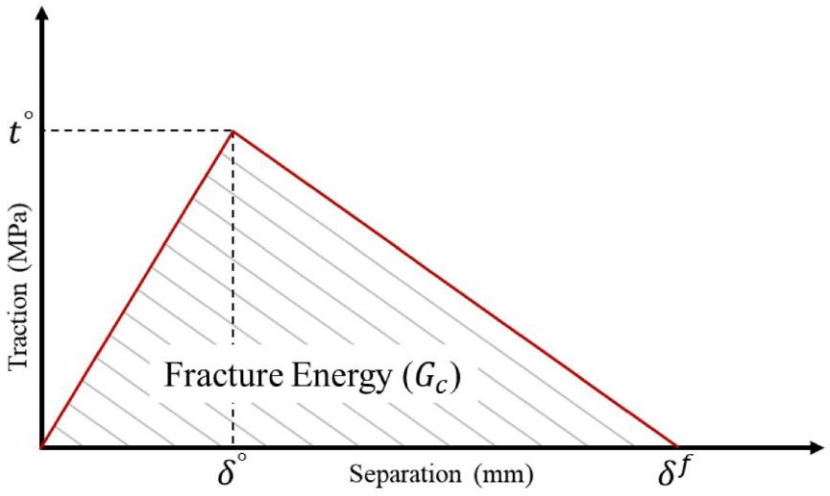


Figure 2.16: Bilinear traction-separation law that can be used in a cohesive zone model (CZM) [63].

2.3.3. Effect of Bond-line Thickness on Adhesive Performance

The effect of bond-line thickness on adhesive performance is not fully understood, and contradictory results are reported in the literature. Classical elastic theory predicts that an increase in the bond-line thickness should translate to an increase in the joint strength, but many experimental studies do not support this analysis [83]. This discrepancy in performance has been variously attributed to the size effect (since thicker bond-lines have increased likelihood for voids and microcracks) and increased interface stresses caused by rapid spreading of the adhesive at larger bond-line thicknesses [73], [84]. Castagnetti et al. observed that an MMA adhesive undergoing cohesive failure experiences an increasing static strength as the adhesive thickness decreases from $0.4mm$ (6 MPa) to $0.05mm$ (20 MPa) [85]. This discrepancy was attributed to the MMA adhesive undergoing an incomplete polymerization at higher thicknesses due to an inadequate ratio between the activator and adhesive. Watson observed that the bond-line thickness has a statistically significant effect on the TSL [86]. Using a modified rigid-DCB (RDCB) specimen, Watson showed that as the bond-line thickness increases, the elastic stiffness and peak traction of the TSL decrease due to a reduction in confinement effects from the adherends on the adhesive; however, the critical energy release rate increased with increasing bond-line thickness.

Arenas et al. used a Weibull distribution to assess the reliability of adhesive joints and determine an optimized adhesive thickness [83]. It was observed that for thicknesses between 0.4 and $0.8mm$, the failure mode during shear loading is cohesive and the strength increases as the thickness decreases due to the size effect and interface stresses. However, below a layer thickness of $0.4mm$, the distribution of the sample failure modes gradually transitions from cohesive to adhesive. Additionally, the variance in sample performance increases as the layer thickness decreases; while Arenas et al. observed peak adhesive performance at a bond-line thickness around $0.3mm$, the recommended layer thickness using the Weibull distribution for a production-quality joint was around $0.5mm$ to ensure reliable performance [83]. Thus, the objective for adhesive joint design is minimizing the bond-line thickness while ensuring the joint fails in a cohesive manner.

2.3.4. Effect of Temperature on Thermoplastic Adhesive Performance

Establishing the suitability of a thermoplastic adhesive at representative service conditions is an important consideration when designing parts that can operate reliably in extreme cold weather. Thermoplastic adhesive performance – which includes MMA adhesives – may become a

concern at low temperatures, which would limit their effectiveness in cold, harsh climates. In a study that investigated the Mode-I fracture toughness of steel substrates bonded with a ductile polyurethane adhesive, Jia et al. observed that the fracture toughness decreased significantly with increasing loading rate and decreasing temperature, as shown in Figure 2.17 [87]. This was further reflected in work by Nam et al., who found that ductile polyurethane adhesives can become brittle at cryogenic temperatures [88]. To the author's knowledge, an assessment of low temperature Mode I fracture toughness for an MMA adhesive-bonded thermoplastic composite has not been reported in the literature. Similarly, low temperature Mode II (shear direction) fracture toughness has not been reported for a thermoplastic composite bonded with an MMA adhesive, and post-mortem fracture surface analyses of low temperature MMA adhesive joints are not available in the literature. Conversely, MMA adhesives experience increasingly ductile performance at higher service temperatures. Moller et al. demonstrated that MMA adhesives exhibit a decreased maximum load but increased displacement during DCB testing as temperatures increased up to 80°C, with a consequent increase in Mode-I fracture energy [89]. Thus, MMA adhesive performance is generally not a concern at elevated service conditions.

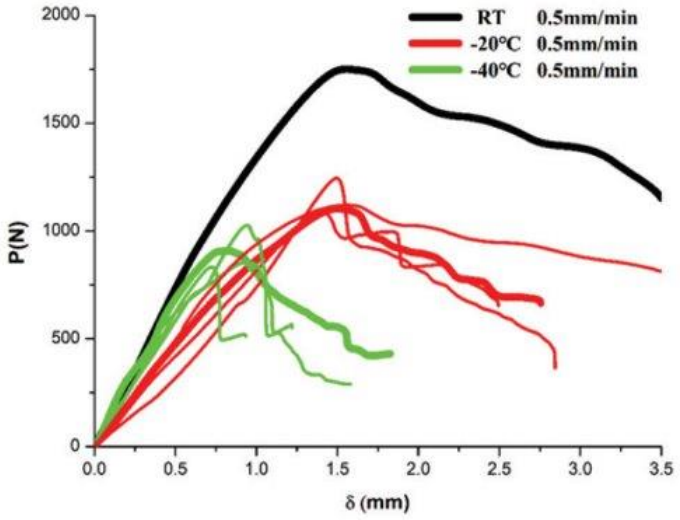


Figure 2.17: Jia et al. demonstrated that temperature has a drastic effect on polyurethane (thermoplastic) adhesive performance at quasi-static loading conditions [87].

2.4. Wind Turbine Blade Manufacturing

2.4.1. VARTM Processes for Wind Turbine Blades

Wind turbine blade manufacturing in industrial applications has settled on VARTM as the most reliable, high-quality production technique available for large-scale structural parts. When processing wind turbine blades, two blade shells are fabricated separately and then adhesively bonded together with a supporting structure (spars) located in the blade cavity. Schematically, the blade is composed of a pressure and suction shell as shown by Figure 2.18 [90].

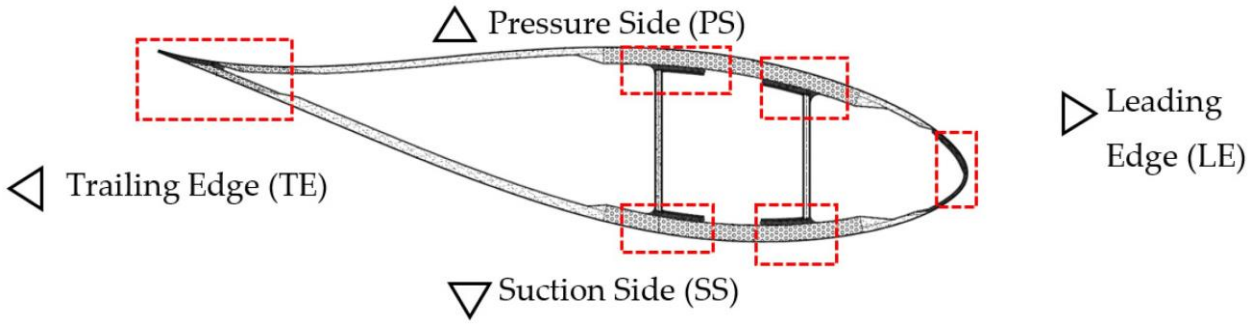


Figure 2.18: Cross-section of generic wind turbine blade highlighting (CW) the Leading Edge (LE), Suction Side (SS), Trailing Edge (TE), and Pressure Side (PS) of the blade, and the interfaces between the blade shells and reinforcement spars [90].

As the scale and geometric complexity of a part increases, the optimization of the inlet gate, outlet vent, infusion lines, and distribution mesh for the VARTM process also becomes increasingly complex, particularly as sharp corners are introduced to the mold and affect the fabric drapeability and permeability [38], [91]–[93]. Apart from the location of the gates and vents, the orientation of the infusion lines (usually plastic tubes with spiral slits) can be used to create preferential resin flow paths. Therefore, the objective of infusion setups for large, complex geometries is to allow multiple flow fronts to cover the planform surface quickly and reach the vacuum vents without causing resin starvation in the part. Figure 2.19 from Chai et al. demonstrates the virtual process chain that is used to optimize a VARTM process for a complex shape [38], [94]. For simpler, smaller parts, simulation models are often replaced with experimental trials that utilize the same cyclic optimization procedure.

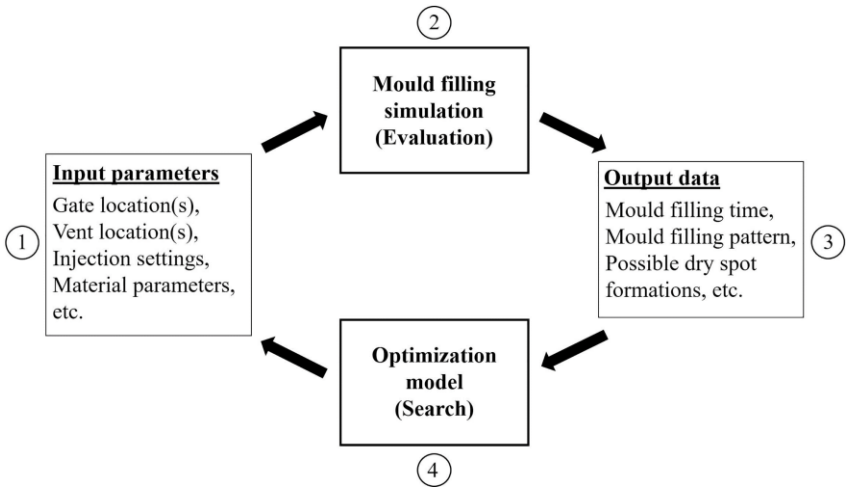


Figure 2.19: Virtual process chain that can be applied to VARTM optimization [38]. *A similar flow chart can be used to experimentally optimize a manufacturing setup.*

Mahendran demonstrated how the distance between infusion lines simultaneously affects quality and efficiency during part production [95]. By reducing the distance between infusion lines, the part can be infused more quickly but with more consumables, while an excessive distance between infusion lines might not allow for complete resin impregnation. Similarly, Mohsin observed that the quality of a panel depends on the planform area covered by the distribution medium [96]. Without any distribution mesh, it was found that the resin was incapable of penetrating the dry laminate stack quickly enough to infuse the panel prior to gelation. Thus, the panel was not fully infused. Conversely, if the distribution mesh completely covered the laminate, large dry spots on the mold-side surface formed due to the transverse flow phenomenon. Mohsin found that covering 80% of the laminate with a distribution mesh allowed complete impregnation of the fabric without premature resin gelation [96].

Micro-generating wind turbine blades may not require complex infusion setups, as shown by Broad [97]. High-quality small-scale blades can be produced with a single inlet infusion line that allows resin to flow across the width of the laminate towards an outlet line on the opposing side. Two outlet vents ensure that the resin flow front is uniform throughout the length of the blade and impregnates the entirety of the root and tip. Figure 2.20 from Broad demonstrates a reliable vacuum infusion line setup developed for small-scale turbine blade manufacturing [97].

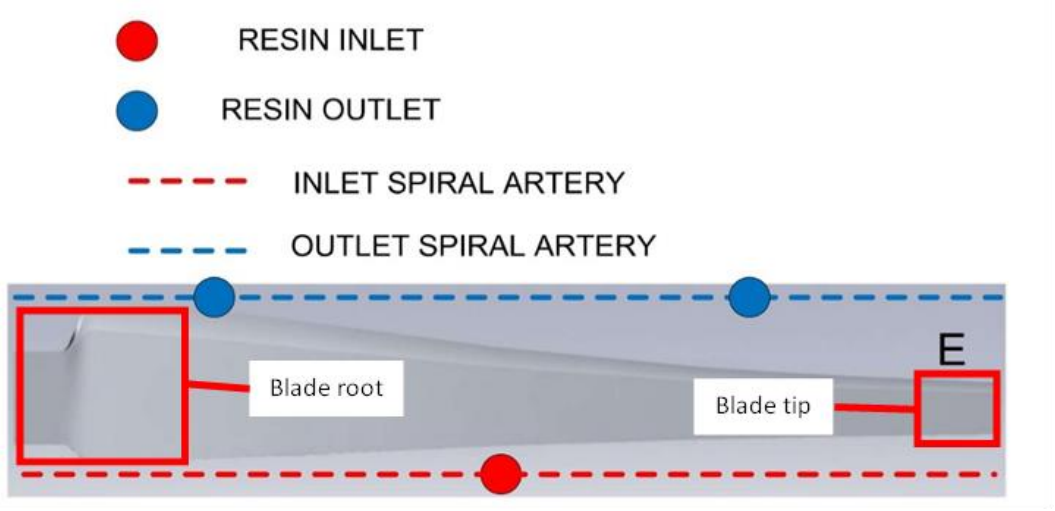


Figure 2.20: VARTM layout for small-scale wind turbine blade including inlet gate, outlet vent, and infusion spiral configurations [97].

2.4.2. Thermoplastic FRP Composites in Wind Turbine Blade Applications

Wind energy is one of the leading potential applications of in-situ polymerizable thermoplastic resins [17]. Adding to the benefits of recyclability associated with thermoplastic resins, the low viscosity associated with in-situ polymerizable resins allows for a drop-in solution for traditional blade manufacturing techniques and a simultaneous reduction in cycle times due to fast thermoplastic polymerization. A recent project investigated the production of a 61.5 m wind turbine blade using Elium® resin and observed a 4.7% reduction in production cost due compared to conventional thermosetting resins owing to lower capital investment, faster cycle times, and reduced energy requirements [17]. This study found that the Elium® FRP samples had comparable mechanical properties with parts produced using an epoxy system. A 13 m blade was also fabricated and tested under both static and dynamic fatigue loading conditions to assess blade integrity – the latter simulating 20 years of operational usage [17]. The blade performance was comparable to similar turbine blades produced with epoxy resin systems. Similarly, Obande et al. observed that Elium® 188 O FRP composite parts exhibit a 33% higher transverse tensile strength and a 15-19% higher fracture toughness than composite parts produced with an SR 1710/SD7820 epoxy system [15].

The processability of the Elium® resin system – related to viscosity, gelation time, exothermic thermal runaway, and volumetric shrinkage – has been investigated in the literature. The viscosity of Elium® 188 XO resin is 0.1 $Pa \cdot s$ at room temperature with an open time between

60 and 90 minutes; most thermosetting resins designed for infusion demonstrate a viscosity between 0.05 and 1 $Pa \cdot s$ [12], [98]. The low viscosity of the Elium® resin enables complete impregnation of the fabric without voids. Resin infusion simulations with Elium® generally assume a uniform viscosity for the duration of the infusion courtesy of the long open time. Khalili et al. modelled the impregnation of a cellulose fabric with Elium® 150 resin assuming a constant resin viscosity for the duration of the simulation and observed a close correlation with the experimental results [99]. Suzuki et al. investigated the polymerization kinetics and temperature evolution for Elium® bulk polymerization during VARTM processing and found that the polymerization conversion rate was sensitive to the concentration of pre-dissolved PMMA polymers in the monomer mixture [100]. Without any pre-dissolved PMMA polymers, thermal runaway was measured and it was observed that the bulk conversion time – and hence the gelation time – for the mixture was approximately 45 minutes. As an amorphous thermoplastic, PMMA does not experience severe volumetric shrinkage during polymerization. Murray et al. observed that the volumetric shrinkage of Elium® glass fiber-reinforced plastic (GFRP) spar caps for a wind turbine blade was less than that of FRP parts produced with epoxy [101]. Volumetric shrinkage of a material during curing/polymerization can induce residual stresses and dimensional warpage in the material and must be considered during part design.

2.4.3. Wind Turbine Blade Assembly

Wind turbine blade assembly techniques depend on the blade scale. During assembly, the geometry of the bonding surfaces between the pressure and suction shells (Figure 2.18) are critical for ensuring sufficient stiffness and strength. Because the strength of an adhesive joint is affected by the part geometry, numerous joint configurations exist depending on structural or form requirements (Figure 2.21) [74].

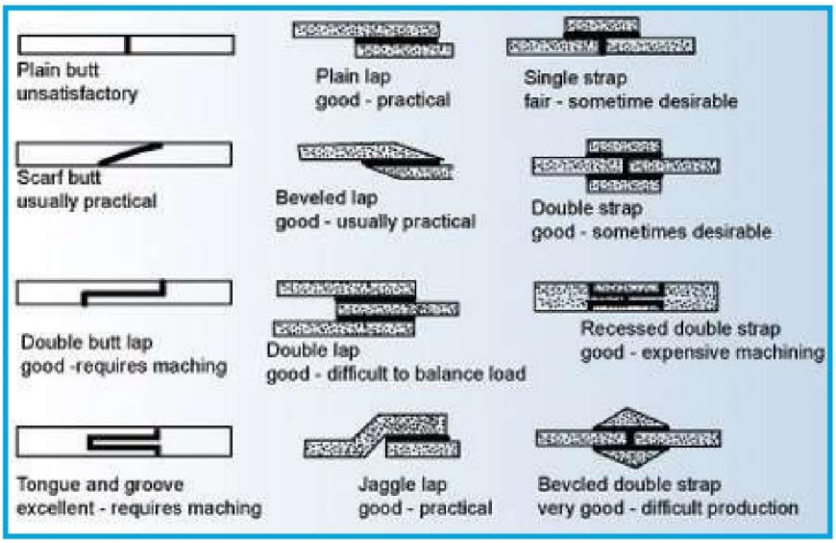


Figure 2.21: Adhesive joint configurations from Petrie with qualitative strength assessment [74].

Single sided strap joints are commonly used in wind turbine blade applications since they combine sound structural support without disturbing the aerodynamic surfaces of the blade [90], [102]. The strength of an adhesive bond is partly governed by the size of the joint overlap, and higher loads can be transferred through an adhesive layer if it covers a large surface area [74]. Per Petrie's recommendation, joint configurations where the adhesive is used to bond along the thickness of a part (such as butt joints) are generally undesirable since the bonding surface area is reduced [74]. Wood recommends a strap joint using a glue dam for small scale blades due to the relatively thin shells and extreme approach angle at the leading edge [20]. Droubi et al. investigated the effect of leading-edge turbine blade joint configurations against deformation due to impact loading [103]. A butt joint, a step joint, and a lap joint were considered, and it was found that the lap joints could withstand loads up to 94% higher than the stepped joints (that experienced the weakest bond due to geometry-induced stress concentrations). Large scale wind turbine blades incorporate these lap joint principles within their internal spar and web supporting structures, and certain small scale wind turbine blades may use a box spar as the leading-edge glue dam [20], [104]. Alternatively, small-scale turbine blades may use an expanding foam (typically epoxy or polyurethane) instead of spars and webs to provide structural support [104].

Chapter 3: Flat Panel VARTM Processing

Taking into consideration the advantages and disadvantages of the VARTM variants listed in Section 2.2.3, SCRIMP was adopted for this thesis due to the relative ease of implementation and improved manufacturing throughput compared to traditional VARTM methods. The focus of this chapter is the optimization of the SCRIMP process for a flat panel. This Chapter will start with a detailed step-by-step summary of the baseline VARTM process setup, which was adopted from the work of Rosso [21]. Next, the iterative process study that was undertaken to optimize the quality of the flat panels is presented.

3.1. Panel Materials

3.1.1. Resin System

The key considerations for a suitable VARTM resin system are low resin viscosity, low processing temperature to reduce energy costs, and low exothermic temperature release to avoid mold damage. The Elium® 188 XO resin system (Arkema, France) provided the necessary compromises to produce micro-generating wind turbine blades via VARTM processes [98]. The technical specifications of the polymerized Elium® resin are shown in Table 3-1 [21].

Table 3-1: Mechanical properties of polymerized Elium® 188 polymer [21].

Shore D hardness	85 – 90		ISO 868
Coefficient of linear expansion	0.065	mm/m/°C	ISO 2155-1
Fracture toughness stress intensity, K_{1C}	1.2	$MPa.m^{0,5}$	ISO 13586
Elongation at break	2.8	%	ISO 527
Flexural strength	111	MPa	ISO 178
Flexural modulus	2.91	GPa	ISO 178
Tensile strength	66	MPa	ISO 527
Tensile modulus	3.17	GPa	ISO 527
Compression strength	116	MPa	ISO 14126
Compression modulus	3.83	GPa	ISO 14126

A benzoyl peroxide solution Luperox® AFR40 (Sigma Aldrich, US) was used as the initiator for the Elium® polymerization reaction. A quantity of 2-3% by weight of the Luperox® initiator was mixed with the Elium® monomer prior to VARTM processing.

3.1.2. Fiber Reinforcement

An E-glass UD-NCF (Saertex US) comprising appropriately sized NEG2026 glass fiber roving (2,400 tex) and supporting glass fiber yarns (275 tex) was selected as the fiber reinforcement [105]. The fabric consisted of warp knitted polyester stitching (110 dtex) in a tricot pattern to bond the glass fiber roving resulting in a fabric aerial weight of 943 g/m^2 (Figure 3.1). The technical specifications of the Saertex fabric are shown in Table 3-2 [105], although the measured stitch length did not match the specified stitch length.

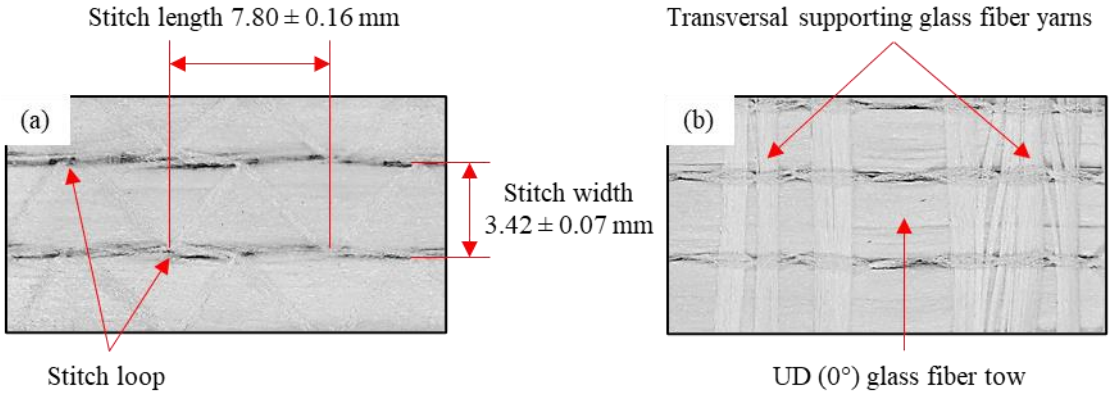


Figure 3.1: Dimensions of E-glass UD-NCF.

Table 3-2: E-glass UD-NCF technical specifications [105].

ARTICLE CONSTRUCTION (in accordance with EN 13473-1)					
Layer	Construction	Areal weight	Tolerance	Material	
2	0 °	850 g/m²	+/- 5.0 %	E-glass 2,400 TEX	
1	90 °	81 g/m²	+/- 5.0 %	E-glass 275 TEX	
Stitching		12 g/m²	+/- 3 g/m²	PES [Polyester] 110 dtex	
FURTHER CHARACTERISTICS					
Gauge	7.0	Stitching pattern	tricot	Width (nominal)	1270 mm
Stitch length	4.00 mm	Total tolerance	5.3 %	Total areal weight	943 g/m²

An E-glass UD-NCF comprising StarRov 090 glass fiber roving (1,100 tex) (Johns Manville, US) [21] and supporting glass fiber yarns was custom fabricated (V2 Composites, US) and used for initial VARTM trials. The fabric contained a warp knitted polyester stitch in a tricot pattern, as

well as a polymeric veil on the transverse yarn side of the glass fiber roving to improve fabric handling and increase inter-laminar resin permeability during processing. This veiled fabric had a lower areal density (< 600 g/m^2) when compared to the non-veiled fabric due to the small roving size. The fabric characteristics are listed below [21]:

- Average thickness = 0.600 mm
- Average roving width = 2.85 mm
- Average fiber diameter = 16 μm
- Stitching pitch distance = 7.50 mm

3.2. Flat Panel Manufacturing – Baseline VARTM Process

3.2.1. Mold Preparation

The mold used for the flat panel trials was a 3.175 mm (1/8 in) thick, aluminum 6061 flat plate measuring 609.6 mm × 609.6 mm (24 in × 24 in). Prior to every trial, the mold surface was cleaned. One coat of Frekote PMC (Henkel, Germany) mold cleaner was applied to the surface of the mold and allowed to cure after 30 minutes. After every 10 processing cycles, the mold received an additional coat of Frekote B-15 sealer (Henkel, Germany) that was applied after the cleaning agent finished curing. The sealer was allowed to set for 24 hours after each application. Four coats of LOCTITE Frekote 770-NC release agent (Henkel, Germany) was applied to the mold surface prior to each process cycle, which required a total of 45 minutes of preparation time. The release agent was essential to demold the FRP panel after polymerization was complete.

3.2.2. Vacuum Infusion Supplies Preparation – Material Stack

The material stack was composed of four layers of UD-NCF (Saertex) with the stacking sequence $[0]_4$, a peel ply (Airtech Econostitch, 381 mm (15 in) wide), a woven distribution mesh (Airtech Greenflow 75 Infusion Media, 1041.4 mm (41 in) wide), and a vacuum bag (33 μm (0.0015 in) thick Airtech Econolon Bagging Film, 1524 mm (60 in) wide). The laminate stack follows the schematic outlined in Figure 2.5. The E-glass UD-NCF layers were cut to 304.8 mm × 304.8 mm (12 in × 12 in). The peel ply layer was cut sufficiently large at 330.2 mm × 457.2 mm (13 in × 18 in) to completely cover the fabric, thus creating a 25.4-38.1 mm (1-1.5 in) inlet flange region and a 76.2 mm (3 in) outlet flange region for the infusion lines. The distribution mesh was cut to accommodate the entirety of the laminate stack and fold around an inlet infusion line that

delivered the resin from a funnel to the mold. The dimensions of the distribution mesh were 304.8 mm × 355.6 mm (12 in × 14 in). The vacuum bag was cut to approximately 508 mm × 508 mm (20 in × 20 in), to cover the entirety of the subsequent sealant tape periphery.

The manufacturing process described in this section was used to produce 304.8 mm x 304.8 mm (12 in × 12 in) GFRP panels using the non-veiled fabric. Earlier trials used the veiled fabric to produce panels measuring 154.2 mm x 304.8 mm (6 in × 12 in), and certain sections in this chapter show the results of the experimental trials with the smaller, 154.2 mm × 304.8 mm GFRP panels. However, the outlined manufacturing process refers to the consumable dimensions and resin quantity required for the larger, 304.8 mm × 304.8 mm GFRP panels. Apart from the quantity of consumables required, the manufacturing techniques were consistent for both sets of panels.

3.2.3. Vacuum Infusion Supplies Preparation – Infusion Lines

The infusion line system included clear, UV-resistant PVC tubing for the resin inlet and outlet lines. The inner and outer diameter of the inlet and outlet tubing were 9.525 mm (3/8 in) and 12.7 mm (1/2 in), respectively. Two tubes approximately 500 mm long were cut for the inlet (to the resin reservoir) and outlet lines (to the vacuum trap).

3.2.4. Laminate Layup

The laminate setup arranged the materials from Section 3.2.2 and 3.2.3 starting with the E-glass UD-NCF layers stacked symmetrically with the tricot stitching side of the fabric facing the mold and vacuum bag. A spray-tack adhesive from 3M was used to hold the fabric layers together during lay-up and was gently sprayed to each layer around the center. The spray tack adhesive was used to accelerate the workflow by building the laminate stack while the mold underwent curing for the release agent. Additionally, the spray tack adhesive would improve the alignment of the fiber tows between layers during layup and reduce the risk of fiber misalignment during handling and processing. However, literature studies show that spray tack adhesives can increase laminate fill times during VARTM processing by 30% although influences on porosity and fiber volume fraction are negligible [106]. Generally, spray adhesives are designed to be non-reactive with matrix resin systems and they can have an effect on part properties including glass transition temperature [107].

The UD-NCF stack was oriented to allow the resin to flow along the transverse fiber direction (i.e, the laminate stack was oriented 90° to the resin flow direction as shown in Figure

3.2), reducing the resin velocity and minimizing the risk of void generation from dual-scale flow. The spray-tack adhesive was gently applied to the upper fabric layer, and the peel ply was placed on the fabric stack with sufficient flange area around the inlet and outlet to accommodate the infusion lines. The mold was then degreased with acetone around the material stack to remove debris before placing sealant tape (Airtech AT-200Y Sealant Tape – yellow) around the periphery. The dimensions of the sealant tape profile around the laminate were 406.4 mm × 508 mm (16 in × 18 in) to allow space for the infusion lines. The distribution mesh was placed on the laminate and covered nearly the entirety of the laminate stack. The inlet line was fed from the corner of the sealant tape periphery, culminating at the middle of the inlet flange. Similarly, the outlet line was fed from the opposite corner of the sealant tape periphery into a fold in the peel ply. The outlet line was connected to a resin trap that fed into the vacuum pump. Figure 3.2 shows the laminate lay-up with the resin flow direction highlighted.

3.2.5. Application of Vacuum Bag

The primary objective during application of the vacuum bag was to avoid air leakage from the mold, which would otherwise inhibit resin infusion and fiber wet out. Thus, the vacuum bag was gradually pressed into the sealant tape around the entire periphery, with care being taken to avoid wrinkles that may contribute to air leakage. The sequence of operations for application of the vacuum bag is summarized in Figure 3.2a, with the orientation of the laminate stack highlighted.

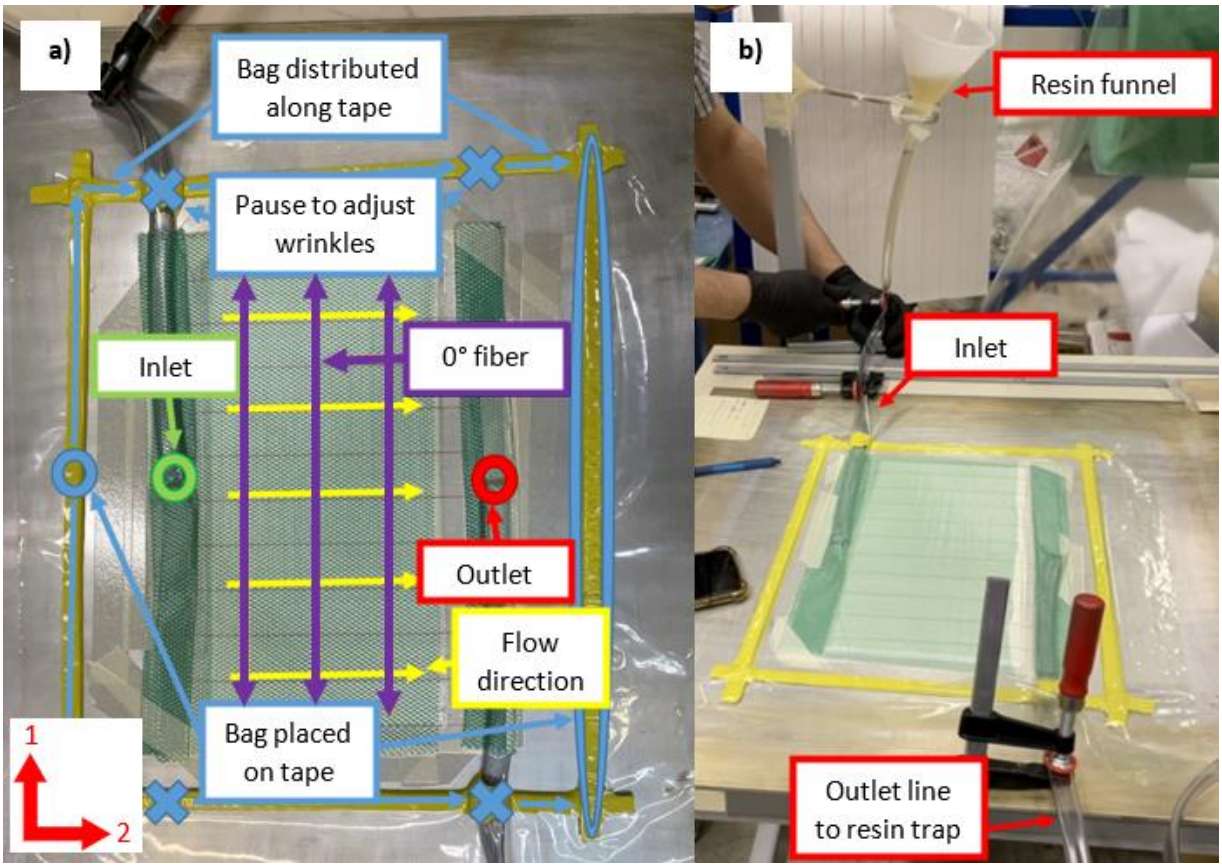


Figure 3.2: Baseline VARTM setup; (a) vacuum bagging technique schematic for a smaller, 154.2 mm x 304.8 mm (6 in × 12 in) GFRP panel. The same technique was applied to larger panels outlined in this section. The resin flow direction is highlighted, and (b) full setup with infusion lines and resin funnel highlighted.

Upon completion of the vacuum bagging procedure, the inlet line was completely shut and vacuum was applied, allowing the bag to collapse onto the laminate. The VARTM process used a Leybold Trivac D30A (Leybold, Germany) vacuum pump. The bag was left under vacuum for 5-minutes to ensure that all air was evacuated, after which the vacuum valve was closed. The vacuum level in the mold was recorded around 29-29.5 inHg, which indicated a perfect seal for this pump. If the pressure inside the bag was maintained at around 29-29.5 inHg after a 25-minute drop test, the vacuum seal was sufficient for infusion.

3.2.6. Resin Mixing

The total resin quantity required when using the Saertex UD-NCF layers was 180g. The resin was combined with 2-3% by weight of the benzoyl peroxide initiator and mechanically mixed using a wooden stick in a disposable reservoir for 8-minutes, which provided a suitable homogenous consistency and viscosity. Subsequently, the resin was poured into a funnel elevated

above the workstation (Figure 3.2b). The mixed resin was allowed to sit for 5 minutes prior to the infusion to allow any entrapped air bubbles from the mixing process to escape.

3.2.7. Resin Infusion and In-Situ Polymerization

Flow control during the resin infusion process was dictated entirely by a C-clamp on the inlet hose and another on the outlet hose. With the pump running and the outlet line open, the C-clamp was released on the inlet side. The resin immediately began flowing down from the funnel into the mold before quickly flowing through the distribution mesh. Once the laminate was completely infused, the inlet and outlet lines were left open temporarily to evacuate any residual air bubbles. The inlet line was closed once air began flowing into the funnel (average infusion time of 2-3 minutes), while the outlet line was closed once the resin reached the perimeter of the sealant tape to prevent resin from being pulled into the resin trap. At this point, the vacuum pump was shut off, and the laminate was left to polymerize. The Elium® 188 XO/ Luperox® AFR40 resin system required three hours to fully polymerize at room temperature after the vacuum was shut off.

3.2.8. Panel Demolding and Mold Cleaning

Brass putty knives were used to demold the polymerized FRP panels. After breaking the vacuum seal between the mold and panel surfaces, the putty knives were used to gradually apply more pressure until the panel was completely removed from the mold. The mold was thoroughly cleaned after each cycle to maintain longevity. First, the solidified resin on the periphery of the panel was removed with the putty knives, upon which the mold was wet sanded thoroughly with 180 grit sandpaper until the mold surface was consistently smooth. At this point, the dirt, grime, and water were completely wiped off with paper towel, and the mold surface was cleaned with acetone before following the mold preparation procedure described in Section 3.2.1.

3.2.9. Baseline Panel Quality

The baseline panels routinely suffered from resin starvation around the resin inlet region (i.e., the leading edge of the resin flow after evacuating the inlet line). Resin starvation was observed around the first half of the panel, while the second half of the panel (i.e., the outlet region) was infused to a comparatively high quality with voids observed less regularly. The resin starvation could be qualitatively assessed by the color of the panel (Figure 3.3).

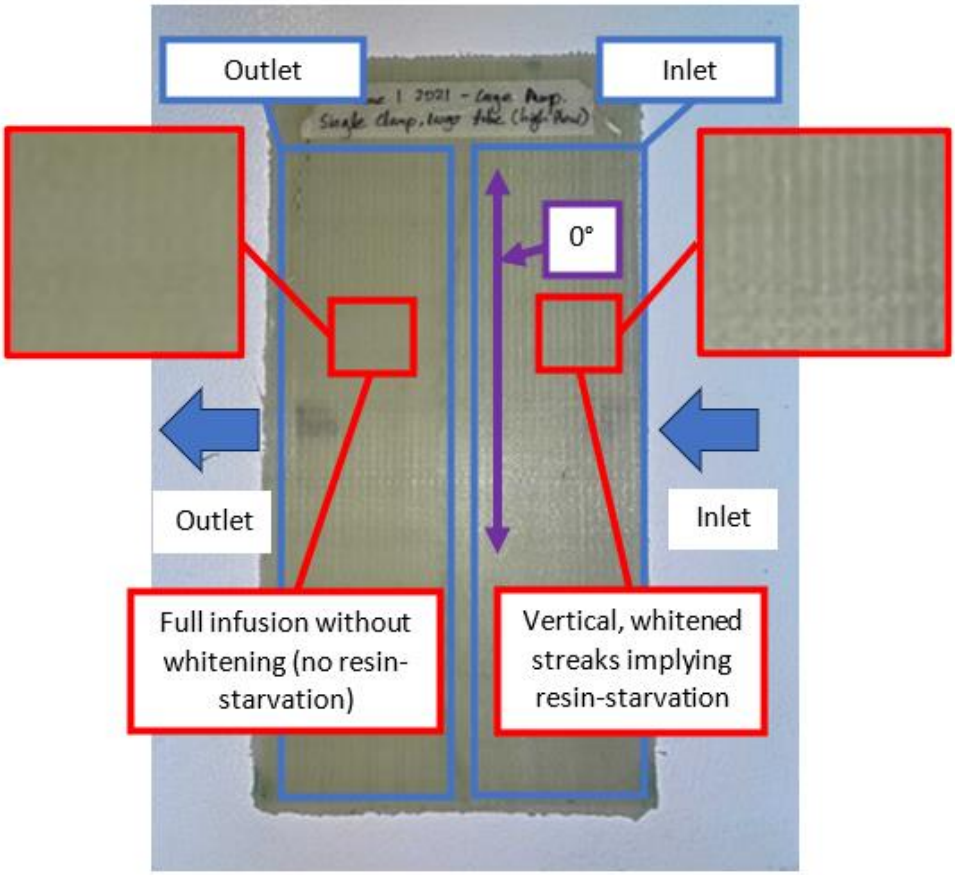


Figure 3.3: Images of 152.4 mm × 304.8 mm (6 in × 12 in) baseline GFRP panels. The panels exhibited consistent resin starvation, particularly around the inlet region (highlighted).

The distribution of the void content through the panel does not correlate with expected results from the literature, where the outlet region is generally expected to experience higher void contents due to lower fluid pressure [48]. Thus, it can be inferred that the baseline VARTM process contained fundamental flaws, possibly in the laminate compaction, that caused an increased void distribution around the inlet of the panels.

3.3. Flat Panel Manufacturing – VARTM Process Improvements

The following sections summarize additional process trials with modifications implemented to the VARTM process aimed at improving the quality and reproducibility of the flat FRP panels. Many of these additional processing trials utilized the veiled UD-NCF 152.4 mm × 304.8 mm (6 in × 12 in) panels, while in latter trials the non-veiled UD-NCF was used 304.8 mm × 304.8 mm (12 in × 12 in) panels.

3.3.1. Vacuum Pump Test

The initial trials described in Section 3.2 used a Leybold vacuum pump that provided a pressure of 29 inHg. Additional trials were performed with a weaker, Welch 2534B-01 piston vacuum pump (Welch, USA) that provided a pressure of 25.5 inHg. The overall part quality was superior with the use of the larger vacuum pump. Parts fabricated with a pressure of 25.5 inHg contained significant void content throughout (Figure 3.4). By contrast, the panels infused at a higher pressure contained voids and resin-starvation near the inlet while the outlet region was fully impregnated (Figure 3.3). Thus, the higher-power 29 inHg vacuum pump was used for the remainder of the trials.

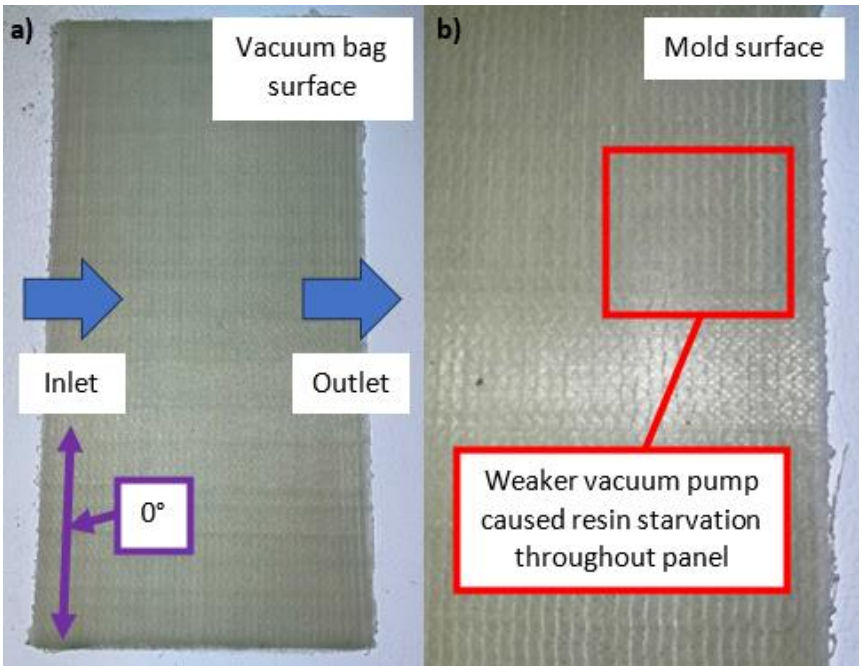


Figure 3.4: Images of 152.4 mm × 304.8 mm (6 in × 12 in) GFRP panels (mold side shown) fabricated with a vacuum pump providing 25.5 inHg pressure for the (a) vacuum bag side and (b) mold side. The weaker vacuum pump was incapable of completely impregnating the laminate.

3.3.2. Flow Rate Test

Preliminary VARTM trials focused on the flow rate of the resin into the mold by adjusting the diameter of the inlet tubes and changing the clamping pressure. It was hypothesized that a reduction in the flow rate might reduce void formation by limiting the proliferation of dual-scale flow; however, results did not conclusively demonstrate that a reduction in the diameter of the inlet tube had a noticeable influence on the panel quality. Changing the inner diameter of the inlet tube from 9.525 mm (3/8 in) to 6.35 mm (1/4 in) without any further modifications did not

influence the resin starvation effect observed around the panel inlet, implying that the pressure losses from the tubular flow were not significant enough to influence part quality. As a result, an inlet tube diameter of 3/8 inches was retained. Previous studies have show that choking the inlet flow and allowing the resin to bleed into the outlet vent can allow voids to be transported out of the mold [48].

Subsequent trials attempted to optimize the inlet clamping pressure and choke the flow into the mold for the smaller, 152.4 mm × 304.8 mm (6 in × 12 in) panels. Each trial was timed with a stopwatch to correlate the quality of the final part with the infusion time. Figure 3.3 in Section 3.2.9 demonstrated the effect of a large diameter tube without any choking of the inlet line. The infusion time was under 3 minutes, and the final part contained significant void content. The next trial applied moderate clamping pressure on the inlet line to choke the flow, with the infusion time rising to 5 minutes. Moderate clamping pressure yielded the first high-quality panel without significant void content recorded during the optimization process. To discover the upper limit of the infusion time, the inlet line was choked even further for the third trial, leading to an infusion time of 8 minutes. Like the high-quality moderate flow trial, the inlet region of the panel did not contain any macro-voids since the reduced flow rate enabled full impregnation of the dry fibers. However, the momentum of the flow was arrested enough that the panel was not entirely infused near the outlet. Thus, an estimated upper limit for the infusion time was confirmed for a high-quality panel, and future trials with 152.4 mm × 304.8 mm panels aimed for an infusion time around 5 minutes. A comparison between the high-quality panel with a 5-minute infusion time and the poorer quality panel with an 8-minute infusion time is shown in Figure 3.5. All subsequent trials employed the same inlet tube clamping technique (flow rate) to ensure a target infusion time matching that of the high-quality panels.

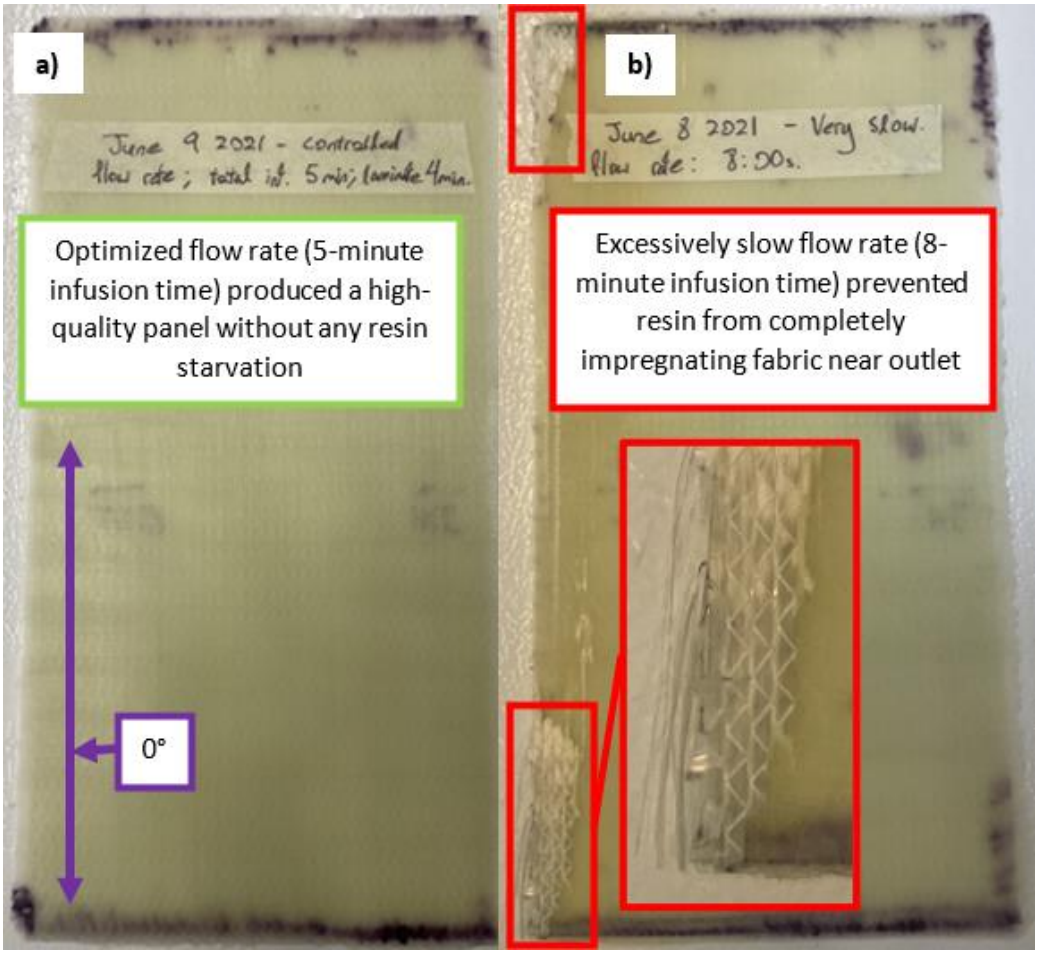


Figure 3.5: Comparison between flow rate trials; (a) partially choking the resin flow rate at the inlet with a C-clamp produced the first high-quality panel of the infusion trials without significant void content, and (b) the inlet flow rate was significantly choked to find the upper limit of the resin flow rate for a successful trial. With an infusion time of 8 minutes, the resin was incapable of fully wetting-out the trailing edge of the laminate.

3.3.3. Degassing Chamber

Despite notable improvements in panel quality stemming from the vacuum pump and inlet line clamping pressure adjustments, further trials were inconsistent and void formation was frequently observed near the inlet. Anticipating that the void formations were the product of air bubbles in the resin, a vacuum chamber-degassing procedure was applied to the mixed resin. The objective with resin degassing is to eliminate the micro-bubbles that may form during mixing [108], [109]. These bubbles can expand under vacuum and cause voids in the final part. Thus, resin was degassed in a vacuum chamber at 25.5 $inHg$ for 15 minutes prior to infusion.

The finished panel using the degassing chamber still exhibited resin starvation near the inlet, and it was deduced that the process inadequacies were fundamentally related to the

uniformity of the atmospheric compaction on the vacuum bag instead of bubbles in the resin mixture. While the V_c of the panels may be improved with a degassing chamber (or with an advanced VARTM process such as VAP or CAPRI), the void formations pointed to a fundamental flaw in the vacuum bag setup that was contributing to poor infusion quality. Images of the resin degassing process and subsequent panel are shown in Figure 3.6. Note, subsequent VARTM processing trials did not use the resin degassing process described in this section.

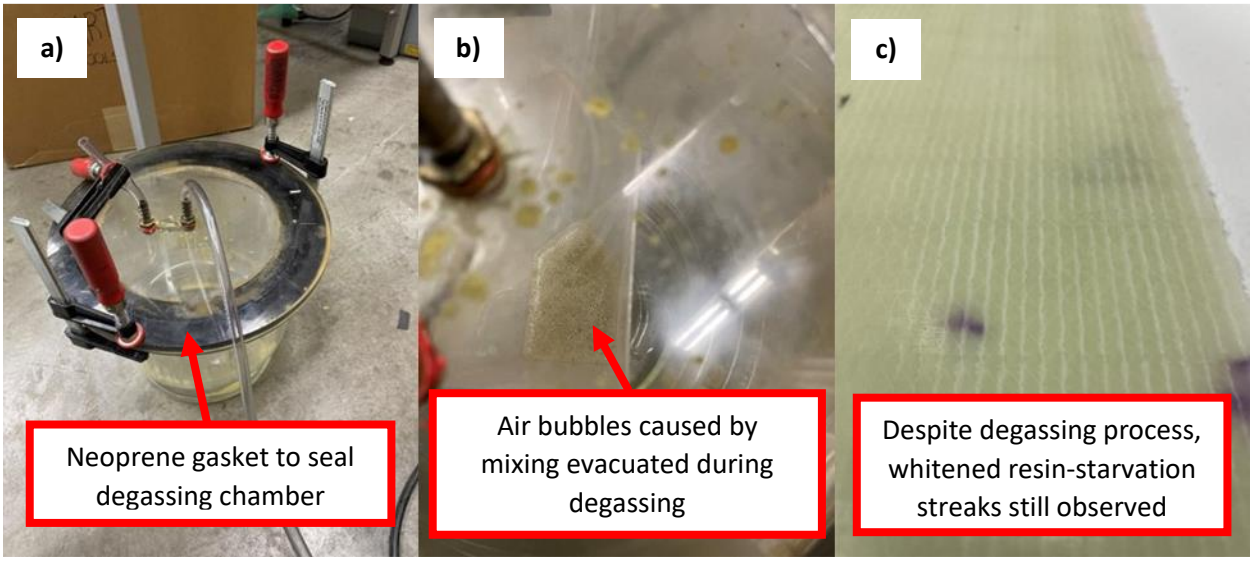


Figure 3.6: Degassing chamber trial; (a) degassing chamber with neoprene gasket (black) to ensure perfect seal, (b) resin bubbling and degassing under vacuum in the chamber, and (c) panel produced with degassed resin still demonstrated significant void formations.

3.3.4. Resin Reservoir

An investigated cause for the consistent resin starvation was the added gravitational pressure due to the height of the funnel above the laminate. Additional gravitational pressure can increase the fluid pressure and overwhelm the distribution mesh, causing pooling and excess resin near the inlet lines [110]. Thus, VARTM setups often place a reservoir below or even with the height of the laminate to reduce the effect of gravitational pressure, resulting in an increase in laminate compaction. Thus, trials were performed with a reservoir system in place of the funnel described in the baseline setup; however, the resin starvation problem was not alleviated. Nonetheless, the reservoir setup was easier to handle, since the reservoir could be securely fastened to the workstation, and the reservoir setup was adopted for all future trials (Figure 3.7).

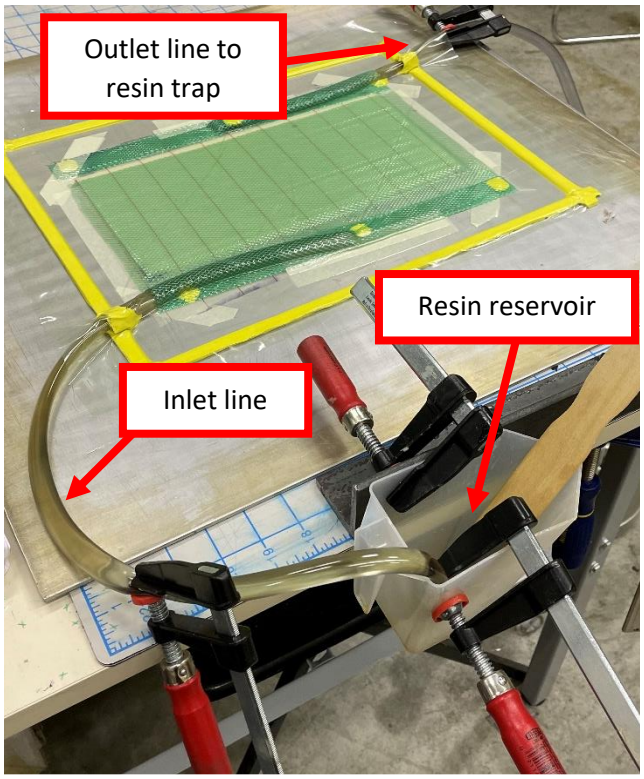


Figure 3.7: Resin reservoir setup that replaced the baseline resin funnel setup due to ease of implementation. Part quality was not noticeably affected by the setup change.

3.3.5. Line Inlet vs. Point Inlet

The baseline VARTM setup introduced the resin into the mold at a single point inlet that would routinely cause an oval-shaped resin flow front due to a permeability discrepancy in the longitudinal and transverse fiber directions. This anisotropy is a source of caution in the literature, as multiple point inlets can create situations where air pockets are trapped in the laminate and the outlet vent is incapable of advancing the flow through these localized dry spots [39]. This becomes a significant risk along the edges of a laminate, since race-tracking behavior can advance the resin flow front aggressively and trap air within lagging flow fronts [11]. Molds with complex shapes can also become susceptible to resin starvation due to non-uniform fabric permeability. Unlike point inlets, spiral infusion lines (line inlets) allow the resin to preferentially flow along a certain geometry in the mold before penetrating the laminate uniformly, allowing for increased control over the resin flow. Thus, line inlets limit the potential for resin starvation by uniformly accelerating the entire flow front. For this work, infusion spirals were trialled in 3 formations to investigate the flow front uniformity.

The infusion line system retained the PVC tubing from the baseline setup but added polyethylene spiral infusion lines to control the flow of resin inside the mold, and barbed nylon plastic pipe-tees to connect the lines together. The outer diameter of both the spiral tubing and pipe-tees was 9.525 mm, however the tubing could be wrapped around the pipe-tees. The first infusion line setup fed the inlet tube into a pipe-tee that redistributed the resin along the leading edge through the infusion spiral. The spiral tubing was placed on the inlet flange over-top of the distribution mesh with the pipe-tee located directly in the middle of the spiral (Figure 3.8a). The length of the spiral was 254 mm (i.e., shorter than the length of the distribution mesh). Despite consuming more resin than a point inlet as the infusion spiral retained a certain quantity (275g compared to 180g described earlier), the resulting uniformity of the flow front enabled a flexibility in the pipe-tee setup that was desirable from a processing perspective.

The second infusion line setup fed the spiral line into the mouth of an inlet tube placed at the corner of the mold without using a pipe-tee (Figure 3.8b). This solution was marginally simpler to implement than the first, but the flow front of the resin was less uniform. A consequence of this non-uniformity was that the leading flow was along the edge of the laminate where the highest degree of race-tracking was expected. Thus, the second infusion line layout exacerbated the race-tracking effect along the laminate edge without meaningfully reducing the resin consumption (since the length of the inlet tube and infusion spirals were identical to the first setup). The problems with the distorted flow front would be exaggerated when upscaling the setup for a full-scale turbine blade shell. Since the blade was longer than the width of the flat panel by a factor of 3, there would be a larger disparity in the flow front between the root and the tip.

The third infusion line setup connected two inlet tubes with a pipe-tee outside of the mold before feeding the tubes into the mold on either side of an infusion spiral (Figure 3.8c). The objective with this solution was to equalize the flow on either side of the laminate while preventing the distorted flow front observed with the second solution. Experimental results showed that this approach could induce symmetry in the flow front on either edge of the panel, but the flow along the middle of the panel lagged either edge. Thus, the panel was susceptible to race-tracking behavior on either edge of the laminate. Additionally, the resin consumption with this solution was the highest since the inlet lines were doubled.

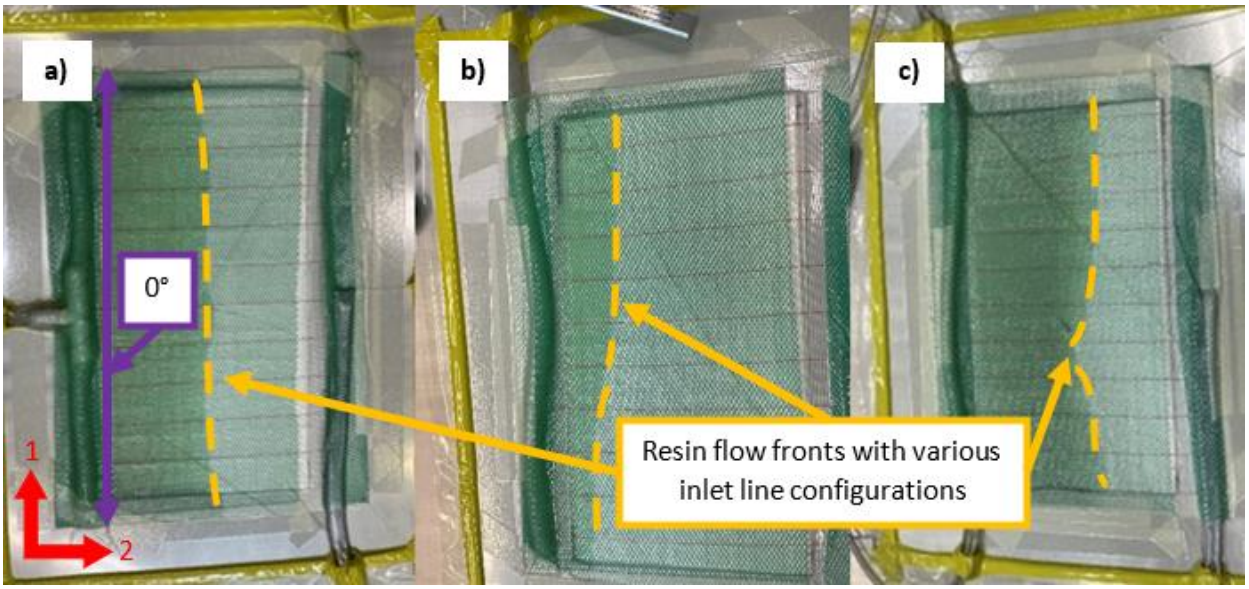


Figure 3.8: Line infusion setup trials; (a) setup #1 with inlet line fed into infusion spiral at center of spiral, leading to uniform flow front across the panel surface, (b) setup #2 with inlet line fed into infusion spiral at end of spiral, leading to lagging flow front emanating from end of infusion spiral, and (c) setup #3 with two inlet lines fed into infusion spiral at either end of spiral, leading to lagging flow front emanating from the center of infusion spiral.

Taking into consideration the resin consumption, the uniformity of the flow front, and the potential for upscaling the process for the full-scale blade shells, the first infusion line setup was adopted for all future trials.

3.3.6. Distribution Mesh Adjustments

Acknowledging the influence of the resin flow rate into the mold, experimental trials were performed that modified the dimensions and orientation of the distribution mesh. While high-quality panels could be produced by choking the inlet line with a C-clamp as shown in Section 3.3.2, this process was unreliable without a flow meter or another quantifiable means for controlling the clamping pressure. Conversely, manipulating the layout and orientation of the distribution mesh provided a quantifiable method for controlling resin flow speed through the laminate. As explained by Advani, the utilization of a distribution mesh was initially pioneered in the SCRIMP process to allow the resin to preferentially flow through a higher permeability layer on top of the laminate [11]. Thus, the distribution mesh can be strategically cut to control the resin flow.

VARTM processes without a distribution mesh generally demonstrate a bulk planar flow through the thickness of the laminate. As discussed in Section 2.2.2.1, this assumption cannot be

made with SCRIMP processes due to the transverse flow phenomenon caused by the large discrepancy in permeability between the top and bottom of the laminate. To reduce the overall effect of transverse flow, the surface area of the distribution mesh can be reduced to gradually decelerate the flow front. Additionally, the distribution mesh contained an anisotropic diamond pattern, and the permeability of the mesh would reduce along the width of the diamond. Thus, the orientation of the mesh could also be manipulated to control the resin flow rate.

In conjunction with the voids generated by the transverse flow phenomenon, it was theorized that the race-tracking effect could also be minimized by strategically modifying the distribution mesh layout. To combat the race-tracking issue, the distribution mesh could be cut narrower such that the edge of the laminate was uncovered on either side of the mesh, allowing the resin to initially penetrate the middle of the laminate stack before flowing laterally to the edges and accelerating via race-tracking along the perimeter. Experimental trials showed that, despite the race-tracking effect persisting due to the increased permeability along the edges of the laminate, the temporary delay in the resin reaching the edges reduced the likelihood of resin starvation towards the laminate outlet.

Iterative trials settled on a distribution mesh setup where the mesh was cut smaller than the fabric layers, with dimensions of 203.2 mm × 266.7 mm (8 in × 10.5 in). Thus, the flow towards the edges of the fabric could be temporarily arrested to minimize the race-tracking effect. Furthermore, the mesh was oriented such that the resin flowed along the width of the woven diamond pattern to minimize the risk of void generation caused by transverse flow. To incorporate the findings from the flow rate trials, the resin flow at the inlet was also controlled via pressure from the C-clamp. Thus, the distribution mesh could be fully impregnated after 30 seconds, after which the C-clamp was removed entirely. At this stage, the resin flowed through the thickness of the fabric and the permeability of the laminate was significantly reduced. Combined with the planar flow through the laminate without a distribution mesh, the entire infusion lasted approximately 15-20 minutes for a 304.8 mm × 304.8 mm (12 in × 12 in) panel. Figure 3.9 demonstrates the preferential flow of the resin through the distribution mesh prior to reaching the laminate edges and initiating the race-tracking effect.

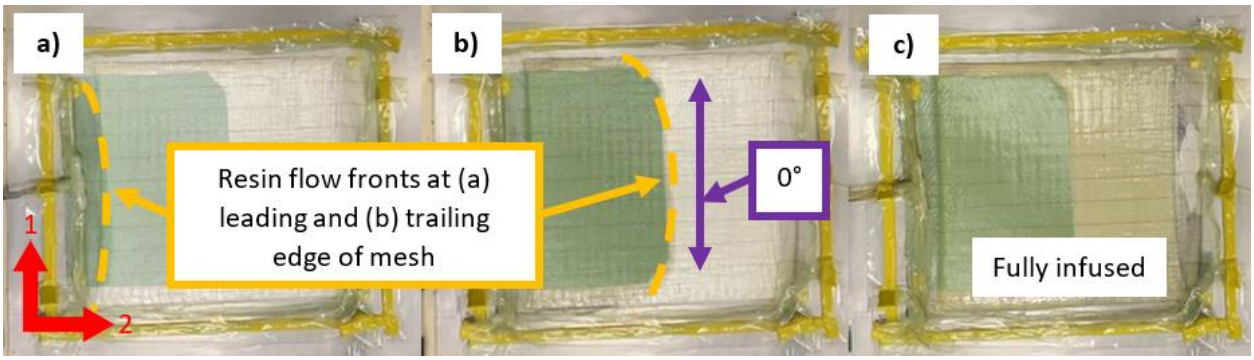


Figure 3.9: Resin flow front at various stages of the infusion process; (a) infusion inlet spiral allowed the resin to span the width of the distribution mesh prior to flowing across the laminate, creating a uniform flow front, (b) the resin flow completely impregnated the distribution mesh after approximately 30 seconds. The flow front along the laminate edges is slightly delayed, limiting race-tracking, and (c) full infusion of the laminate required around 15 minutes for a GFRP laminate with an $[0]_4$ stacking sequence.

3.3.7. Vacuum Bag Pleats

Despite minimizing the transverse flow and race-tracking effects by adjusting the distribution mesh layout, resin starvation was still consistently observed. Thus, it was proposed that vacuum bag bridging might be limiting the laminate compaction uniformity and preventing the resin from properly impregnating the fabric stack. Trials were performed with bag pleats placed strategically to allow the bag to conform to complex geometries without bridging. Even flat panel molds contain out-of-plane geometries – for instance, inlet and outlet tubing – that, without pleats, result in vacuum bag bridging and resin pooling. By placing additional bagging material around the inlet and outlet tubes, the bag can wrap around the features adequately and limit resin pooling. Taking inspiration from the findings by Bloom et al., it was theorized that bag bridging around the infusion lines was contributing to weak compaction leading to poor resin impregnation around the inlet region of the laminate [42].

To accommodate the pleat setup, the vacuum bag size was increased to approximately 609.6 mm × 685.8 mm (24 in × 27 in) for the 304.8 mm × 304.8 mm panels to provide sufficient excess bagging material. Like the schematic in Figure 3.2a showing the order of operations for the pleat-less vacuum bag setup, a systematic, numbered approach was adopted for the pleated vacuum bags (Figure 3.10).

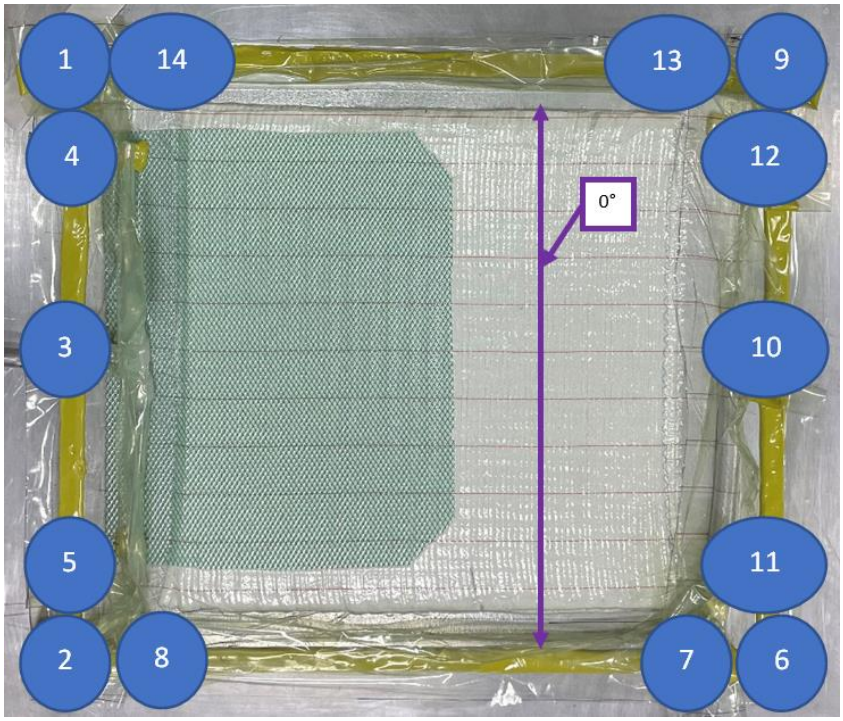


Figure 3.10: Sequence of operations during flat panel vacuum bag processing. The corner sections labelled '1,' '2,' '6,' and '9' do not require pleats, and the bagging film is simply pressed into the sealant tape.

The operations at each corner – labelled '1,' '2,' '6,' and '9' – did not require pleats, and the bag was simply pressed into the sealant tape. The remaining numbers highlight pleat locations in the vacuum bag in the order they were applied. There were two types of pleat techniques that were required for this process, that will be referred to as pleat technique *A* and *B* in this thesis. Pleat *A* was used to anchor the vacuum bag along the middle of the sealant tape at locations '3' and '10', while pleat *B* was used to connect the central anchors to the corners of the sealant tape. The techniques for the different pleats could be applied to virtually any flat or neat-flat mold. The procedure for pleat *A* is visually described in Figure 3.11 below. The procedure for pleat *B* is explained in Figure 3.12 below. Using these methods, the entirety of the vacuum bag was sealed with sufficient excess material to prevent bag bridging. Special interest was paid to pleat '7' in Figure 3.10 which followed a similar procedure as pleat *B* in Figure 3.12, except that the pleat was located on the outlet line. After sealing the vacuum bag, the entirety of the vacuum bag was pressed into the sealant tape to ensure a good seal.

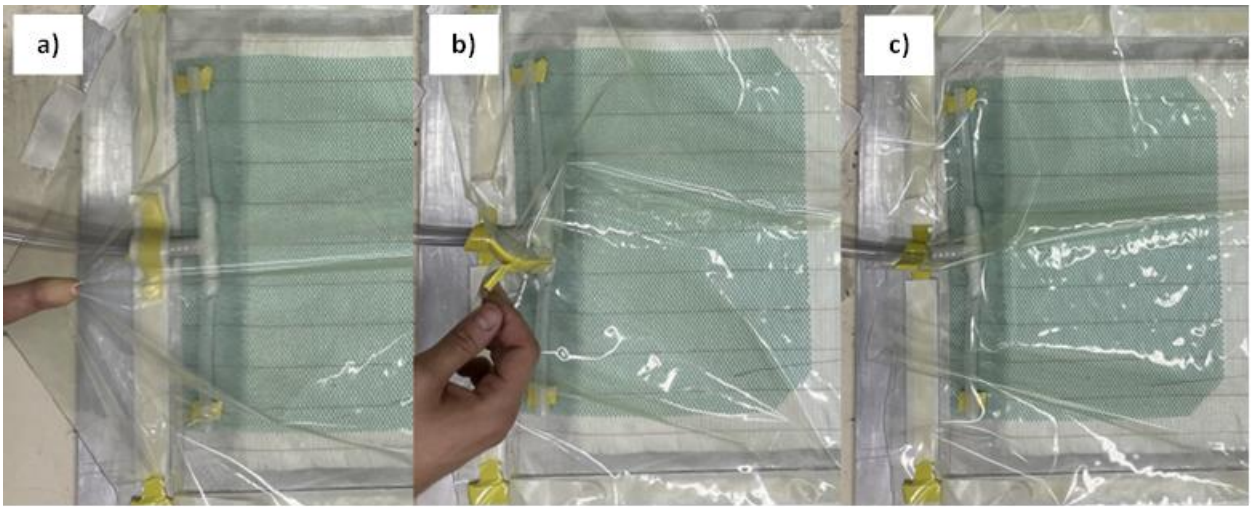


Figure 3.11: Pleat A explained in a 3-step process; (a) the center of the bag between two corners is located. A strip of sealant tape is stuck to the middle of the bag, (b) the sealant tape is folded on itself, forming a pleat, and (c) the pleat is placed on the sealant tape periphery. The area between the central pleat and the corners is not yet taped.

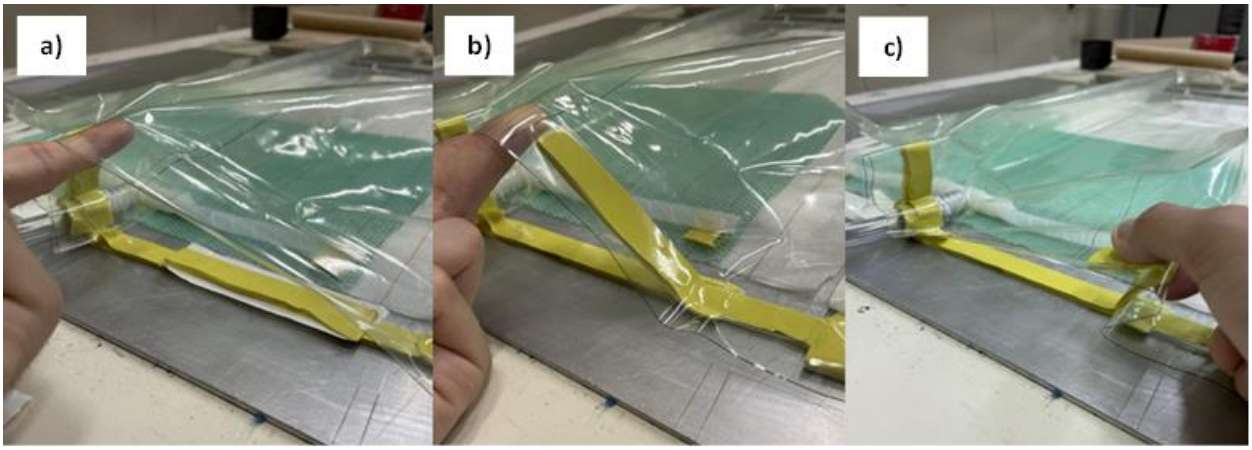


Figure 3.12: Pleat B explained in a 3-step process; (a) a strip of sealant tape was placed on the periphery, (b) the vacuum bag was pressed onto the extra sealant tape and taped to the periphery, and (c) the sealant tape was folded on itself under tension to gradually form the final pleat.

After completing the pleated bag procedure, wrinkles formed due to the excess bagging material that could create race-tracking channels under vacuum. To minimize the wrinkle formation, the inlet line and vacuum gauge valve were left open as the vacuum was pulled to allow increased control of the vacuum bag as it started to settle. This step allowed wrinkles in the bag to be moved away from the laminate. At the inlet and outlet flanges, the wrinkles were adjusted to wrap around the infusion lines, ensuring a good compression and minimizing resin pooling. Figure 3.13 shows the bag with partial vacuum before and after the wrinkle adjustment. Once the vacuum

bag was in a desirable condition, the inlet line was fully clamped and the vacuum gauge was fully opened, allowing the bag to collapse onto the laminate.

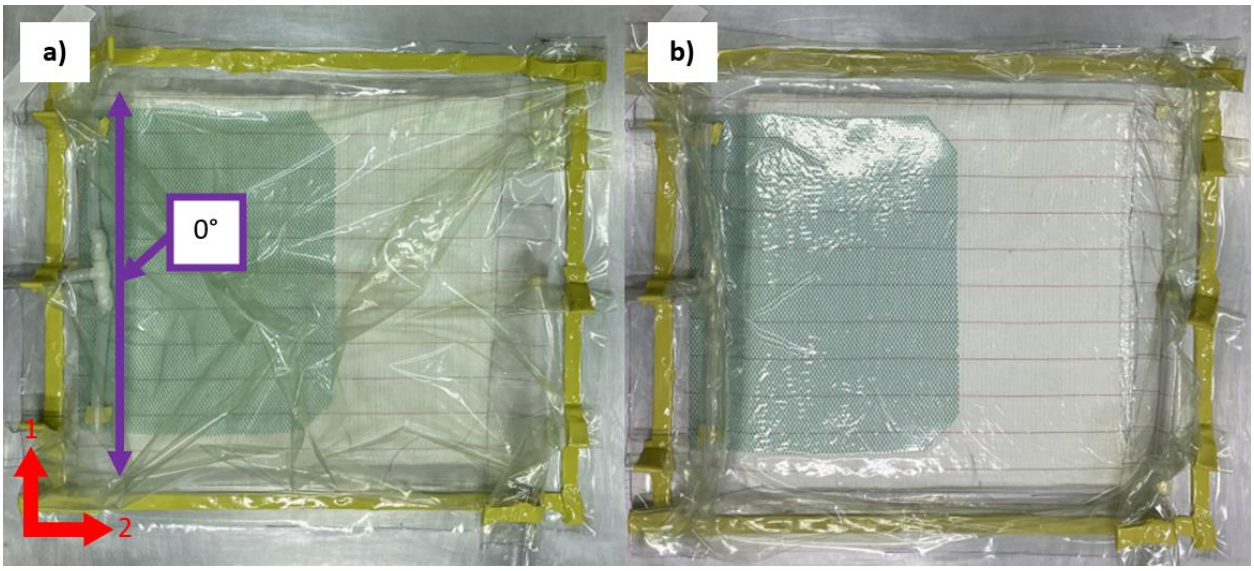


Figure 3.13: Vacuum bag comparison under partial vacuum (a) before and (b) after wrinkle adjustment.

From an industrial perspective, pleats grant operators increased error margin during part processing since any excess slack in the bag can be mitigated by adjusting the length of the pleat. However, the most valuable aspect of pleats is their ability to allow the vacuum bag to conform to the entirety of the mold while maintaining maximum pressure on the laminate during an infusion, minimizing the formation of resin dry spots. Thus, pleats were adopted for all future trials, and reliably improved the quality and consistency of the flat panel parts.

3.3.8. Caul Plate Trials

A preliminary functional requirement for the VARTM process was the improvement of the surface quality on the bag-side of the part. Generally, RTM processes with two-part rigid molds are the standard industrial solution for smooth surface finishes on both sides of an FRP part [41]. For these processes, large presses are needed to withstand the above-atmospheric resin pressure required to fill the mold. For flat surfaces that require uniform pressure or tight dimensional tolerances, caul plates can be adopted as a cost-effective method to improve the surface finish of VARTM parts [11]. To investigate the effectiveness of a caul plate for improving surface quality, flat panel VARTM trials were conducted using a glass caul plate to allow a clear view of the flow front during the infusion.

For the caul plate trials, the plate was placed directly on top of the peel ply without a distribution mesh. The first setup used an oversized caul plate that exceeded the planform area of the laminate, which created a high-permeability vacuum under the flanges of the caul plate contributing to a large race-tracking effect. The resin flowed around the periphery of the laminate (underneath the caul plate) prior to penetrating the laminate stack. This left an oval-shaped macro-void in the center of the laminate that was never fully impregnated. Images of the race-tracking effect during the infusion and the finished part are shown in Figure 3.14.

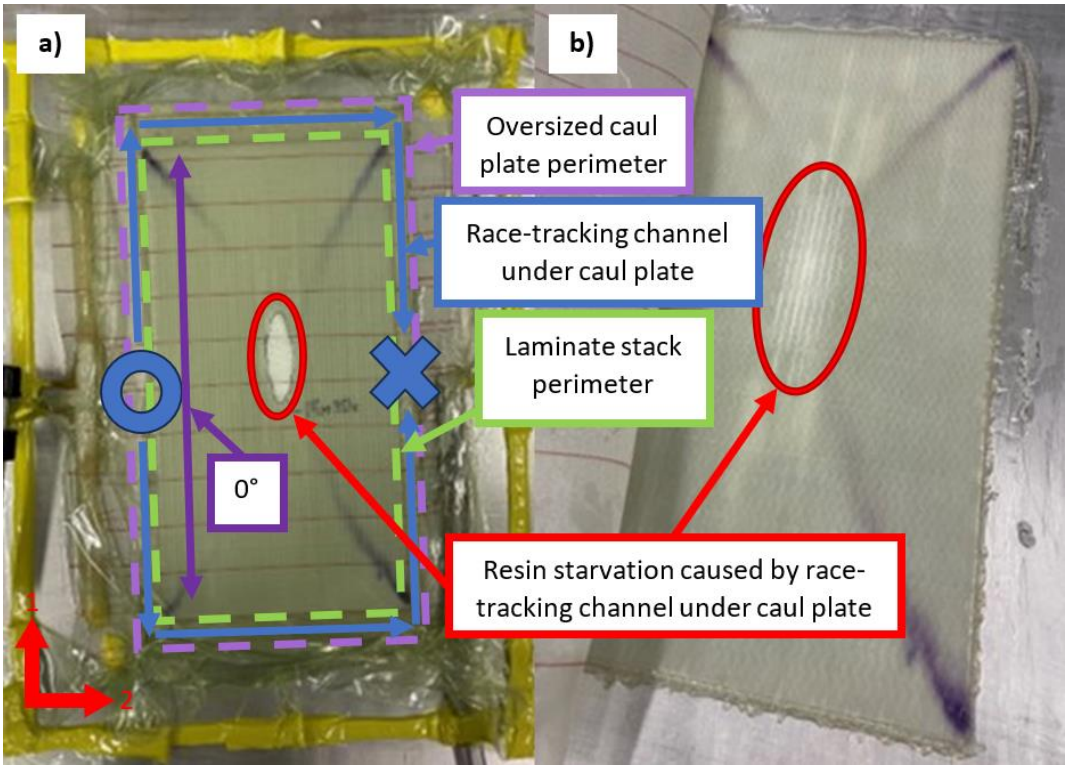


Figure 3.14: Oversized caul plate trial; (a) high permeability flow channel underneath caul plate flanges encouraged resin flow around laminate. Thus, the center of laminate was infused last, and (b) panel demonstrated resin starvation at the center.

A subsequent trial was conducted with an undersized caul plate relative to the laminate planform area to minimize the race-tracking effect. With a smaller caul plate, the resin could flow through the laminate although a race-tracking flow persisted along the edges of the caul plate. Nonetheless, the undersized caul plate prevented air pockets from being trapped within the center of the laminate. There was a clear transition in surface roughness between the region of the panel that was covered by the caul plate compared to the region that was uncovered. The surface of the uncovered area followed the contour of the longitudinal fabric tows, while the surface under the

caul plate was comparatively smooth. Figure 3.15 shows an image of the flow front where the race-tracking phenomenon is reduced compared to Figure 3.14, and an image of the laminate cross section demonstrating the change in surface roughness from the uncovered area to the covered area.

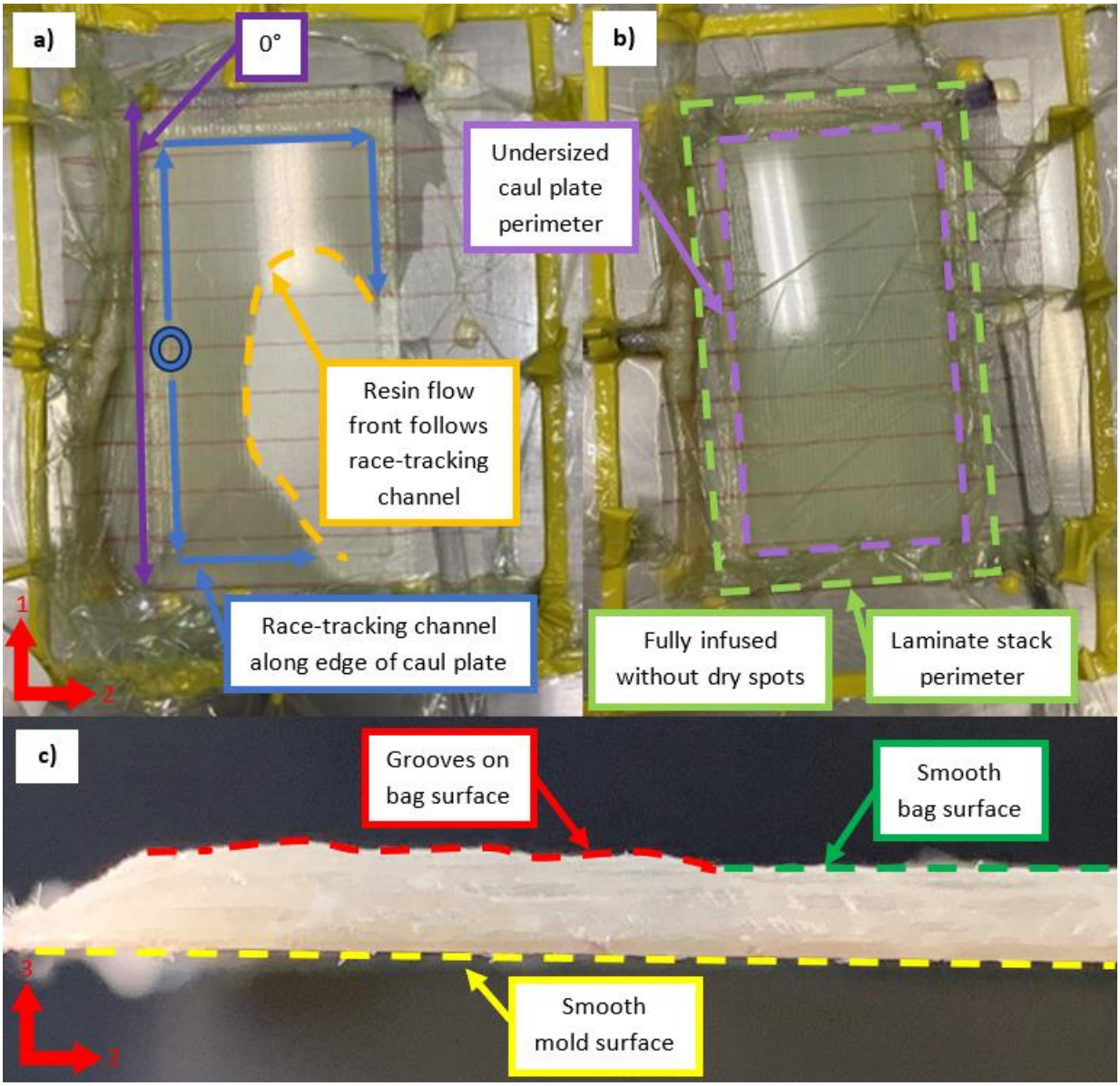


Figure 3.15: Undersized caul plate trial; (a) large degree of race-tracking due to flow channels along edges of caul plate, but the race-tracking effect is significantly reduced compared to the oversized caul plate trials, (b) reduction in race-tracking allowed full panel impregnation, and (c) comparison between regions of laminate that were uncovered (red) and covered (green) by caul plate, showing reduced propensity for groove formation along the UD-NCF tows on the vacuum bag surface.

Despite the caul plate demonstrating an improvement in the bag-side surface quality of the panel, the capital cost required to manufacture a suitable caul plate for a complex geometry such as a blade shell was prohibitive, and the caul plate solution was not adopted for future trials. With the requirement that the caul plate must be rigid, this would necessitate a large, machined mold to achieve the correct shape. While the expenditure for a caul plate would theoretically be cheaper than producing a separate mold half entirely, developing such a tool for experimental research and development was financially risky. Thus, it was concluded that a caul plate can be an effective tool for flat parts, but that the constraints of a turbine blade minimized the effectiveness of such a tool for these applications.

3.3.9. Summary of Optimized VARTM Setup

Section 3.3 has provided an overview of the iterative approach taken to improve the baseline VARTM setup outlined in Section 3.2, where the objective of the process optimization was to simultaneously improve part quality and repeatability. Table 3-3 presents a comparison between the baseline and optimized setups.

Table 3-3: Overview of adopted VARTM parameters for optimized setup compared to baseline setup.

Parameter	Baseline Setup	Optimized Setup	Advantages	Disadvantages
Fabric	Veiled Fabric	Non-veiled Fabric	Increased panel V_f due to reduced inter-laminar thickness	Increased areal weight might increase resistance to compaction
Distribution Mesh	Covered entirety of laminate	Covered inlet region of laminate without approaching edge	Improved part quality by limiting voids caused by transverse flow	Significantly increased processing times
Vacuum Bag	Did not incorporate pleats	Incorporated pleats	Significantly increased part quality by ensuring uniform compaction throughout laminate	Increased quantity of vacuum bag and sealant tape required for infusion trial

Resin Feed	Elevated funnel	Resin reservoir	Securely mounted to workstation; easier to use	More difficult to clean between trials
Inlet Setup	Point inlet	Line inlet	Improved flow uniformity that might reduce dry spot formation for more complex parts	Increased setup time
Flow Rate	Unrestricted flow (no clamp)	Partially restricted flow	Limited potential for void formation due to transverse flow	Increased processing times

Additional parameters were investigated with varying degrees of success, but not implemented in the final optimized solution. A summary of the additional iterative trials is given in Table 3-4.

Table 3-4: Summary of additional process optimization trials that were not adopted for final, optimized VARTM process.

Parameter	Results	Reason for rejection
Weak Vacuum Pump	Consistent resin starvation throughout part	VARTM process effectiveness requires efficient, strong vacuum
Degassing Chamber	Did not conclusively alleviate resin starvation issues	Panel quality was acceptable after process optimization without relying on degassed resin
Caul Plate	Significantly improved surface smoothness on vacuum bag side	Upscaling caul plate for blade shell production would require fabrication of curved mold at significant expense

The baseline VARTM setup produced panels that were susceptible to resin starvation, particularly towards the inlet (Figure 3.3), while the optimized setup was able to repeatably produce parts with minimal visible resin starvation on either the mold side or vacuum bag side. A panel produced with the optimized process is shown in Figure 3.16.

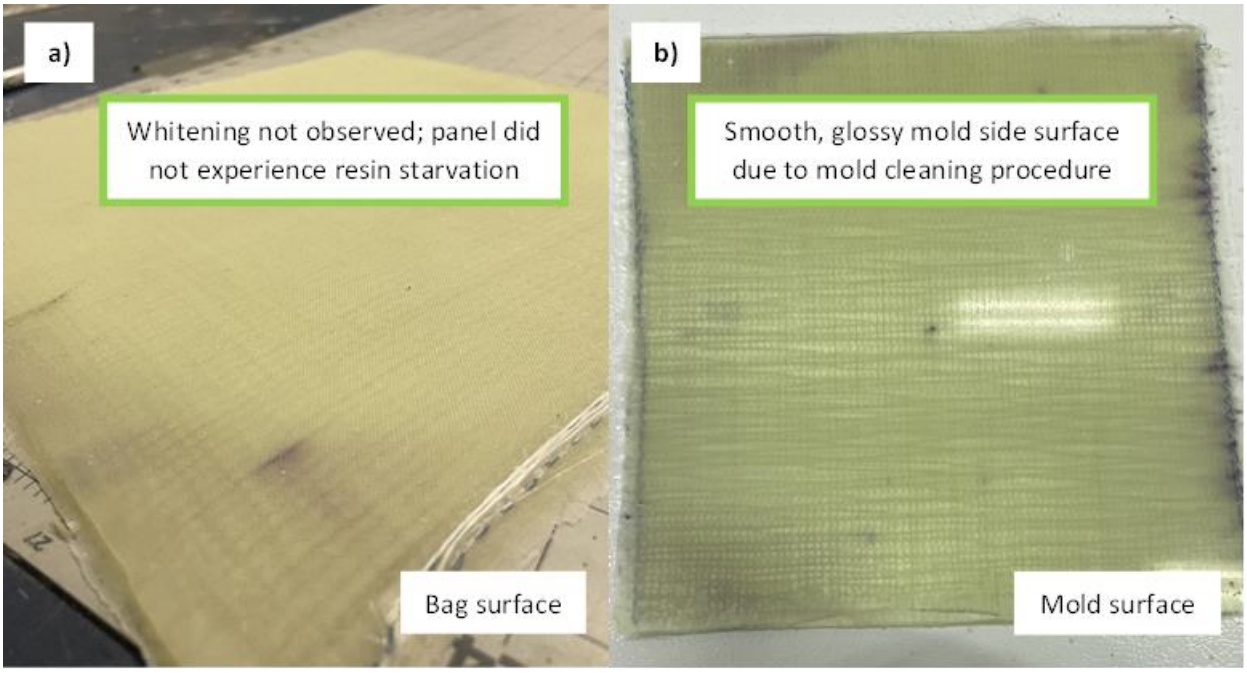


Figure 3.16: Thermoplastic E-glass UD-NCF composite panel produced with optimized VARTM process showing (a) bag and (b) mold surfaces.

A qualitative marker that may be used to assess the optimized VARTM process against literature results is a correlation of the void content distribution along the length of the panel. Considering that the inclusion of pleats in the vacuum bag yielded the greatest increase in part quality, the implication is that the poor laminate compaction caused by the pleat-less vacuum bag setup may have been exaggerated in the inlet region of the panel, potentially due to the increased flow velocity from the higher fluid pressure or the influence of the inlet line geometry on vacuum bag bridging. Investigating the void content of the optimized panels quantitatively would confirm whether the theoretical distribution matches the experimental production cycles [48].

3.4. High-Quality Panel Characterization

Optimization of the VARTM process required feedback from qualitative and quantitative assessments of the fabricated panels during process iterations. Rosso [21] used multiple techniques to characterize the same material system. Acid digestion was used to determine the V_f and V_c of samples from the fabricated panels, microscopic analysis was used to assess the microstructure of the material, and dynamic mechanical analysis (DMA) enabled identification of the glass transition temperature. Rosso experienced issues with acid digestion calculations yielding incorrect V_c values greater than 20%, which were attributed to incorrect measurements of the initial specimen volumes

and insufficient degradation the thermoplastic matrix phase. Subsequently, microscopic analysis was used to quantify void volume fraction. However, microscopic analysis of a 2D planar surface is generally not a reliable marker for quantifying the volume of 3D shapes throughout a microstructure. With these caveats in mind, the task of identifying reliable markers for panel quality was continued in this thesis.

3.4.1. Void Assessment

During VARTM process iterations, resin starved regions could be visually identified to provide a qualitative assessment whether process changes yielded tangible reductions in V_c. These qualitative assessments served as the basis for process iteration, and acid digestion was intended to be used as a final quantitative confirmation of the panel quality (the acid digestion procedure is described in Appendix A1). While acid digestion is a common approach in literature, nitric acid was incapable of completely decomposing the Elium® acrylic polymer, affecting the accuracy of the V_f calculations for the GFRP composite. All samples extracted from fabricated panels that underwent the acid digestion process exhibited a distinct hard plastic residue on the fibers. The problems with acid digestion necessitated microscopic analysis of the V_f for the composite; however, microscopic analysis would be unsuitable for V_c measurements. Nevertheless, a qualitative microscopic assessment of void content was performed. Figure 3.17 shows the size and location of a void within the microstructure of a high-quality panel produced with the veiled UD-NCF.

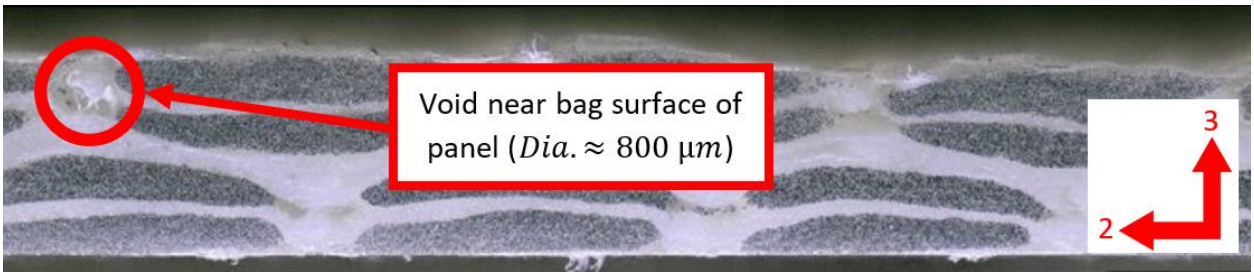


Figure 3.17: Qualitative microscopic assessment of void content within high-quality panel.

3.4.2. Fiber Volume Fraction Assessments via Microscope Analysis

Samples extracted from high-quality FRP panels produced with both the veiled and non-veiled UD-NCFs were investigated using a VHX-5000 opto-digital microscope (Keyence, Canada). Sample preparation for microscopic analysis of the FRP samples followed the procedure for cold mounting, grinding, and polishing outlined in Appendix A2. The polishing process used

a semi-auto polishing machine, creating a clear distinction between the fibers and matrix under a microscope at high magnification. The microscope software measuring tools were used to calculate the intra-tow fiber volume fraction, the volume fraction of the tows, and the total V_f of the FRP material samples.

Initial VARTM trials utilizing the custom veiled UD-NCF yielded V_f values around 42%, which was deemed to be low when compared to a previously reported study [52]. Due to the existence of the veil, the interlayer laminate thickness was notably larger and V_f lower when compared to the panels comprising the non-veiled Saertex UD-NCF. In practice, the increased thickness caused by the polymeric veil is negated if the veil dissolves into the resin during a high temperature curing cycle allowing greater compaction of the fabric layers [30]. However, in this study the veil did not dissolve because resin infusion and in-situ polymerization occurred under room temperature conditions. A study by García-Rodríguez et al. found that a polymeric veil that did not dissolve during processing increased the thickness of the ply interface and caused porosities in the resin-rich regions [30]. Thus, the melting temperature and architecture of the veil affected the laminate microstructure and impacted part performance. García-Rodríguez et al. observed that samples that included a veil with a melting temperature below the curing temperature of the resin (i.e, initiating veil degradation) experienced a 100% reduction in the damage area after a 14J impact test and a 28% increase in compression after impact (CAI) strength compared to samples where the veil had a higher melting temperature than the curing temperature (i.e, the veil did not degrade). The non-veiled UD-NCF comprised glass fiber roving with a high linear density and an overall higher aerial density when compared to the veiled UD-NCF, contributing to an increase of approximately 35% in FRP panel thickness for an identical ply stacking sequence of $[0_4]$. A summary of the volume fractions for both FRP samples are presented in Figure 3.18 and Table 3-5. The FRP samples comprising non-veiled UD-NCF exhibited an average V_f that was 8.2% greater. This result implies that the veil did not dissolve during processing and would not allow the fabric layers to sufficiently compact. The intra-tow fiber volume fraction of the veiled samples was 12% higher than the non-veiled samples, which may be attributed to polishing and the increased linear density of the non-veiled UD-NCF tows. The polishing scheme was optimized for the veiled microscope trials and exhibited less chipping of the fibers compared to the non-veiled samples (Figure 3.18). The effect of the veil was most clearly visible within the tow volume

fraction, where the non-veiled UD-NCF was 18.5% higher than the veiled fabric, implying improved inter-laminar compaction due to the removal of the veil.

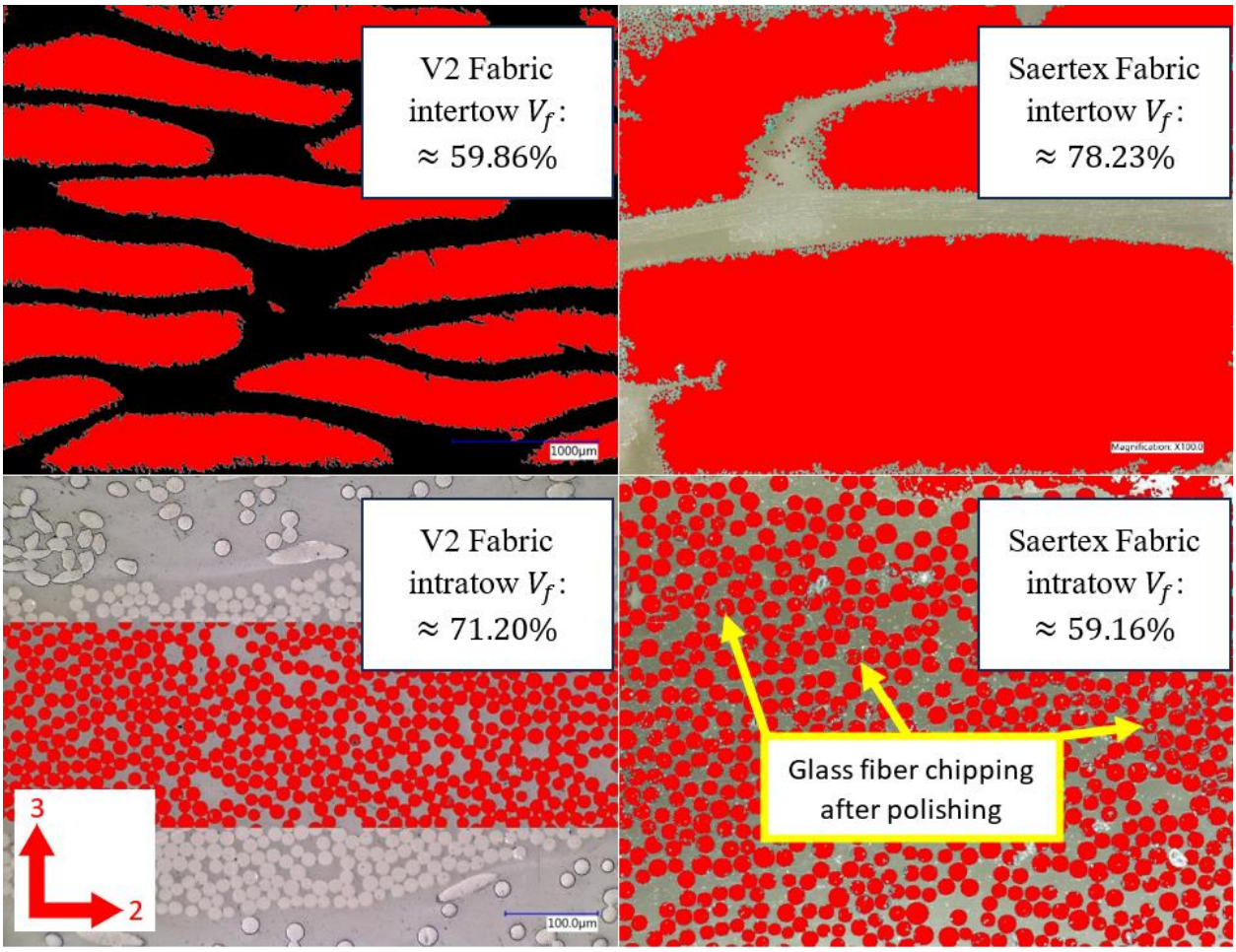


Figure 3.18: Cross-sectional images used to assess tow volume fraction for (a) veiled and (b) non-veiled UD-NCFs, and intra-tow fiber volume fraction for (c) veiled and (d) non-veiled UD-NCFs.

Table 3-5: Comparison of volume fractions for indicated FRP samples.

	FRP samples with veiled UD-NCF	FRP samples with non-veiled UD-NCF
Thickness (mm)	1.89 (±0.0042)	2.91 (±0.025)
Tow volume fraction (%)	59.86 (±2.9)	78.23 (±2.1)
Intra-tow fiber volume fraction (%)	71.20 (±1.6)	59.16
V_f (%)	42.50 (±2.1)	46.28 (±1.2)

Chapter 4: Adhesive Joint Testing

Fracture tests were performed to assess the Mode I and Mode II response of non-veiled UD-NCF composite substrates bonded with a methacrylate adhesive. A key objective of these tests was to establish a suitable adhesive joint for a micro-generating wind turbine blade designed to operate in extreme environments. Thus, double-cantilever beam (DCB) and end-notched flexural (ENF) tests were performed under room temperature (RT) (25°C) and low temperature (LT) (-40°C) conditions. For each test case, three distinct specimen adhesive bond-line thicknesses were considered. The test specimen fracture surfaces were then analyzed to assess the associated failure modes. The RT DCB tests were simulated using the commercial finite element software ABAQUS and a cohesive zone model (CZM) to calibrate the calibrate the bilinear TSL values. Due to complications with the recording of the elastic stiffness values and a highly brittle fracture response for the LT DCB specimens, and issues with tracking the crack tip for all ENF tests, these trials were not simulated in ABAQUS.

4.1. Specimen Preparation and Test Setup

The non-veiled E-glass UD-NCF/Elium® composite panels processed in Chapter 3 were used to extract the substrates for the adhesively joined specimens. The mechanical properties of the FRP material were reported by Shi [44] (Table 4-1) and required in this study for fracture test data reduction schemes. The MMA adhesive FIT3045 (Bostik, France) was used in this study, which is composed of 40-80% methyl methacrylate monomer, enabling a chemical bond with the Elium® FRP substrate [111]. The FIT3045 adhesive also contained smaller quantities of quartz, butyl methacrylate, and isocyanate compounds.

Table 4-1: Non-veiled E-glass UD-NCF/Elium® panel properties reported by Shi [44]. *Panel properties were required for data reduction schemes during adhesive characterization.*

Property		Mean Value (±STV)
E_1 (GPa)	Longitudinal Young's modulus	28.9 (±1.7)
E_2 (GPa)	Transverse Young's modulus	6.5 (±0.5)
ν_{12}	Major in-plane Poisson's ratio	0.28 (±0.03)
G_{12} (GPa)	In-plane shear modulus	1.9 (±0.3)
X_t (MPa)	Longitudinal tensile strength	570.5 (±18.1)
Y_t (MPa)	Transverse tensile strength	36.5 (±1.2)

4.1.1. Specimen Preparation

The specimen substrates were cut from fabricated FRP panels using an abrasive waterjet cutting machine. The dimensions of the DCB substrates were 25.4 mm × 140 mm following a study by Dehaghani [63], while ENF substrate dimensions were 25.4 mm × 75 mm as per a study by Ribeiro et al. [82]. Note, the length of the substrates was limited by the internal dimensions of the climate chamber used for LT testing. The substrates retained an $[0]_4$ stacking sequence with the longitudinal fiber direction oriented along the length of the substrates. The thickness of each substrate was measured with a Mitutoyo micrometer with an average value of 2.91 (±0.025) mm.

Prior to bonding the substrates, the surfaces were treated based on guidance from the adhesive supplier. For the mold side of the panel, an abrasion procedure with 180 grit sandpaper was performed, followed by degreasing with isopropanol. For the vacuum bag side of the panel, degreasing with isopropanol without abrasion was sufficient due to the imprint from the peel ply during panel processing. Prior to adhesive bonding, a Surtronic 25 profilometer (Taylor Hobson, England) was used to measure the surface roughness of the abraded mold side of the specimen at 3 locations. The average surface roughness (R_A) increased from 0.28μm to 0.76μm after abrasion.

Each specimen used a custom fixture setup [63] to bond the peel ply side of one substrate to the mold side of another with the MMA adhesive at ambient conditions of 25°C and 30% humidity, and the adhesive was allowed to polymerize for at least 15 hours. Shims were used to define the pre-crack and control the adhesive bond-line thickness. Three different shim thicknesses that satisfied the adhesive supplier recommended bond-line specifications (between 0.2mm and

1.0mm; optimum performance at 0.8mm) were used for DCB (0.25mm, 0.635mm, 0.8mm) and ENF (0.3mm, 0.475mm, 0.6mm) tests. For the DCB specimens the shims were glued to the substrates; however, this led to an artificial initial stiffness response during the tests (Section 4.2.1). Thus, when bonding the ENF specimens the shims were taped to the substrates.

After adhesive polymerization was completed, the excess adhesive was removed from the edges of the specimens using a chisel to observe the bond-line thicknesses. The bond-line thicknesses and pre-crack lengths were measured using a VHX 5000 opto-digital microscope (Keyence, Canada). An image of the edge of a DCB specimen captured with the microscope with a measurement of the bond line thickness is shown in Figure 4.1.

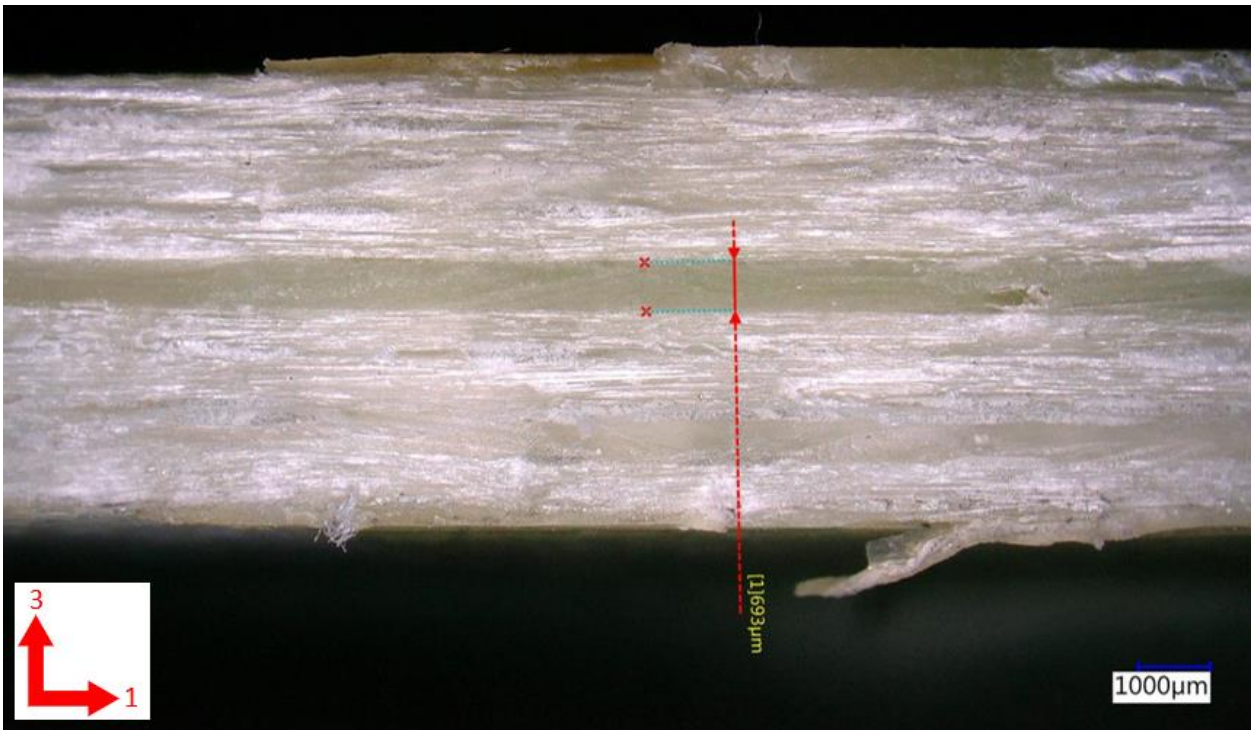


Figure 4.1: Microscopic bond-line thickness measurement for bonded specimen.

The dimensions of the DCB and ENF specimens are presented in Table 4-2 and Table 4-3, with reference to the dimensions outlined in Figure 2.15.

Table 4-2: DCB test specimen dimensions (corresponding to Figure 2.15).

Shim thickness (mm)	Length L (mm)	Width B (mm)	Bond-line Thickness t_A (mm ±STV)	Pre-Crack Shim length a_0 (mm ±STV)	Total Sample Thickness $2h$ (mm ±STV)	Average Surface Roughness (μm ±STV)
0.25	140	25	0.33±0.049	45.52 ±0.44	6.01 ±0.088	0.76 ±0.047
0.64			0.72 ±0.12	45.41 ±0.47	6.35 ±0.065	
0.8			0.81 ±0.073	45.89 ±0.42	6.51 ±0.062	

Table 4-3: ENF test specimen dimensions (corresponding to Figure 2.15).

Shim thickness (mm)	Length L (mm)	Width B (mm)	Bond-line Thickness t_A (mm ±STV)	Pre-Crack Shim length a_0 (mm ±STV)	Total Sample Thickness $2h$ (mm ±STV)	Average Surface Roughness (μm ±STV)
0.25	75	25	0.30 ±0.046	51.41 ±0.26	6.15 ±0.18	0.76 ±0.047
0.48			0.61 ±0.027	52.68 ±0.55	6.43 ±0.088	
0.68			0.72 ±0.069	52.46 ±0.36	6.48 ±0.070	

The grips of the test frame used in this study necessitated the use of piano hinges bonded onto the DCB specimens to enable the application of a tensile load to drive crack propagation as per ASTM standard D5528 [78]. 304 stainless steel piano hinges (Spaenaur, Canada) with 2.29 mm (0.090 in) thick arms and a 4.75 mm (0.187 in) diameter hinge pin (product number 098-805) were used to ensure that peeling of the hinges from the substrates was mitigated. The surfaces of the substrates were sand blasted (60-grit silicon carbide at 25 psi) and cleaned with isopropanol prior to bonding with the piano hinges. The hinges were bonded to the substrates using Loctite 480 (Henkel, USA) and allowed to cure for 24-hours while clamped to achieve full strength.

4.1.2. Experimental Setup

An MTS 810 servo-hydraulic test frame with a 50kN capacity load cell (signal variability ±100N) was used for all tests. Mechanical wedge grips were used for the DCB tests (Figure 4.2), while an adjustable three-point bending test fixture with a span of 150 mm was used for the ENF

tests (Figure 4.3). Note, a sliding alignment bracket was used to position the ENF specimens parallel with the edge of the fixture, while a second bracket was placed at a 1-inch offset to prevent the specimens from slipping during the tests. All tests were performed in displacement control with a constant displacement rate of 0.1 mm/s.

The data reduction scheme from the ASTM standards required crack tip monitoring to compute the SERR. A Nikon DSLR camera with a Sigma EX 180mm lens was mounted on a tripod stand and focused on the adhesive layer at the edge of the test specimen immediately past the end of the initial crack tip to track the relative displacement of discrete markers that were evenly spaced at 2.5 mm increments. Video of the adhesive deformation was captured in 1080p at 30FPS. Data was captured at 2Hz for the DCB trials, which was sufficient for the RT tests due to the high ductility of the adhesive. Due to the brittleness of the material response at LT, all LT tests were sampled at 30Hz. The load-displacement data was synchronized with the DSLR camera footage during post-processing.



Figure 4.2: Test frame grip fixture with the DCB specimen mounted. The hinge was aligned within the grips prior to tightening to avoid specimen damage.

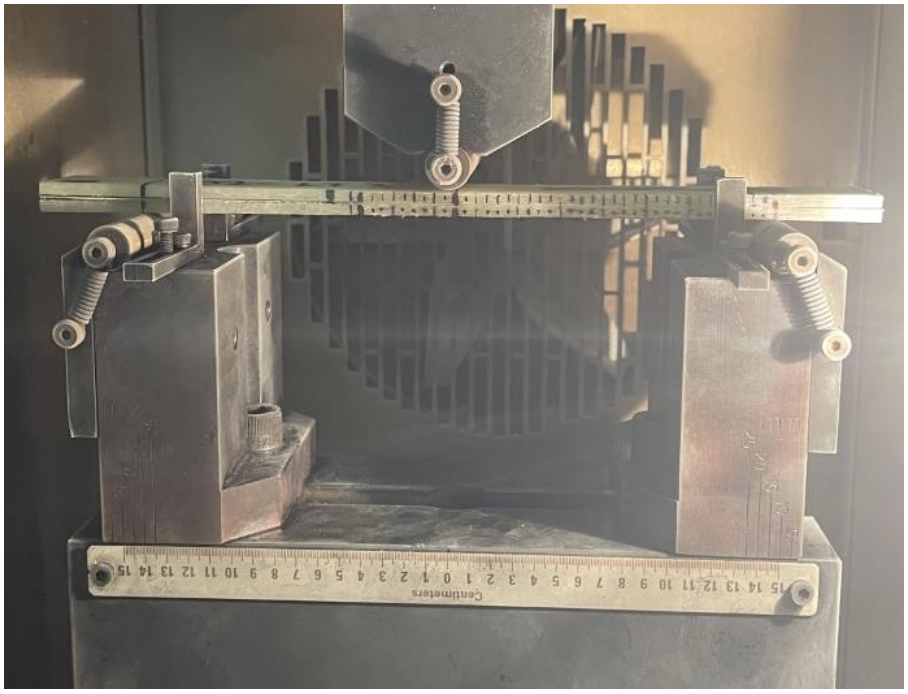


Figure 4.3: ENF specimen mounted on the 3-Point Bend fixture. L-brackets constrained the out-of-plane slippage, and the specimens were aligned such that the midspan coincided with the central loading pin.

4.1.3. Climate Chamber Setup – Low Temperature

The MTS 810 test frame was equipped with an Instron 3119-609 climate chamber to perform the LT tests. The chamber was cooled using a NI LC230-22 LN2 canister from Praxair Canada, reaching the set temperature of -40°C in 10 minutes. Once the set chamber temperature was attained, the specimens were allowed to reach thermal equilibrium during a 5-minute interval. The test frame was set to load control during the temperature cooldown to allow for unrestricted contraction under zero load, thus avoiding premature specimen damage. The climate chamber comprised a heated observation window that prevented frosting during LT tests, which enabled excellent image resolution (Figure 4.4).



Figure 4.4: Test footage was captured via DSLR cameras adjusted on a tripod mount. The heated climate chamber window ensured a good quality image.

4.1.4. Mode-I SERR Data Reduction Scheme

The Modified Beam Theory (MBT) method is a commonly employed data reduction scheme for computing G_I as indicated in the standard ASTM D5522 [78]. Gálvez et al. demonstrated that the MBT model can be used reliably in conjunction with DSLR footage for a ductile thermoplastic (polyurethane) adhesive [112]. The calculation of G_I via the MBT method is given by:

$$G_I = \frac{3P\delta}{2B(a+|\Delta|)}, \quad (8)$$

where P is the load, δ is the load point displacement, B is the specimen width, a is the crack length, and Δ is a compliance correction factor. The Δ parameter was computed from the cubed root of the beam compliance (Figure 4.5) [63]. The crack length a was determined using DSLR video footage, and post-processed using the *Tracker* open-source software tool [113]. The software

followed discrete marker points on each of the substrates to determine the precise moment when the markers began vertically separating from each other. A graphical explanation for this solution is provided by Dehaghani and shown in Figure 4.6 [63].

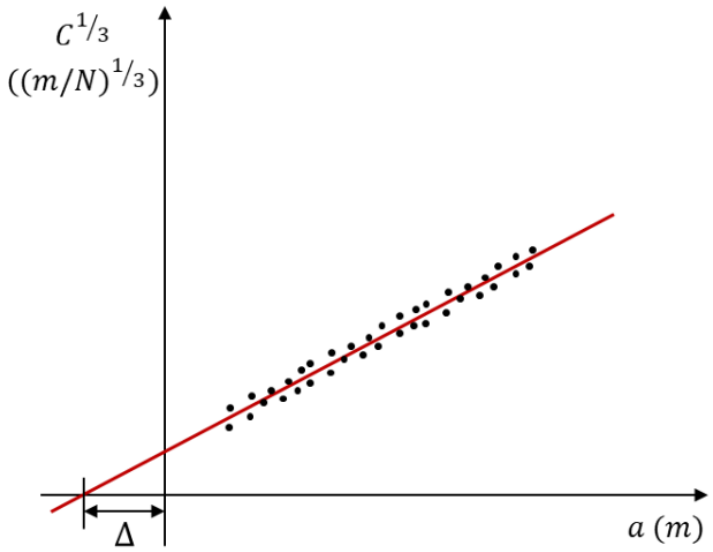


Figure 4.5: Schematic showing calculation of Δ calibration parameter for the Modified Beam Theory [80].

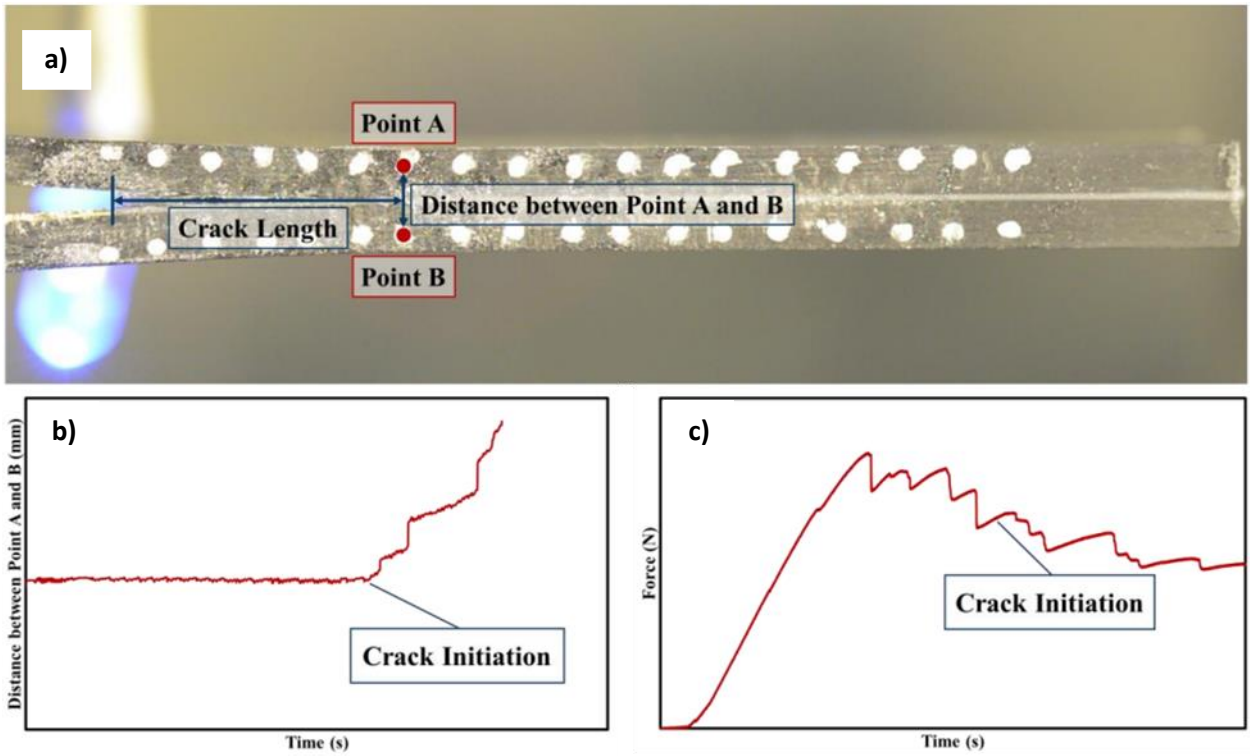


Figure 4.6: Crack tip following algorithm demonstration; (a) image taken from Dehaghani thesis showing DCB samples with markings for DSLR analysis, (b) when Point B begins to separate from Point A, this implies that crack tip is located at Point B (for fracture toughness analysis), and (c) location of Point B crack tip within load-displacement curve [63].

The G_I value was measured at discrete 2.5 mm increments to determine the fracture response as the crack opened. An image from the *Tracker* software during crack tip monitoring is shown in Figure 4.7, where two separate frames monitoring the same discrete crack tip location are shown. The top image captured a frame prior to the crack tip reaching the discrete market, while the bottom image captured a frame after the crack tip had passed the same point. This point is highlighted in Figure 4.7 with a purple reticle that served as the coordinate system in the software. The corresponding point on the lower substrate was continuously tracked using the red dots shown in Figure 4.7. There is a clear ductile whitening that developed in the adhesive layer as it began to deform, and the onset of whitening occurred at the same moment that the software identified the relative movement of the corresponding markers. The whitening region constituted the Fracture Process Zone (FPZ). Once the crack tip locations were synchronized with the load-displacement curve, the MBT method was used to determine G_I at each discrete point. By averaging the discrete G_I values, G_{IC} for the adhesive system at a given bond-line thickness could be computed.

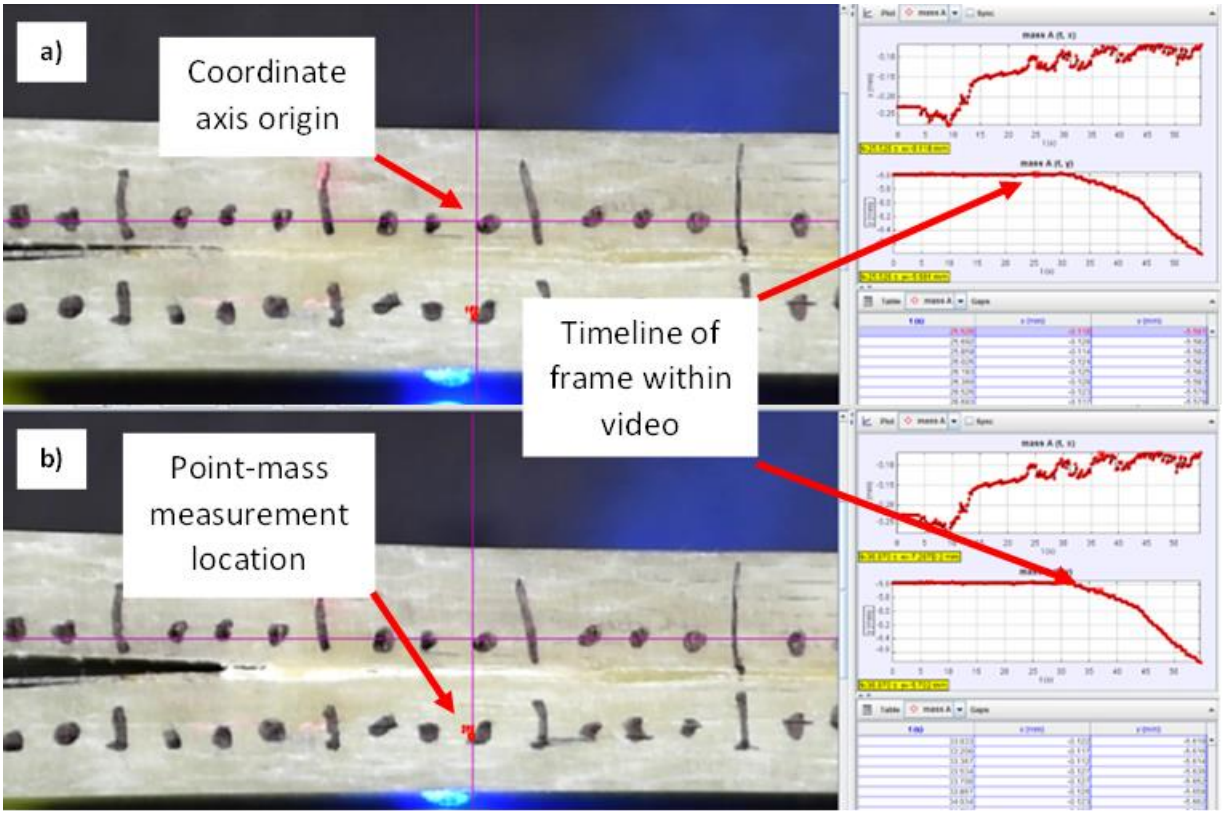


Figure 4.7: Progression of ductile process zone demonstrating significant whitening and void formation; (a) discrete crack marking point prior to crack tip reaching the marker, and (b) same discrete marking point when crack tip reaches marker.

4.1.5. Mode-II SERR Data Reduction Scheme

While crack tip monitoring is feasible for DCB tests and enables calculation of the Mode-I G_{IC}, there has not been a widely accepted crack tip monitoring solution for Mode II ENF tests. While the separation of the DCB specimen substrates yielded a clear FPZ in this study, the crack tip was not clearly discernible during the ENF tests (Figure 4.8). Additionally, the bending of the substrates during ENF testing did not allow the *Tracker* software to be used effectively, since the corresponding marker points slid in multiple axes relative to each other. Data reduction schemes exist in the literature – such as the Compliance-Based Beam Method (CBBM) – that utilize an artificial (or effective) crack tip computation, where the material properties of the substrate are used to determine G_{IIC} instead of crack tip monitoring [80]. However, this method was not considered in this thesis.

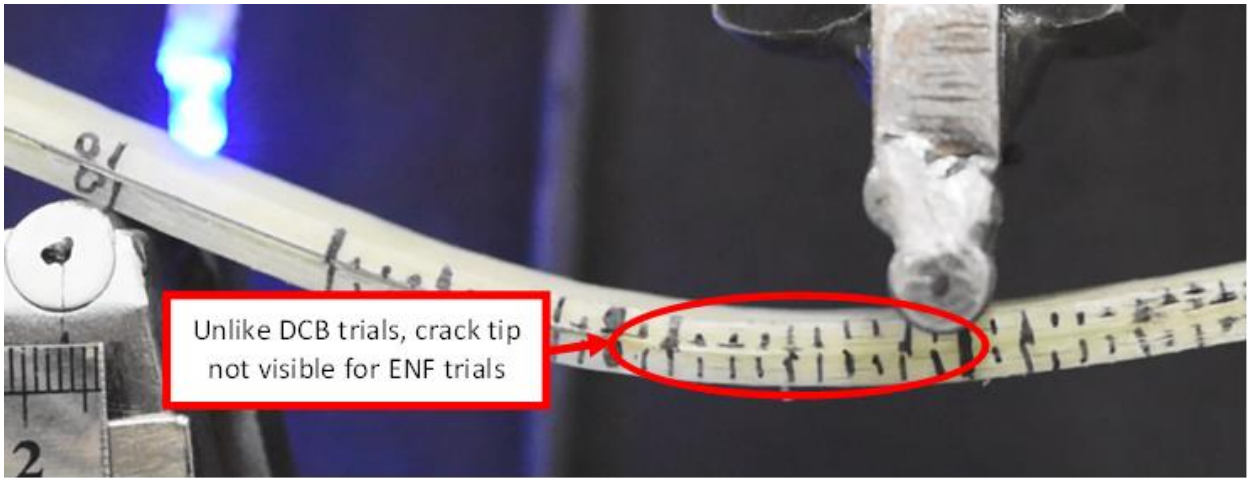


Figure 4.8: Image of ENF specimen captured in-situ during test, revealing that the crack tip was not clearly visible.

To counter the problems with DSLR crack tip monitoring, literature studies have investigated the validity of crack tip monitoring algorithms using DIC methods [81]. Ferrarese developed a crack tip algorithm that could parse data from VIC 2D-6 using MATLAB to identify the crack tip during Mode I DCB testing [81]. The MATLAB script iteratively parsed each frame from VIC 2D-6 and compared the *SIGMA* parameter from adjacent frames. The *SIGMA* parameter tracks relative variance between frames. This approach was adopted for the ENF trials to attempt to determine G_{IIC}. The primary objective of the trials was to investigate if the *SIGMA* parameter could accurately discern variance between adjacent frames and allow future work to adopt the algorithm from Ferrarese for ENF tests. Thus, speckle patterns were applied to a sub-set of RT ENF specimens and observed by the DSLR camera.

The ENF tests were parsed through VIC 2D-6 using *Subset* and *Step* values recommended by Ferrarese, and a strain field plot was generated for the duration of the video [81]. Results from the DIC analysis showed that the strain fields and damage gradient in the adhesive layer could be identified throughout the specimen. The strain field representation is purely visual and shows that the DIC software could identify the speckle pattern throughout the test. The strain field is not intended as a marker for the fracture toughness since strain is dependent on specimen geometry and G_{IIC} calculations do not have a condition that relates the strain of the adhesive layer to the crack length. An image of the strain field in the ENF specimen is shown in Figure 4.9.

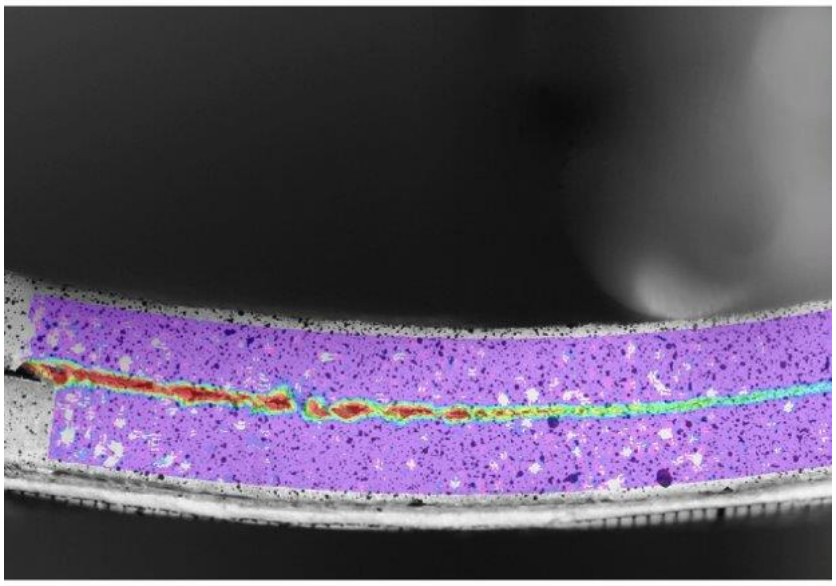


Figure 4.9: Strain field monitoring of ENF samples using VIC 2D-6 DIC software.

The *SIGMA* parameter for the ENF trials was also recorded. However, results indicate that the *SIGMA* parameter was calibrated as an absolute marker relative to the initial frame instead of a relative marker between adjacent frames [81]. Thus, further work must be done to troubleshoot the software and tune the *SUBSET* and *STEP* parameters to the ENF test geometry, including further optimization of the speckle pattern resolution. The current results suggest that there is merit to using the DIC method to assess the crack tip location for ENF tests; however, development of an appropriate script and optimizing the test setup was outside the scope of this thesis.

4.2. DCB and ENF Test Results

4.2.1. DCB Test Results

The load-displacement curves for the RT and LT DCB tests are shown in Figure 4.10. The methacrylate adhesive performance was dependent on the ambient temperature and bond-line thickness. RT load-displacement curves showed that as the adhesive layer thickness increased, higher loads could be sustained at a given displacement value. It should be noted that the load-displacement responses within the elastic range were slightly inaccurate for all RT and LT Mode I tests. This inaccuracy is due to the fact that the metal shims used to control the thickness of the adhesive were glued to the substrate. Thus, the stiffness of the shims influenced the elastic response prior to the point when the shims debonded from the substrate (represented by the non-linearity in

the elastic region of the plots shown in Figure 4.10). This was rectified for the ENF trials by taping the shims to the substrate.

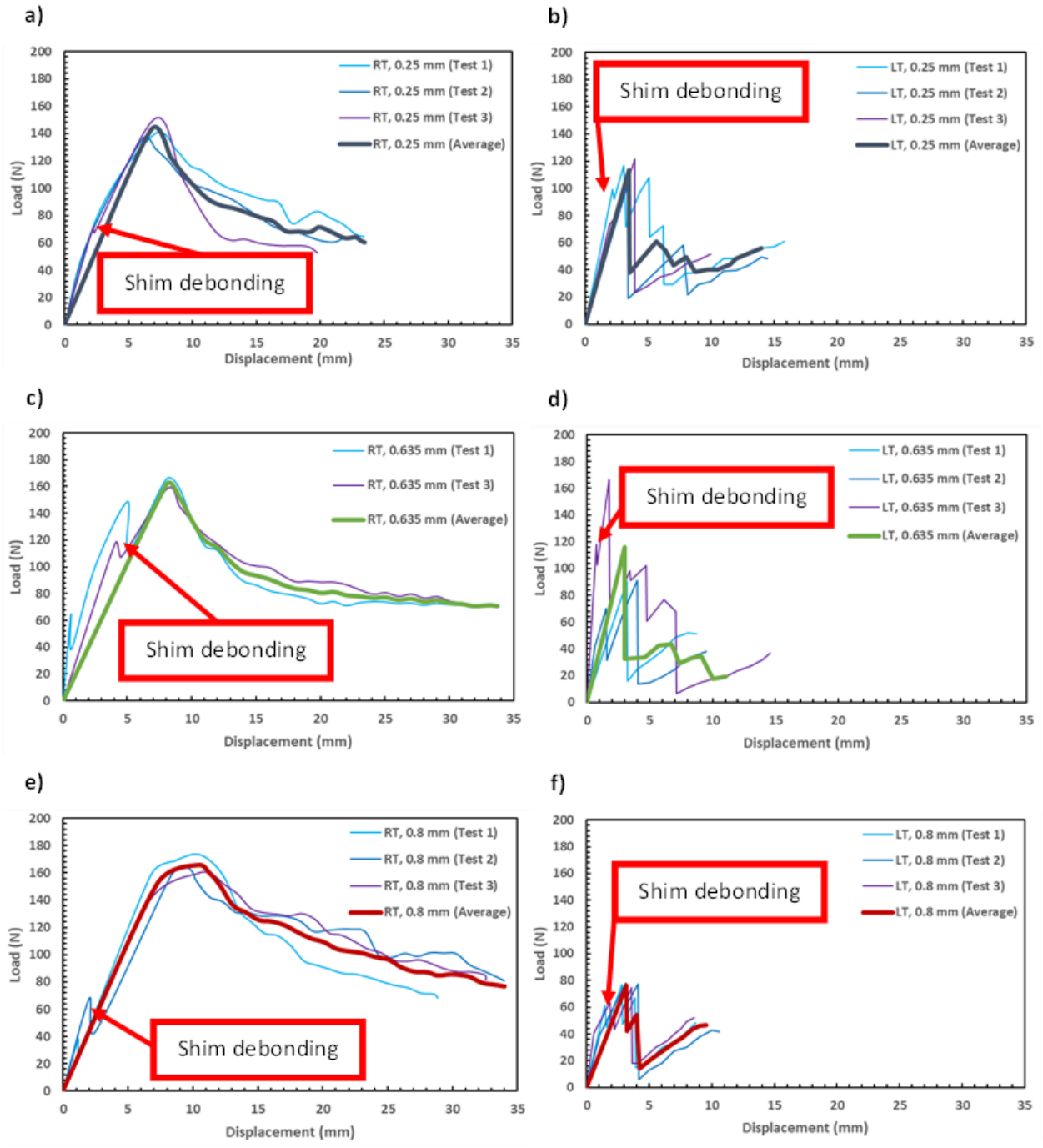


Figure 4.10: Load-Displacement curves of RT and LT DCB specimens with varying bond-line thicknesses.

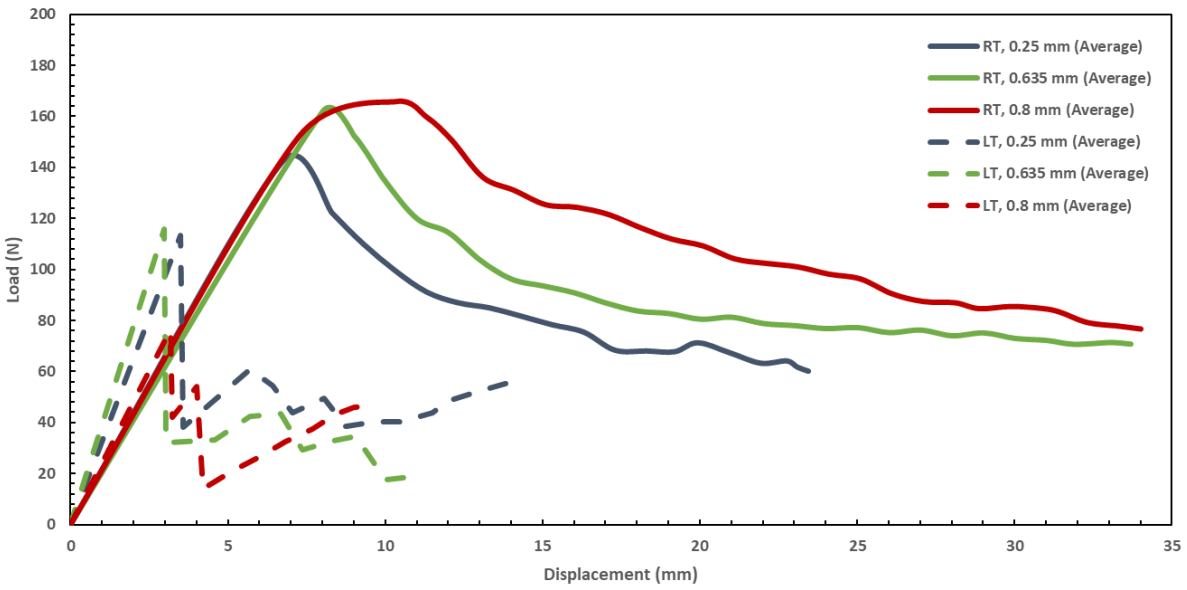


Figure 4.11: Overlay of average Load-Displacement curves for DCB tests at RT and LT.

The average load-displacement curves are combined in Figure 4.11, demonstrating the effect of bond-line thickness and temperature on the response. According to the adhesive supplier, peak performance is achieved when the bond-line thickness was between 0.2 and 1.0mm, with theoretical peak performance at a bond-line thickness of 0.8mm. The expected adhesive performance as a function of the bond-line thickness was confirmed by the load-displacement curves at RT. As Figure 4.11 demonstrates, at a target bond-line thickness of 0.25mm, a 60N load was sustained at 24mm of displacement before failure. Comparatively, at a target bond-line thickness of 0.6mm, a 70N load was sustained at 34mm of displacement before failure, and at a target bond-line thickness of 0.8mm, an 80N load was sustained at 34mm of displacement before failure. The MBT method was applied to the RT samples to determine the post-peak SERR response. The G_{IC} values for the RT DCB curves are shown in Table 4-4. Thus, G_{IC} for the RT DCB specimens increased by 45% over the range of bond line thicknesses considered.

Table 4-4: G_{IC} calculations using MBT method for RT-DCB specimens.

Bond-line Thickness (mm)	G_{IC} (N/mm)
0.2	0.892
0.635	1.231
0.8	1.632

The bond-line thickness did not clearly influence the LT DCB load-displacement results. The LT DCB specimens exhibited reduced load and displacement at failure when compared to the RT DCB specimens with a brittle failure response and stick-slip behavior as the crack propagated in an unstable manner, which is analogous to the results reported by Jia et al. [87] for a polyurethane adhesive. Unstable crack propagation prevented the MBT method from being used to determine the post-peak G_{IC} response of the adhesive. The LT DCB specimens exhibit an increase in the initial elastic stiffness compared to the RT DCB specimens. However, the inconsistency with the elastic stiffness performance of the specimens caused by the shim debonding during loading would have affected these results.

4.2.2. ENF Test Results

The load-displacement curves for the RT and LT ENF tests are shown in Figure 4.12, with the average curves combined in Figure 4.13. For the RT tests, the results were truncated to 25mm of displacement, i.e., when the crack tip did not surpass the central loading pin. It should be noted that one of the RT samples with the 0.635mm thick shim experienced a sudden change in elastic stiffness and a premature failure due to misalignment during the bonding process. The effect of bond-line thickness was observed at RT, where specimens with a 0.635mm bond-line thickness exhibited a higher peak load than the samples with thinner bond lines; however, the initial stiffness was consistent for all bond line thicknesses. The LT samples all abruptly failed in a brittle manner at approximately 800N, irrespective of the bond-line thickness and exhibited a consistent initial stiffness. Similar to the Mode I tests, the ENF specimens sustained a higher load at RT compared to LT. The elastic stiffness of the samples was also higher at LT than RT (Figure 4.13).

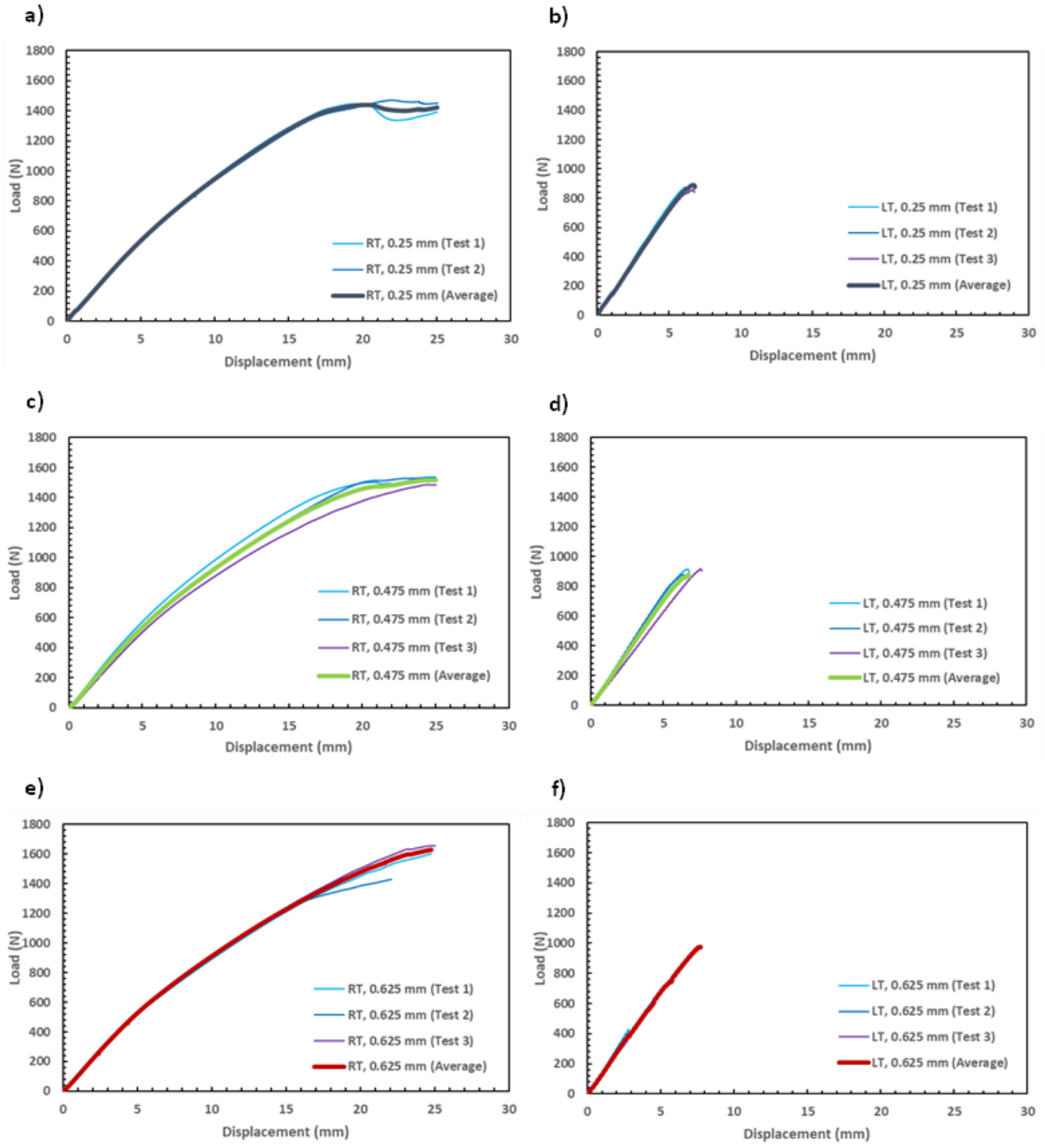


Figure 4.12: Load-Displacement curves of RT and LT ENF specimens with varying bond-line thicknesses.

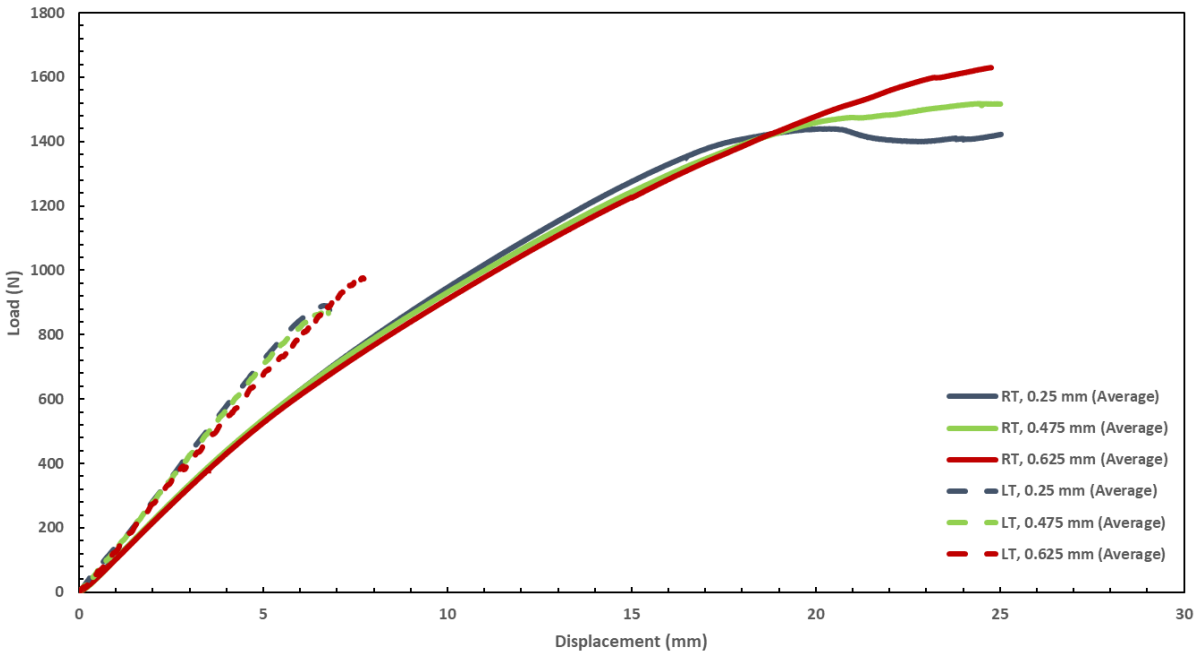


Figure 4.13: Overlay of average Load-Displacement curves for ENF tests at RT and LT.

4.2.3. Comparative Epoxy Adhesive DCB Tests

Additional DCB specimens were prepared with the glass fiber/thermoplastic substrates comprising the veiled UD-NCF and bonded using 3M 07333 toughened epoxy adhesive. The aim of these tests was to assess the failure mode of the toughened epoxy adhesive and the MMA adhesive. The surface treatment for the substrates was consistent with that described in Section 4.1.1. However, the epoxy adhesive specimens incorporated a loading block and pin instead of a piano hinge.

The epoxy adhesive trials clearly demonstrated material incompatibility between the adhesive and composite systems. Each specimen experienced interfacial failure between the composite laminate and the adhesive at room temperature. Certain specimens even experienced debonding from both substrates simultaneously. The simultaneous debonding of the adhesive layer from both substrates was captured by the DSLR camera and demonstrated the extent of the interfacial incompatibility, as shown in Figure 4.14 below.

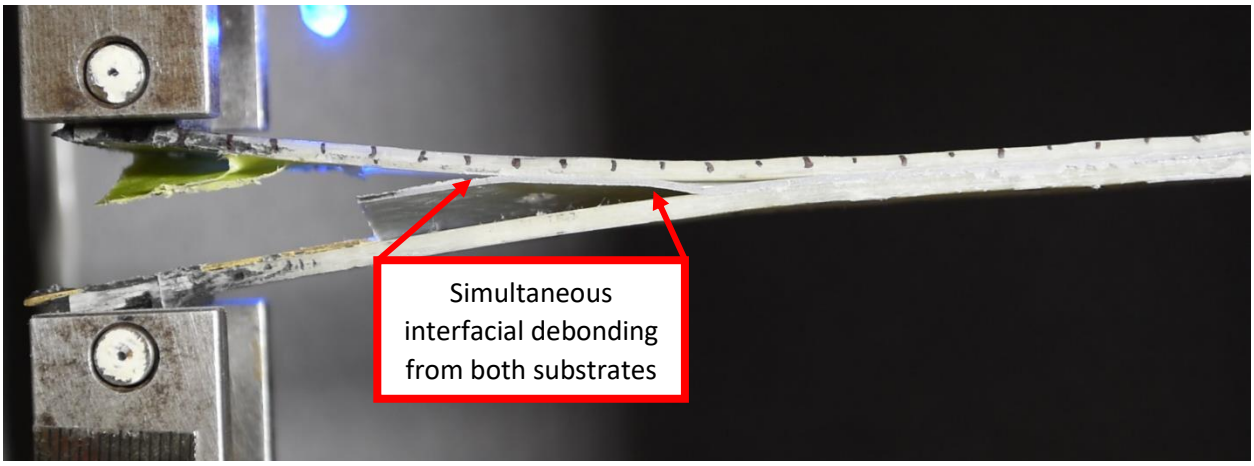


Figure 4.14: Simultaneous interfacial failure between both thermoplastic FRP substrates and epoxy adhesive during quasi-static DCB test.

Figure 4.15 shows the fracture surface of the epoxy adhesive samples after the interfacial debonding. The top face contained minimal epoxy residue and the composite surface remained intact. Thus, the low surface polarity of the acrylic-composite was incapable of forming a strong bond with the low diffusivity epoxy adhesive.

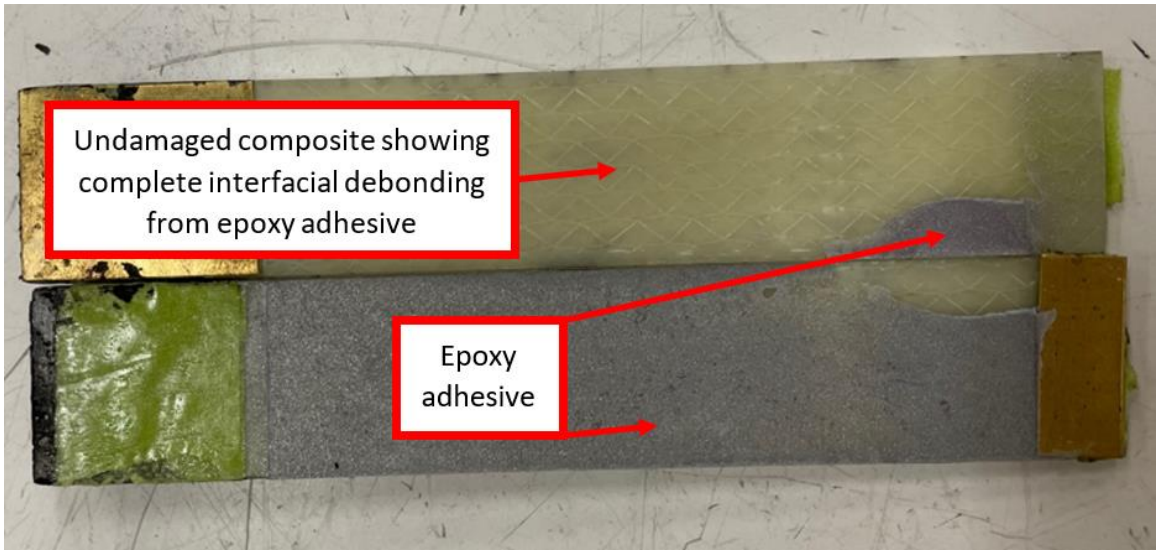


Figure 4.15: Interfacial failure between epoxy adhesive and thermoplastic FRP substrate.

The DCB test results with an epoxy adhesive confirmed observations from the literature that an abrasion and degreasing surface treatment method is insufficient for the joining of thermoplastic FRP substrates with an epoxy adhesive. Since thermoplastics have greater plastic deformation than thermosets, their surfaces do not become very chemically reactive after mechanical surface treatments [63], [66]. Thus, most studies into thermoplastic adhesive bonding

recommend more intensive surface treatments including corona treatment, plasma treatment, flame treatment, or chemical treatment methods [80]. For a medium-production scale, these advanced surface treatments would not be feasible.

4.3. Fracture Surface Analysis

4.3.1. RT DCB Specimens

Fractography of the RT DCB specimens further demonstrated that the adhesive failed in a highly ductile, cohesive manner with a large FPZ. The whitened fracture surface caused by the FPZ was broadly uniform throughout the adhesive layer (Figure 4.16).

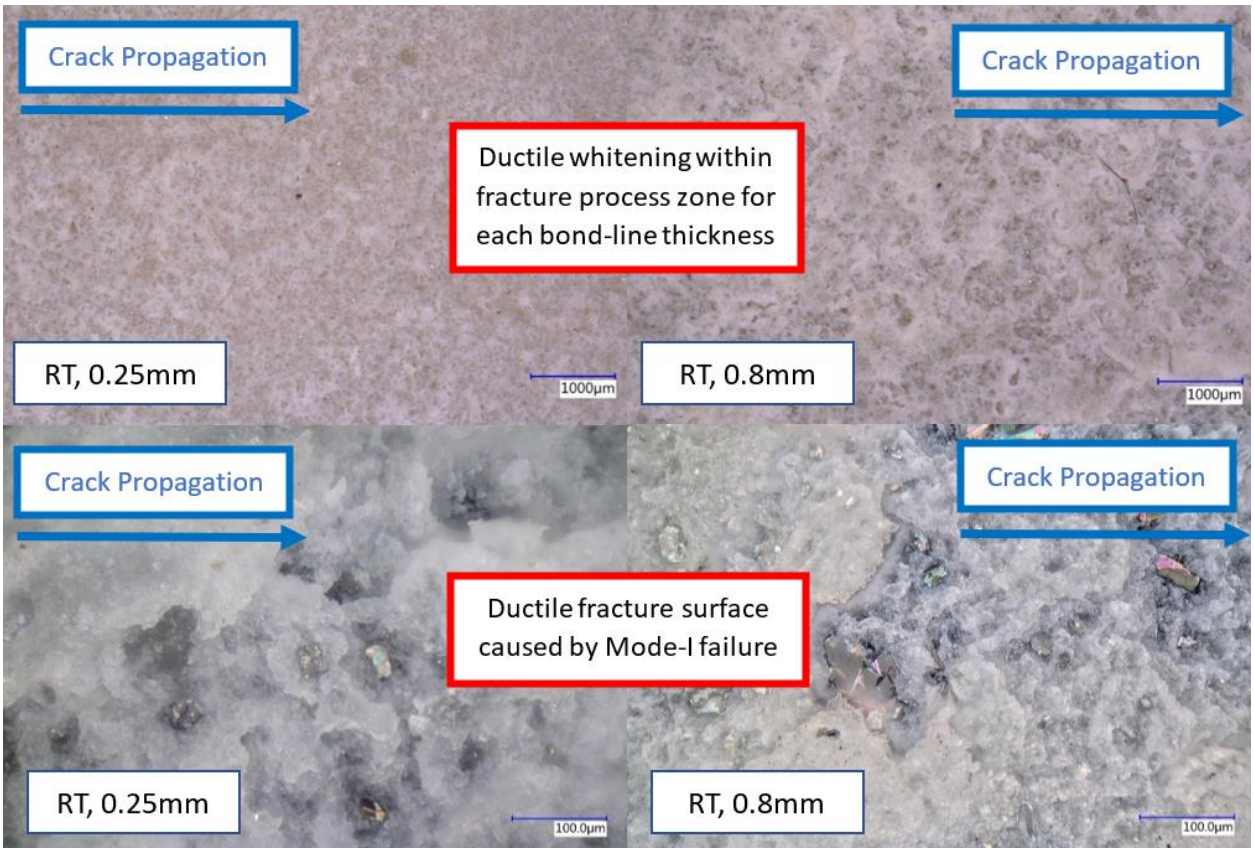


Figure 4.16: Ductile fracture surface of RT DCB specimens. Low magnification images of (a) 0.25 mm, and (b) 0.8 mm bond-line thickness specimens shows whitened FPZ, while high magnification images (c), (d) show consistent formulations for both bond-line thicknesses.

4.3.2. LT DCB Specimens

The fractured surfaces of the LT DCB specimens are visually distinct from the RT samples. Unlike the whitened, ductile fracture surface, the LT samples were smooth in appearance. Distinct, wave-like crack fronts that oscillated between substrates were observed for certain specimens.

These oscillatory fracture surfaces contained adhesive peaks and ridges that were each between 2-5mm in length. Furthermore, the adhesive ridges contained exposed stitching implying that the crack front propagated through the adhesive interface and into the substrate itself. Despite the reduced load capacity of the specimens at LT, the substrate damage indicated that the bond strength was not the cause of failure. The low magnification images of the LT DCB fracture surfaces are shown in Figure 4.17.

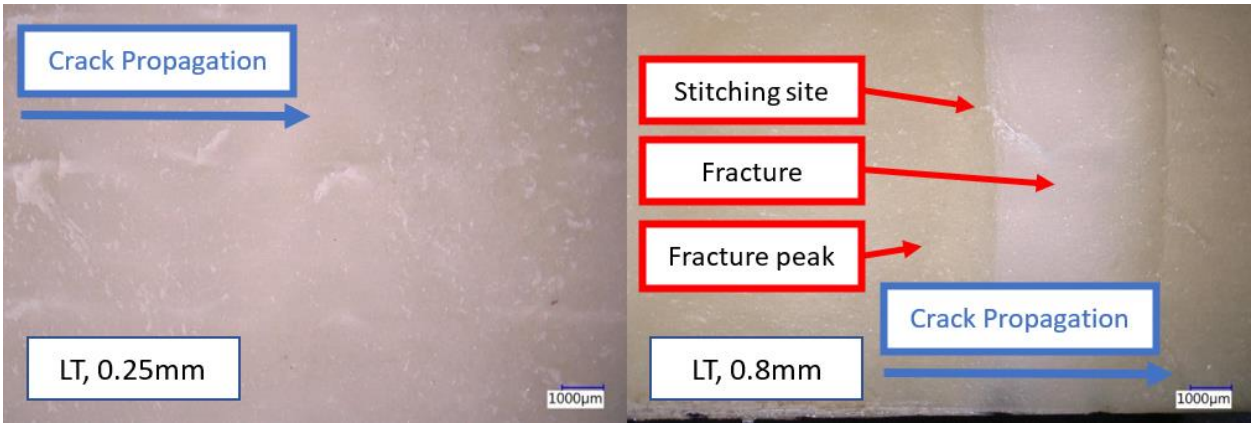


Figure 4.17: Fracture surface analysis of LT DCB specimens at (a) 0.25 mm, and (b) 0.8 mm bond-line thicknesses, with (b) showing oscillatory crack propagation.

The oscillatory crack tip propagation patterns were investigated in further detail using a 3D depth display feature on the Keyence microscope that generated a contour plot of the fracture surfaces and quantified the amplitude of the oscillations. The 3D depth display showed that the depth of the oscillations was equal to the initial bond-line thickness, confirming that the crack front oscillated between substrate surfaces. Oscillatory crack propagation in the adhesive layer during DCB testing was observed by Chen et al. who investigated the effect of residual stress on crack stability [114]. Chen et al. observed that the oscillation frequency was correlated with the degree of residual stress sustained during a preliminary tensile loading prior to the DCB test. Thus, it can be inferred that the discrepancy in CTE values between the substrate and the adhesive induced a residual stress in the specimens during the LT tests and contributed to the crack tip instability. Simultaneously, it can be inferred that the dominant failure mode for the adhesive during Mode I LT fracture was mostly cohesive as the crack tip propagated through the thickness of the adhesive layer itself. An image of the 3D depth display of each of the specimen thicknesses is shown in Figure 4.18.

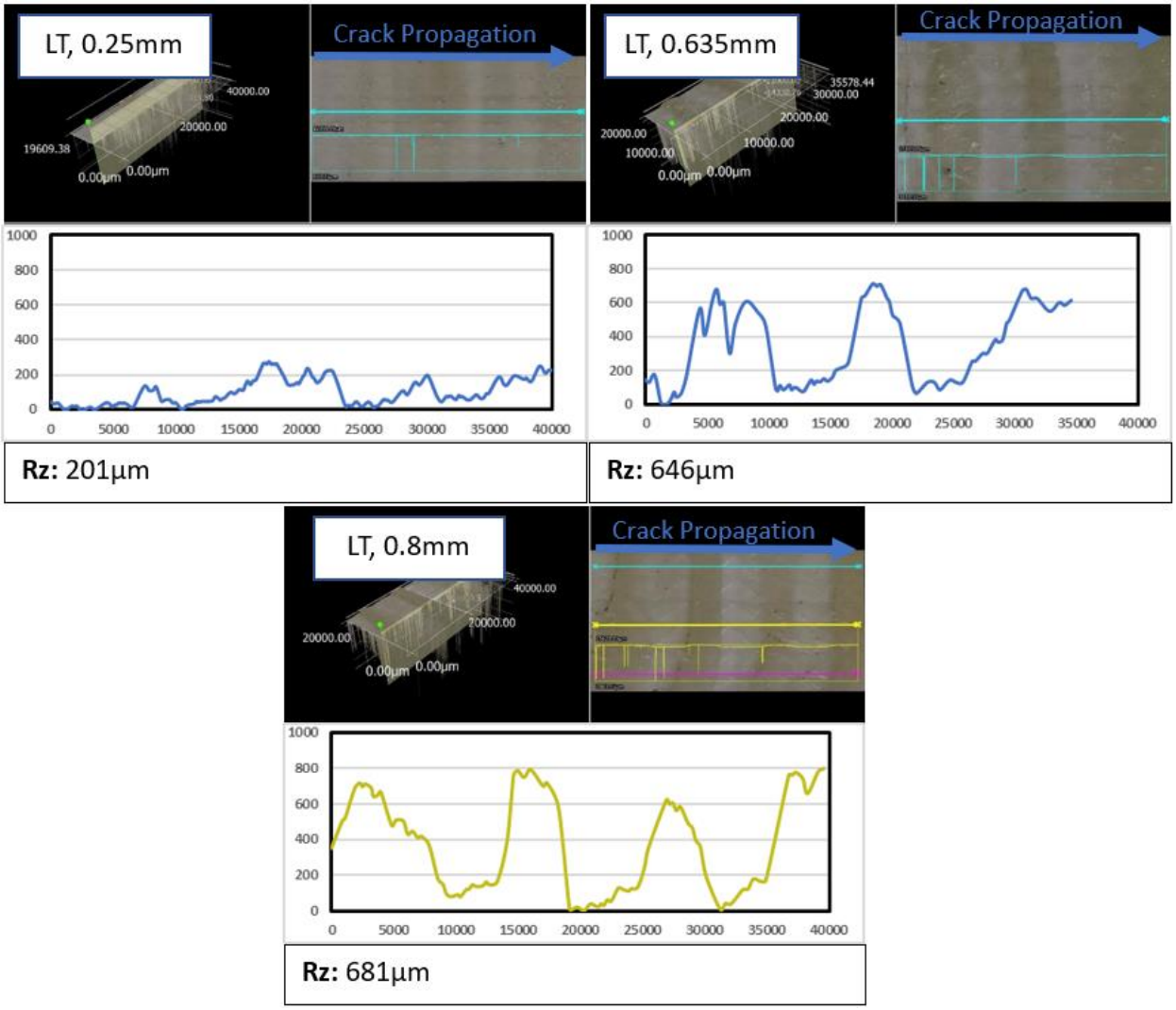


Figure 4.18: 3D depth display was used to characterize surface roughness for each (a) 0.25 mm, (b) 0.635 mm, and (c) 0.8mm adhesive bond-line thicknesses.

The 3D depth display was also used to assess the fracture surface of the thickest RT specimens, and it was observed that the Rz topographic variance was less than 200µm, as shown in Figure 4.19.

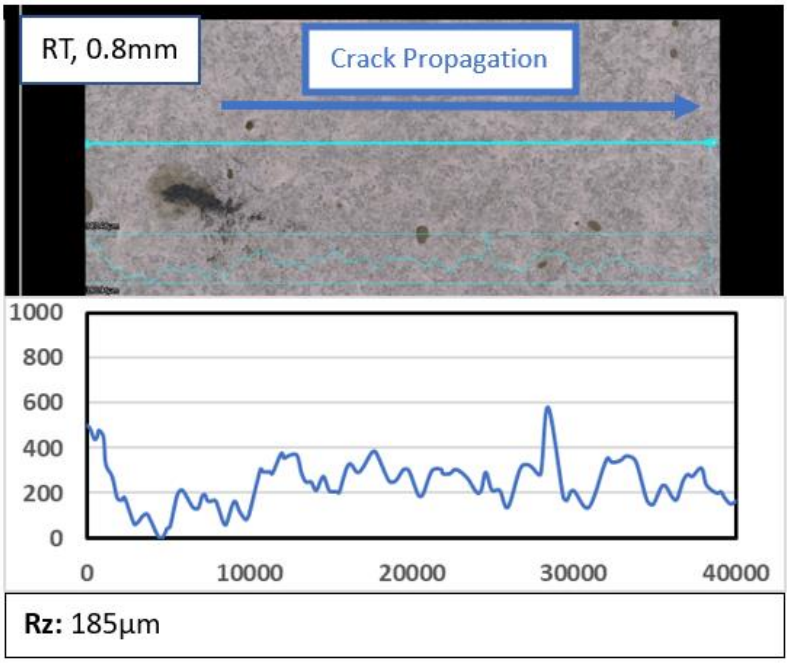


Figure 4.19: 3D Depth Display showed that the fracture surface of the RT DCB specimen with 0.8 mm bond-line thickness was uniform compared to the LT DCB specimens.

To verify that the adhesive failed in a cohesive manner throughout the entire layer, high magnification microscopic analysis was conducted on the fracture peaks and ridges. The high magnification analysis confirmed that – independent of the underlying thickness of the adhesive region – the fracture surface maintained a consistent appearance. The adhesive fracture surface was also compared with the un-bonded substrate surface at high magnification to ensure that the failure mode was not interfacial. While the LT fracture surface was smoother than the ductile cohesive failure shown by the RT specimens, the un-bonded surface was still smoother by comparison. A pure interface failure would have yielded a clean fracture surface like the un-bonded example, but this was not observed under the microscope [115]. The high magnification LT DCB fracture surface images are shown in Figure 4.20.

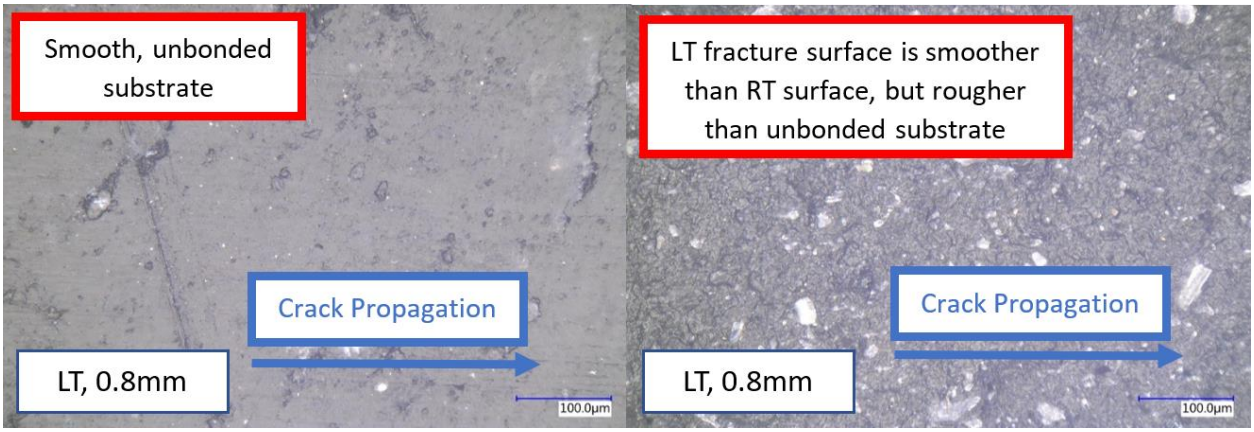


Figure 4.20: Comparison of (a) un-bonded fracture surface with (b) fracture valley region adhesive for LT DCB specimen at 500x magnification. The fracture surface contains a smoother, more brittle appearance than the RT DCB specimens, but the fracture surface is still distinctly less smooth than the un-bonded surface.

4.3.3. RT ENF Specimens

The fracture surfaces of the RT ENF specimens are analogous to those of the RT DCB specimens. A ductile failure mode was evidenced by a whitened fracture surface that formed in the FPZ, and the adhesive failed in a purely cohesive manner with an equal deposit remaining on both substrates. Compared to the RT DCB specimens, the RT ENF specimens had a greater amount of hackle formations in the adhesive layer, indicating shear failure. These hackles are shown in Figure 4.21.

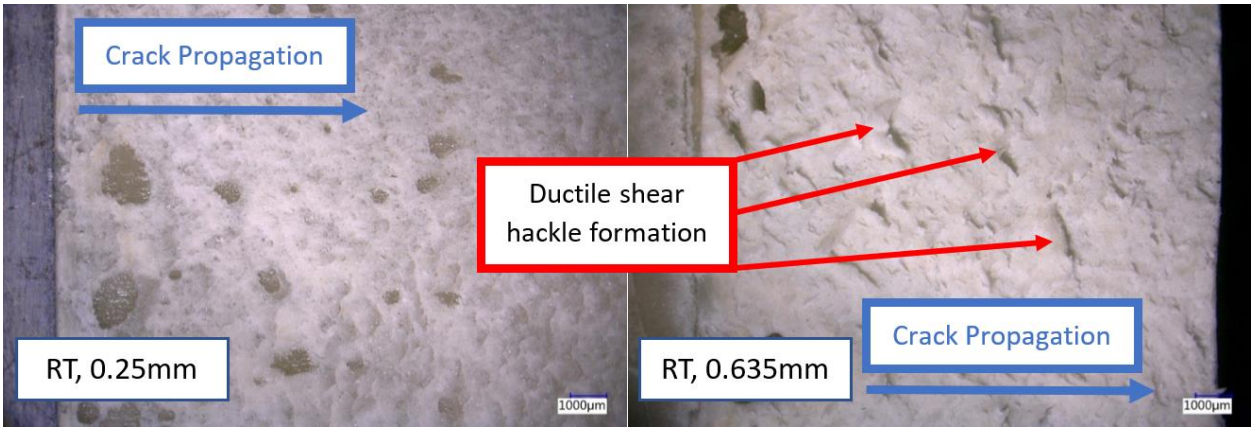


Figure 4.21: Fracture surface analysis of RT ENF specimens with (a) 0.25 mm and (b) 0.635 mm bond-line thicknesses at low magnification showing hackle formation during shear loading.

4.3.4. LT ENF Specimens

The LT ENF specimens failed in a brittle manner unlike the ductile failure modes observed with the RT specimens. Unlike the LT DCB tests, the LT ENF test specimens mostly experienced

fiber-tear failure within the substrate. Fractographic analysis showed a large degree of fiber pullout from each specimen irrespective of bond-line thickness, indicating that the adhesive bond was stronger than the substrate itself during LT shear failure. High magnification fractography for the LT ENF tests confirmed the brittle nature of the failure modes. Irrespective of bond-line thickness, the specimens contained either exposed fibers (within the damaged substrate) or fiber imprints (within the adhesive layer that remained attached to the undamaged substrate). The fracture surfaces within the tows contained shear cusps and fiber imprints, further signifying brittle failure. Unlike the LT DCB specimens, the LT ENF specimens did not experience the unstable, oscillatory crack tip propagation between the substrates. Nonetheless, the propensity for substrate failure implied that the discrepancy in CTE between the substrate and the adhesive was contributing to residual stresses in the composite. The fractographic images of the LT ENF tests are shown in Figure 4.22.

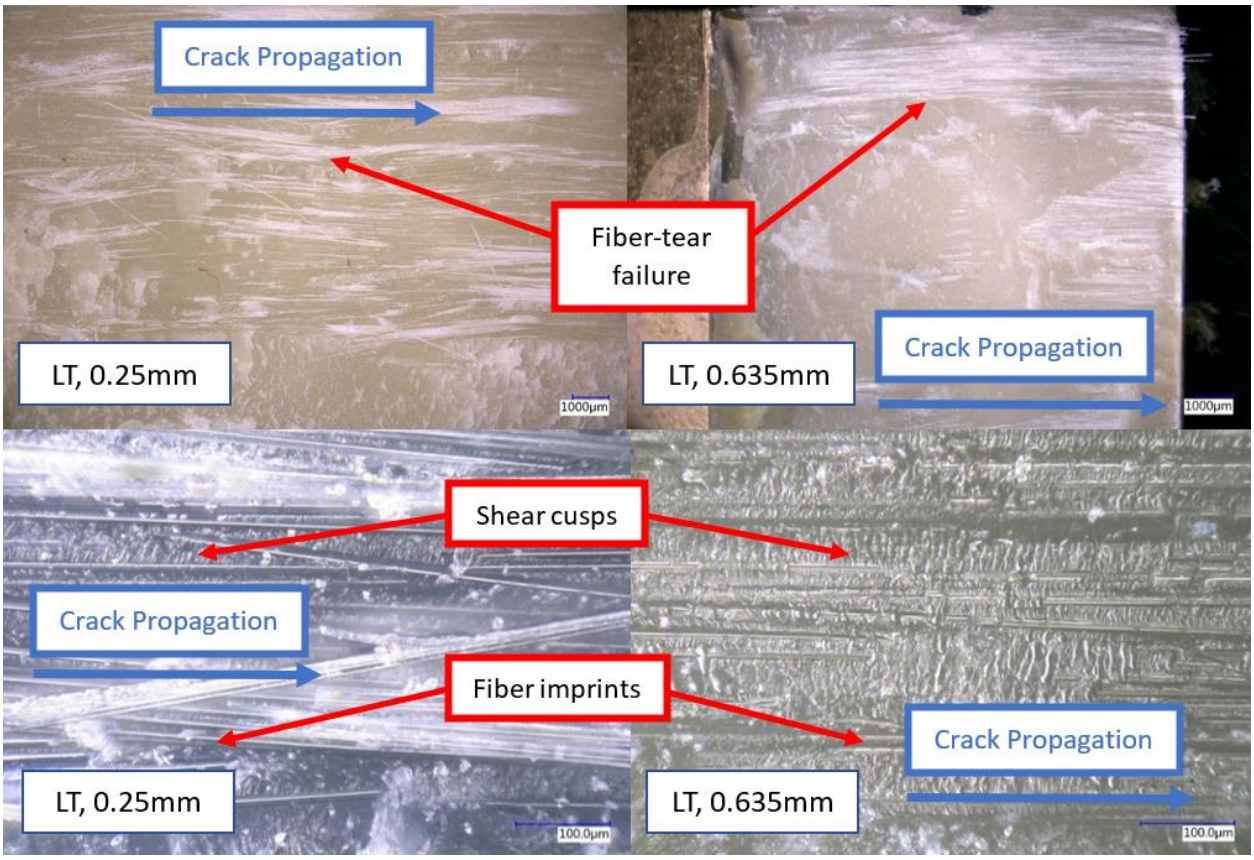


Figure 4.22: Fracture surface of LT ENF specimens. Low magnification images of (a) 0.25 mm, and (b) 0.635 mm bond-line thickness specimens shows fiber-tear failure within substrate, while high magnification images (c), (d) show shear cusps and fiber imprints indicative of brittle failure.

4.4. RT DCB Test Simulations

A finite element model of the RT DCB specimens was developed to calibrate the parameters of the bilinear TSL. A 2D planar shell model with cohesive elements (COH2D4 cohesive element type) employing a bilinear traction-separation law was used to model the adhesive layer. The model considered the DCB specimen geometries listed in Table 4-2 at each bond-line thickness, and the material properties for the substrate were taken from Shi (Table 4-1) [44]. The model was placed in displacement control at the location of the piano hinges. The upper hinge was pinned ($U1 = U2 = 0\ mm, UR3\ unconstrained$) while the lower hinge was prescribed a vertical displacement ($U1 = 0\ mm, U2 = -30\ mm, UR3\ unconstrained$). Structural elements were applied to the mesh, and a mesh refinement study was performed with convergence observed at an element size of 1.5mm. The meshed model is shown in Figure 4.23.

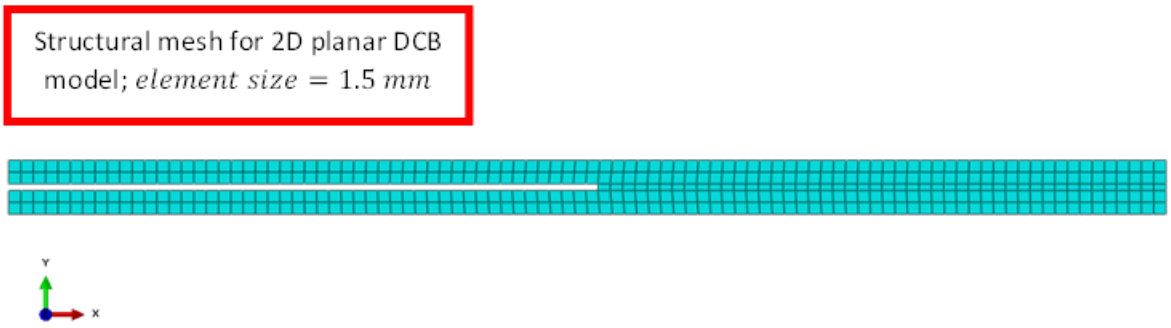


Figure 4.23: Meshed DCB model.

The G_{IC} values computed using the MBT data reduction scheme (Table 4-4) were used as the fracture energy inputs for the cohesive element model, while the elastic stiffness and peak tractions of the traction-separation curve were determined using an inverse parameter-fitting method. The numerical model was not sensitive to the peak traction and elastic stiffness, and this insensitivity is a characteristic of the DCB test setup [63]. The calibrated numerical parameters used in the traction separation law are presented in Table 4-5.

Table 4-5: Calibrated traction separation law parameters used in RT DCB ABAQUS numerical models.

Bond-line Thickness (mm)	Initial Stiffness (MPa)	Peak Traction (MPa)	Fracture Energy (MPa mm)
0.25	1000	15	0.892
0.635	500	15	1.23
0.8	2000	15	1.63

The predicted post-peak load-displacement response for each bond-line thickness correlated well with the experimental plots (Figure 4.24). However, the peak load from the numerical model did not fall within the scatter of the experimental data since the bonding of the shims to the substrates during physical trials effectively shortened the pre-crack length of the specimens. This caused an artificial increase in the elastic stiffness and a higher peak load compared to the numerical models. Even considering the inherently poor correlation with the elastic response of the experimental trials, however, the numerical model may struggle to accurately capture the peak response. A potential source of error in the numerical model is the use of a bilinear TSL that may not be adequately representing the ductility of the MMA adhesive. Thus, a trilinear (trapezoidal) TSL can be used to better predict the peak of the load-displacement curve for a ductile adhesive, but such a model is not available in ABAQUS CAE.

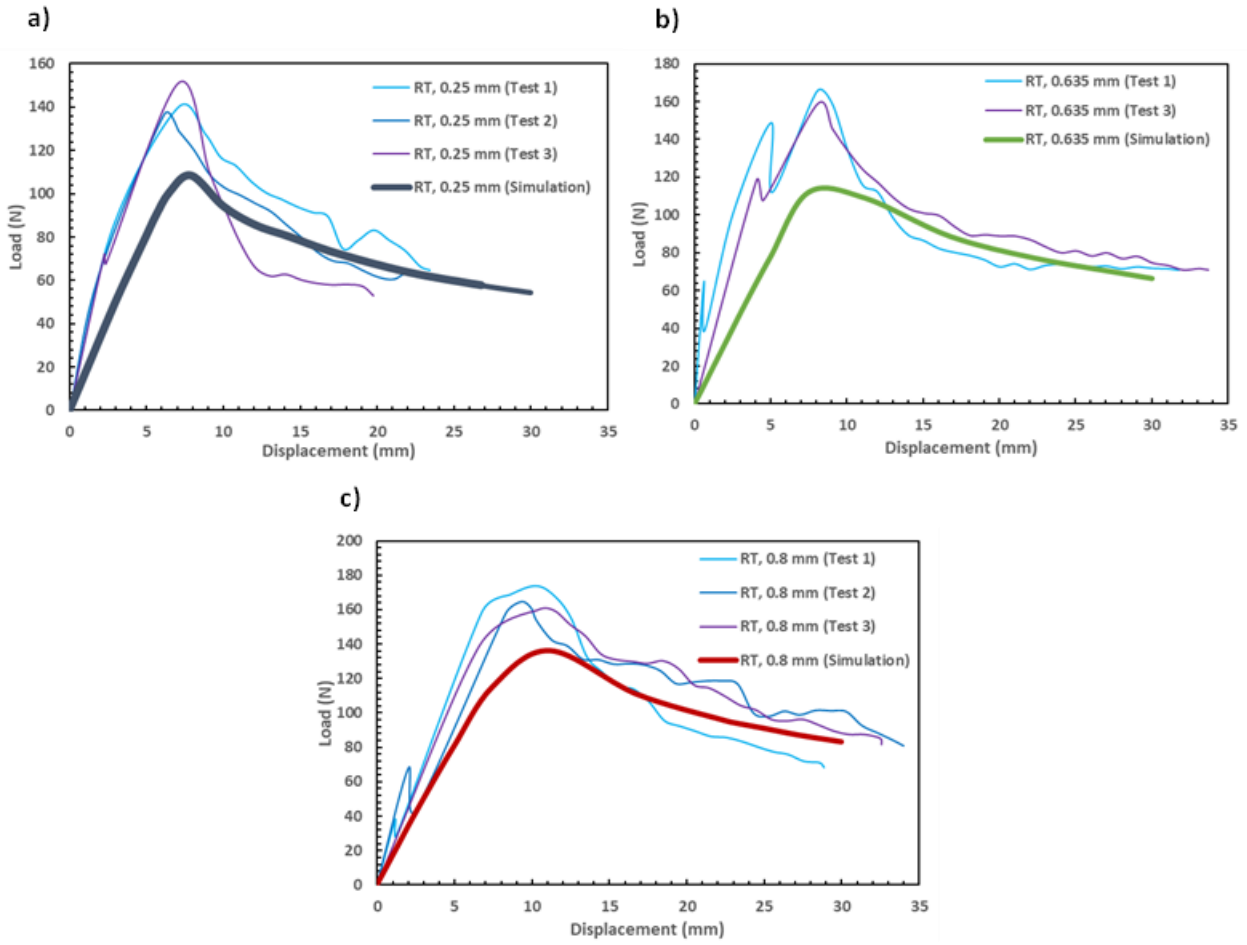


Figure 4.24: RT DCB experimental results vs. numerical simulation for each bond-line thickness.

Chapter 5: Turbine Blade Manufacturing

This Chapter presents the results of full-scale micro-generating wind turbine blade manufacturing. First, modifications made to the VARTM process developed for glass fiber UD-NCF thermoplastic panels (Chapter 3) are summarized, and the outcomes of the high-quality blade shell manufacturing trials are presented. Next, the adoption of the developed MMA adhesive joint procedure (Chapter 4) for bonding the two blade shells will be presented.

5.1. Blade Shell Mold Modification

A two-part composite mold previously used to fabricate the wind turbine blade shells via an autoclave process were adapted in this study for VARTM processing (Figure 5.1). Mold modifications involved plugging existing bolt holes to allow sufficient flange area for applying sealant tape and a vacuum bag without leakage (Figure 5.1). A marine-grade epoxy resin system (West System Six10) was used to fill each hole. After preparing the surfaces, the holes were countersunk on the lower side of the mold to create a mechanical stop that would prevent the resin plug from being sucked into the mold after repeated vacuum cycles. The mold side surface was covered with tape to ensure that the resin remained flush with the surface of the mold. The holes were filled with epoxy and held at ambient temperature for curing. A vacuum test was performed with a vacuum bag to ensure that there were no leakages through the plugged holes.

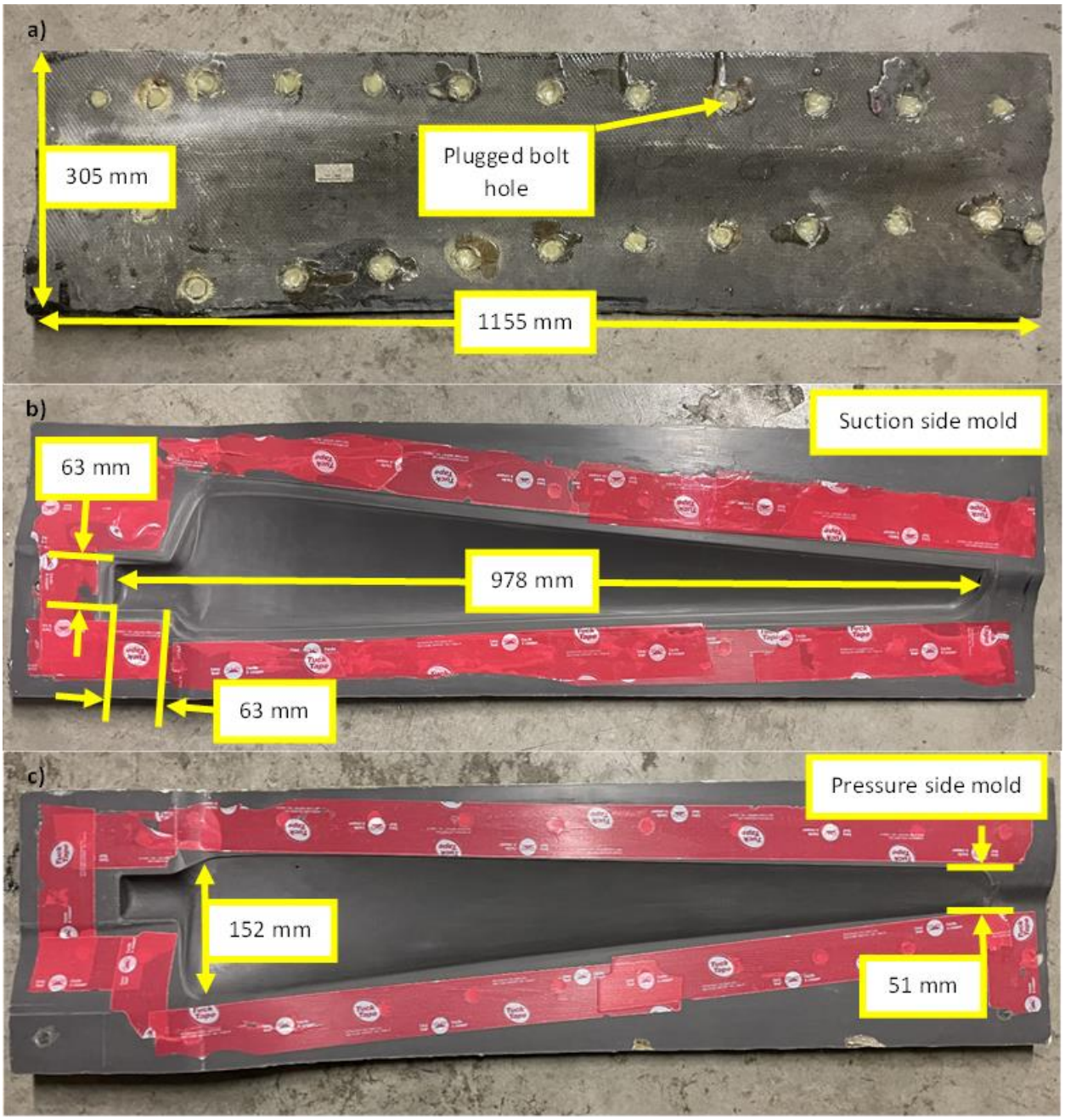


Figure 5.1: Blade shell mold overview with measurements: (a) back-side of suction side mold showing plugged bolt holes, (b) suction side mold, and (c) pressure side mold.

5.2. Blade Shell Processing

The VARTM process and consumables used for blade shell manufacturing was similar to that of the flat panels outlined in Chapter 3; however, there were a few key distinctions that will be highlighted in this Section. Note, the non-veiled UD-NCF was used for blade shell process trials

with an $[0]_4$ stacking sequence. A schematic of the VARTM process developed for the blade shells is shown in Figure 5.2 with material coordinate axes highlighted.

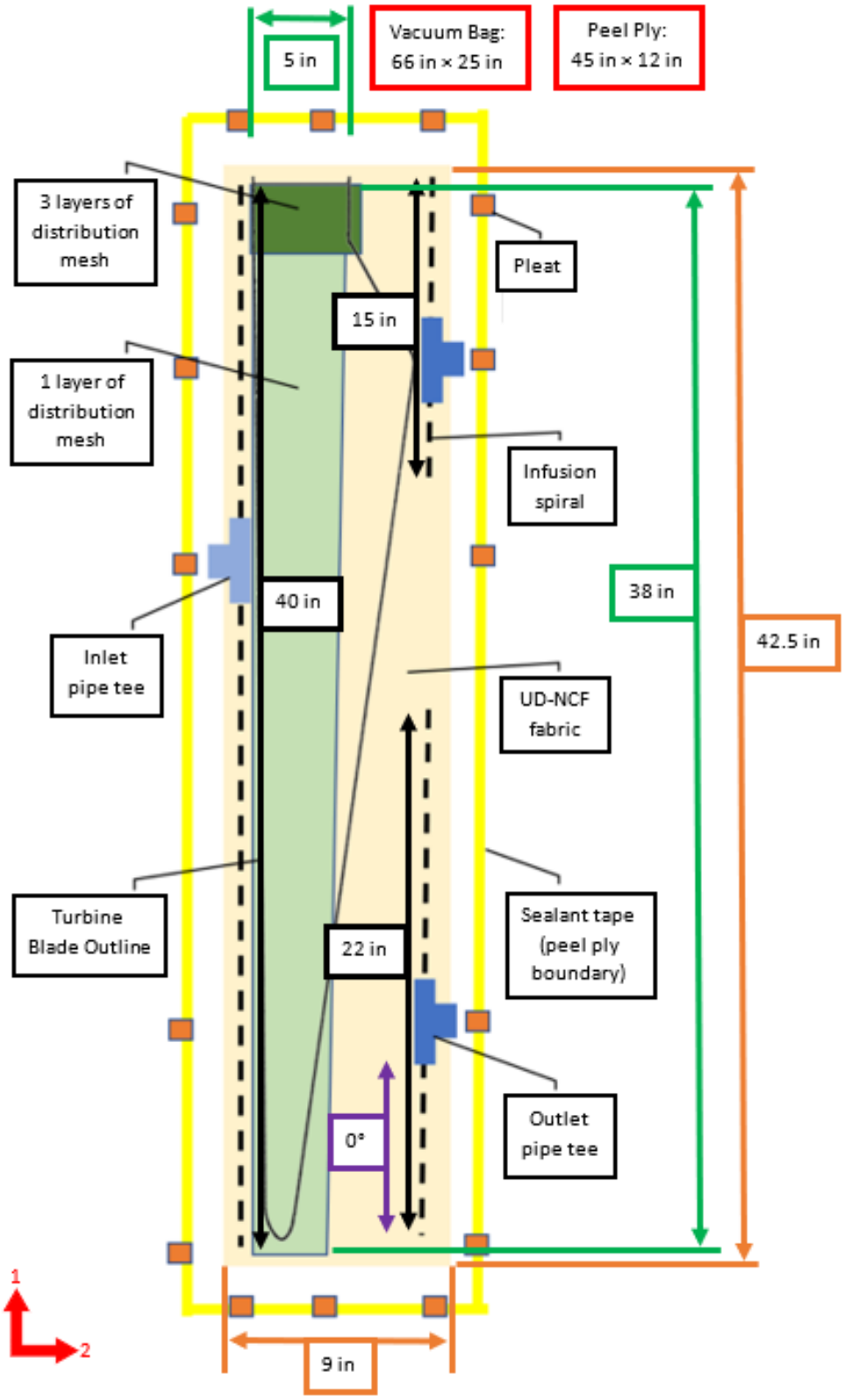


Figure 5.2: A schematic of the full-scale turbine blade shell infusion setup. Although the pressure and suction shell molds contained distinct geometries near the root, the infusion setup could be applied to both shells.

5.2.1. Vacuum Infusion Materials Setup

While the laminate materials were the same during flat panel and blade shell processing – including the same four layer stack of non-veiled UD-NCF (Saertex) with the stacking sequence $[0]_4$ – the dimensions for the blade shell laminate materials were modified to accommodate the blade geometry (Figure 5.2).

The fabric dimensions allowed a 1” flange around the periphery of the blade with a sufficiently large peel ply area to place the infusion spiral lines. The distribution mesh was cut to accommodate the entirety of the blade length and half the blade width starting from the inlet infusion spiral. The infusion spirals were cut to accommodate the length of the blade. For the blade shell, the width of the airfoil at the longest chord length was around 7”, meaning that a single infusion spiral along the leading edge would be able to infuse the entire blade geometry according to the line spacing guidelines outlined by Mahendran [95].

Unlike the flat panel trials, special attention was paid to the fabric compaction during layup to prevent race-tracking channels from forming. Mold conformity was particularly important for the pressure-side blade shell, which had a sharp concave corner near the root that could cause resin pooling. While the slim, aerodynamic profile of both blade shell halves allowed each mold to be approximated as flat towards the tips, the root geometries included sharp corners and steep draft angles that required cutting of the continuous fabric layers and adding small reinforcement strips to create an overlap joint around the reinforcement discontinuities. This technique is best demonstrated graphically in Figure 5.3, where the staggered cutting locations for the fabric are shown for each layer.

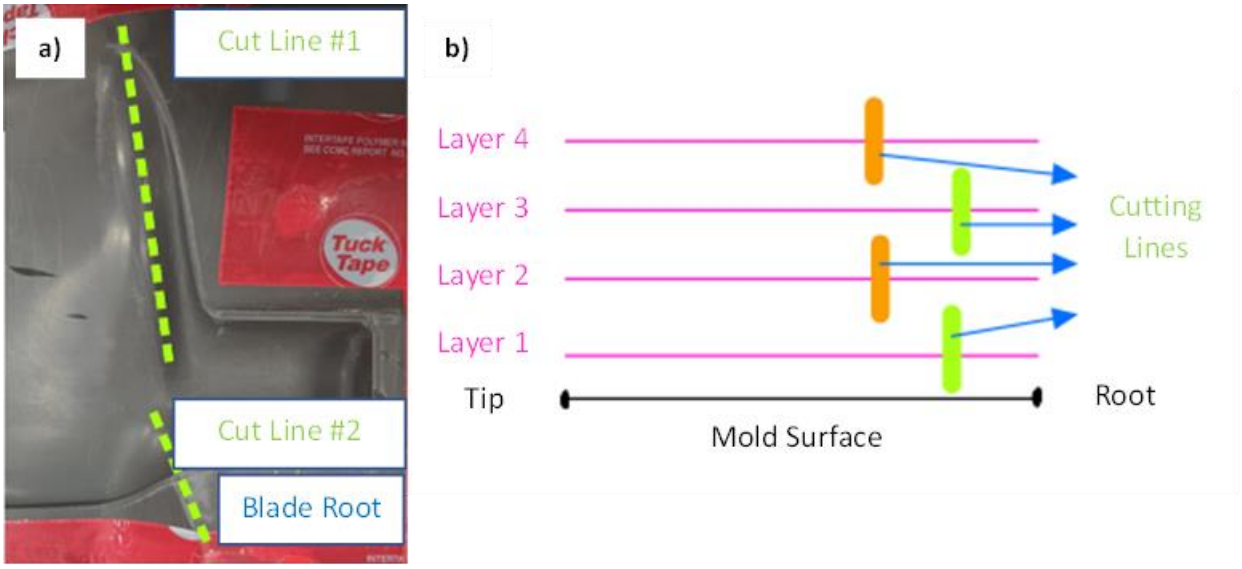


Figure 5.3: Fabric cutting and ply staggering for drapeability; (a) blade geometry contained sharp cutaway that requires cuts in the UD-NCF fabric to allow for draping. These cutting lines are reinforced with fabric strips with fibers along the direction of the cutting lines, and (b) the cutting lines were staggered between layers (not to scale) to limit localized resin pooling.

By convention, the reinforcement strips were at least 1" long to retain the fiber load bearing capabilities. Jin et al. demonstrated that the mechanical strength of overlapped composite joints between fabric layers achieved a consistent strength at overlap lengths of 0.5" and above [116]. Thus, a reinforcement butt joint with 1" in length would be sufficiently long to overlap each half of the cut fabric by 0.5" and retain the mechanical performance. The cutting location for the fabric was staggered by approximately 1" between layers to prevent localized resin-rich regions from forming at a single cutting location. Falcó et al. demonstrated that a staggered overlap joint configuration through the laminate thickness reduced the propensity for localized resin rich gap formation that could lower the strength of the composite [117]. Similarly, Tang et al. found that an increasing stagger distance between cuts in the plies would gradually increase the strength of the composite [118].

The complexity of the blade geometry also created problems when trying to conform the peel ply to the mold. Thus, additional peel ply strips were required near the root to prevent the fabric from bridging and forming dry spots in the laminate. Strips of peel ply were overlapped ad-hoc around the root and held together with spray-tack adhesive to prevent the fabric from contacting the vacuum bag or the distribution mesh. Figure 5.4 shows the full fabric and peel ply layups near the complex blade root geometry.

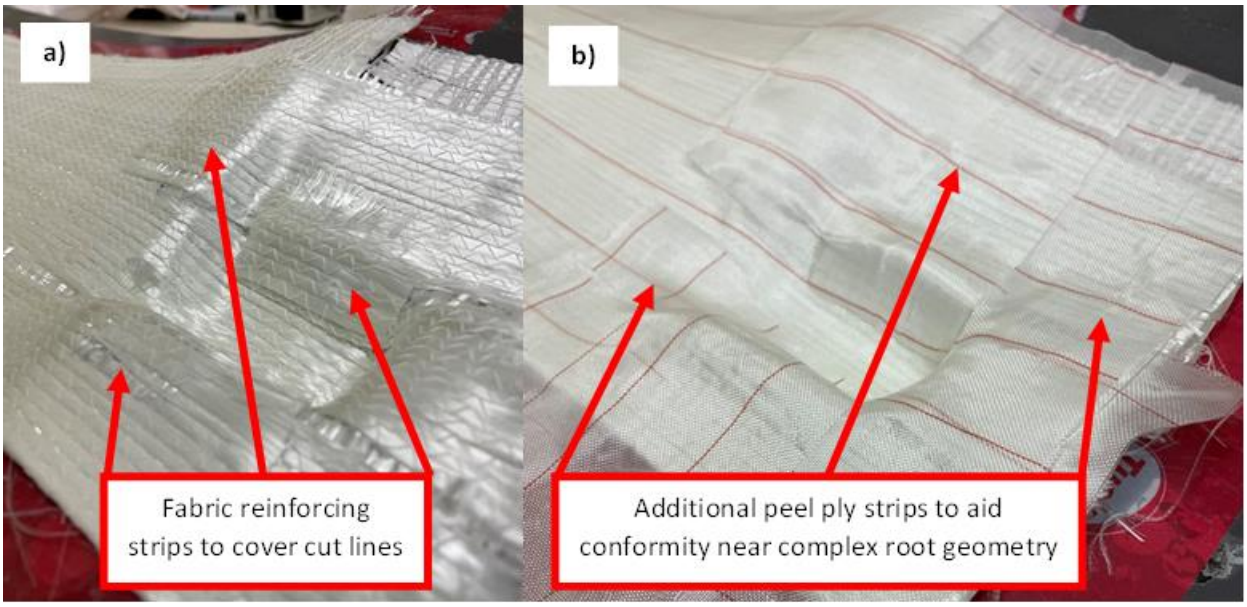


Figure 5.4: The fabric and peel ply layups; (a) fabric layup with reinforcing strips covering the cutting lines in the continuous layers, and (b) the arrangement of the peel ply with overlapped reinforcement strips that enabled conformity to the mold while completely covering the fabric around the root.

The distribution mesh setup broadly mirrored the flat panel setup by covering half of the laminate starting from the inlet infusion line and allowing the resin to flow along the width of the diamond pattern. However, the cylindrical root required extra layers of distribution mesh (2-3 total layers) to further increase the localized flow rate relative to the flow in the flatter sections near the tip. The depth of the cylindrical root increased the total flow distance, and additional mesh layers were needed to maintain an even flow front across the blade. The inlet infusion spiral was placed on the leading edge of the blade, and the outlet infusion spiral was placed on the trailing edge. Thus, the resin was allowed to flow in a transverse direction to the fibers, mirroring the fabric orientation outlined for the flat panel processing. Unlike the flat panel procedure, the blade shell setup also used infusion spirals at the outlet to help unify the flow front. Two unconnected infusion spirals were used on the outlet side: one of the spirals covered approximately a third of the blade length from the root, while the second spiral covered most of the remaining two-thirds of the blade length. This enabled greater control of the resin flow into the low permeability root (due to higher geometric complexity) and high permeability tip (approximately flat), simultaneously. If the flow at either end was accelerated, the advanced flow front could be arrested by closing either of the outlet vents, allowing the remaining laminate stack to be infused without dry spot formation. Both outlet infusion spirals were wrapped around a pipe-tee that was fed onto the outlet tubing; these

two outlet tubes then shared a pipe-tee outside the mold and were connected to the resin trap. Although the flow front could be controlled independently for both halves of the blade shell, the vacuum was pulled from a single pump. The configuration of the distribution mesh at the blade root and the infusion lines are shown in Figure 5.5.

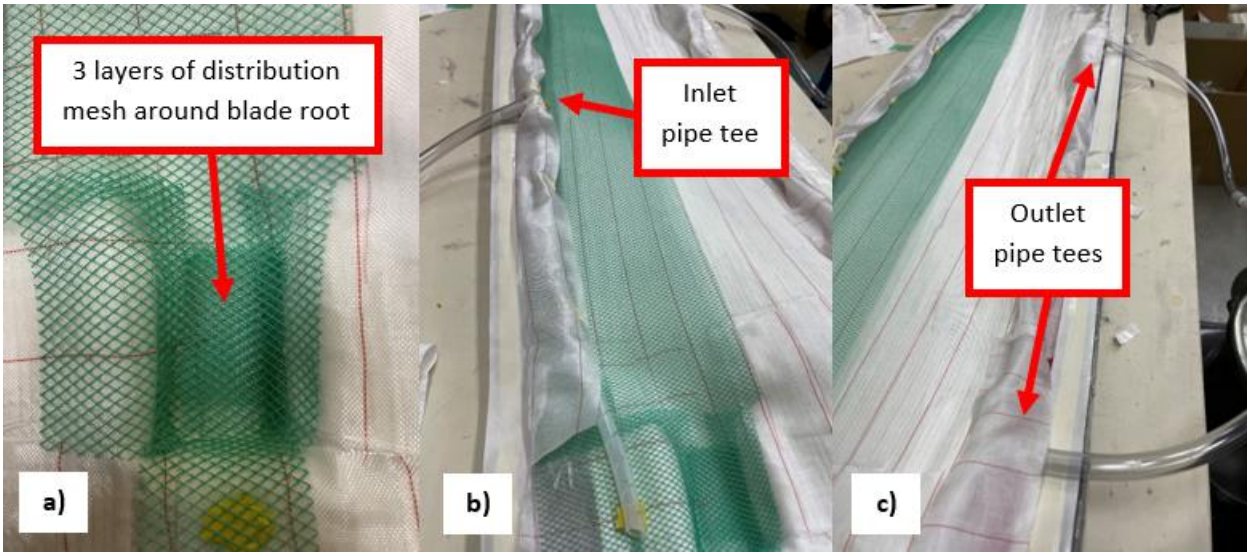


Figure 5.5: The distribution mesh and infusion line layouts; (a) distribution mesh layout at the blade root used extra layers to increase the flow velocity due to the increased flow distance caused by the depth of the root, (b) the inlet infusion spiral used a single pipe-tee connected to the inlet line to the resin source, and (c) the outlet infusion spirals used two pipe-tees to connect to outline lines that fed to the resin trap.

5.2.2. Blade Shell Vacuum Bagging

The procedure for the vacuum bagging of the blade shell molds closely follows the setup described for flat panel fabrication. The pleat techniques described in Chapter 3 are used, except that more pleats are required due to the size and complexity of the mold. The mold geometry requires 5 pleats along the length of the mold, and 3 pleats along the width of the mold. The pleats accounted for topographical variances in the mold stemming from the blade root geometry, the blade profile, and the infusion lines, spirals, and pipe-tees. Figure 5.2 outlined the layup and vacuum bag setup and highlights the positions of each pleat along each side of the sealant tape.

Pleat technique *A* was used for the middle pleat on each side (i.e, pleat 3 along the length from the left and pleat 2 along the width from the bottom of the schematic shown in Figure 5.2), while technique *B* was used for the remaining pleats. Where possible, the pleat was placed directly on an infusion line (i.e., pleat 3 on the inlet side and pleats 2 and 4 on the outlet side were placed on an infusion line). After completing the vacuum bagging procedure, a partial vacuum was

applied to remove the bag wrinkles on the planform area of the blade to limit the race-tracking effect before starting a 25-minute drop test to verify the bag integrity.

5.2.3. Resin Mixing and Infusion

For a blade shell with 4 layers of Saertex fabric, 650g of Elium® resin with 2-3% by weight peroxide initiator was required to completely impregnate the mold. The resin and initiator were mixed for 15 minutes before sitting for 5 minutes to evacuate excess air bubbles. Due to the layout of the infusion spirals and the width of the blade, the infusion required roughly the same time as the flat panel molds due to the comparable flow distances across the laminate surface. The flow rate was partially choked by an inlet clamp as the resin flowed through the distribution mesh, and the clamp was removed once the distribution mesh was fully impregnated. Depending on the trial, the resin flow front through the root or tip would lead. Either scenario would result in a high-quality blade shell provided that the leading flow was arrested by closing one of the two outlet vents to unify the flow front as the outlet infusion lines were reached.

5.2.4. Demolding and Cleaning

Demolding the blade shell required greater effort than the flat panels, particularly around the blade root. A single brass putty knife was generally sufficient for demolding the flat panels (sometimes requiring a second knife for thick parts), but multiple knives were required to gradually break the vacuum seal for the full-scale blade shell. The tip of the blade created the weakest vacuum seal. Thus, the putty knives were gradually advanced from the tip towards the root of the blade with increasing pressure. Once the thickest chord of the blade was reached, additional pressure was applied around the root to pop the blade out of the mold. Once the blade was removed, the mold was cleaned to prepare for the next cycle using the techniques described in the flat panel process.

5.2.5. Trimming and Post-Processing

Full scale turbine blade manufacturing required trimming and sanding of the blade shells prior to bonding since the layout of the polymerized composite produced excess flanges that were up to 2-3” wide. A fixture design that would enable the use of handheld tooling during post-processing was deemed expensive and difficult to manufacture. Thus, industrial-grade vertical band-saws and belt sanders were used to trim the blade shells and prepare them for adhesive bonding.

The vertical saw was used to cut the flanges, leaving a 5 mm perimeter around the blade profile. The excess flange was subsequently sanded until the blade outline was flush with the mold features. Occasionally, the heat from the saw or the belt sander would char the cutting surface, but this was alleviated with a slower cutting feed rate or a smaller applied force during sanding, respectively. Complex geometries such as interior angles were finished using a rotating cylindrical belt sanding tool. The finished blade shell is shown in Figure 5.6.

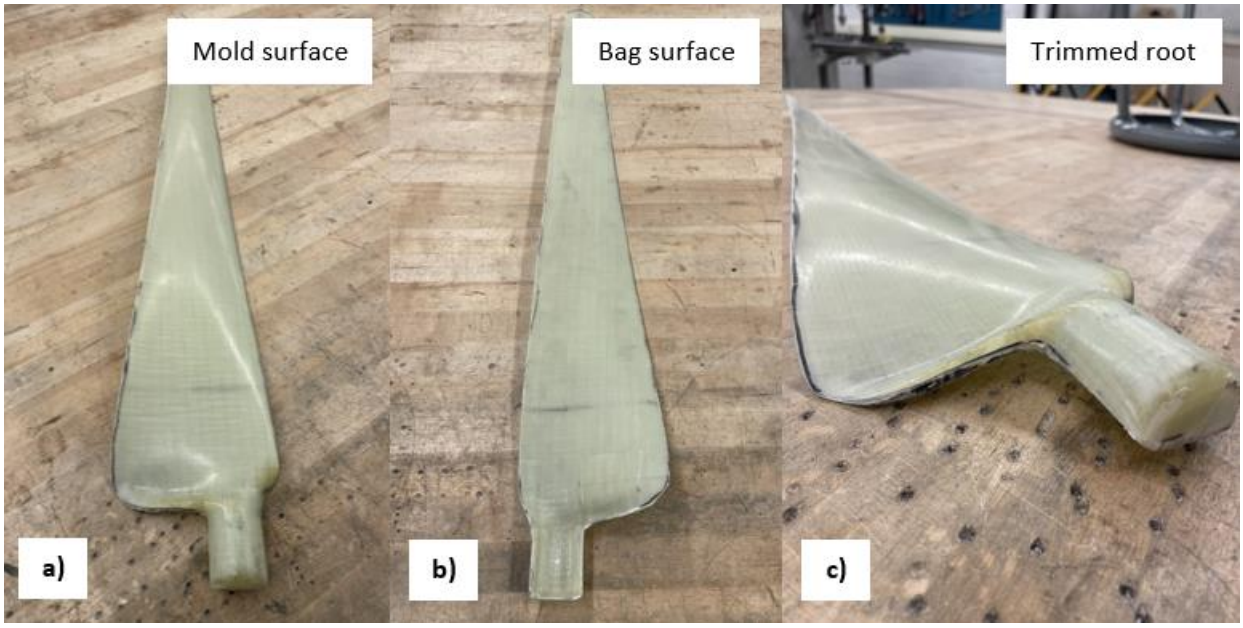


Figure 5.6: Blade shell after trimming and sanding from left to right (a)-(c); (a) outer surface of blade shell with smooth finish, (b) inner surface of blade shell with rough texture from peel ply, and (c) blade root showing complex geometry.

Once each shell was individually trimmed, the shells were aligned to identify any bonding surface interferences. The thickness of the shells required additional sanding along the interior geometries to ensure a compatible fitment. The blade shells were gradually grinded down on the vacuum-bag surface until the interferences were cleared. The contours near the root of the blade were similarly adjusted to achieve the desired fit. Once the grinding and alignment was completed, the blade shells were ready for bonding.

5.3. Blade Shell Process Overview

Like the flat panel process, the dimensions of the turbine blade allowed the resin to flow along the transverse fiber direction, enabling the peel ply and distribution mesh setup to be directly adapted from the flat panel setup. The largest discrepancy between the flat panels and the blade

shells was the sharp corners near the blade root that necessitated modified layup processes to prevent resin pooling and starvation. A feature of the blade that routinely caused defect formation was a sharp concave corner geometry near the root of the pressure-side mold that created a race-tracking channel, which contributed to resin pooling on the mold surface. The cylindrical blade root also routinely suffered from defect formation. The blade root feature contained a sharp convex corner that abruptly transitioned into a half-cylinder around 1" in diameter. This combination of geometries prevented the fabric from completely draping around the convex corner without cuts in the continuous fabric. Unlike the sharp concave corner that suffered from resin pooling, the convex corner increased the localized compaction pressure on the laminate stack leading to dual-scale flow through the root geometry and incomplete wet-out of the fabric.

Due to the small scale of the blade that allowed for overlap with many flat panel processes, minimal process iteration was required to optimize the blade shell production method. Difficulties with conforming the continuous fabric to the complex root geometries meant that the fabric cutting scheme outlined in Section 5.2.1 was a requirement even with the initial trials. Thus, discrepancies in part quality between trials were attributed to poor workmanship. Summarily, if the operator ensures that the fabric is draped tightly to the mold, the ensuing part quality would be acceptable. Conversely, if the layup process was rushed, the part would likely be rejected. It should be noted that the blade shells fabricated for this work did not incorporate a stacking sequence that would be representative for a production-ready part. Unlike the prototype blades that used an $[0]_4$ stacking sequence, the production stacking sequence of the blade might incorporate $\pm 45°$ layers to account for torsional rigidity requirements. This may cause non-uniform permeability depending on the fiber orientation. The fiber orientation may also affect the fabric draping and would also have to be considered for the layup procedure during volume production.

5.4. Blade Shell Assessment

Like the flat panel trials, the key marker for assessing blade shell quality during process optimization was the visual identification of resin starvation. Additionally, the concave corners along the root of the blade shell were susceptible to resin pooling. The technical challenges with assessing the V_C of the composite described in Chapter 3 (related to acid digestion, TGA, and CT scanning) persisted when attempting to quantify the V_C of the blade shells. Nonetheless, the relatively flat aerodynamic profile towards the blade tip meant that the results observed during flat

panel trials would be valid for significant portions of the blade shell, while the clarity of the resin dry spots meant that visual inspection was sufficient to ensure blade quality near the root. A comparison between a poor-quality blade shell comprising regions with resin pooling and incomplete compaction and a high-quality blade shell are shown in Figure 5.7. Note, the trimmed and post-processed blade shell in Figure 5.6 represents a high-quality part that was produced using the techniques outlined in this chapter.

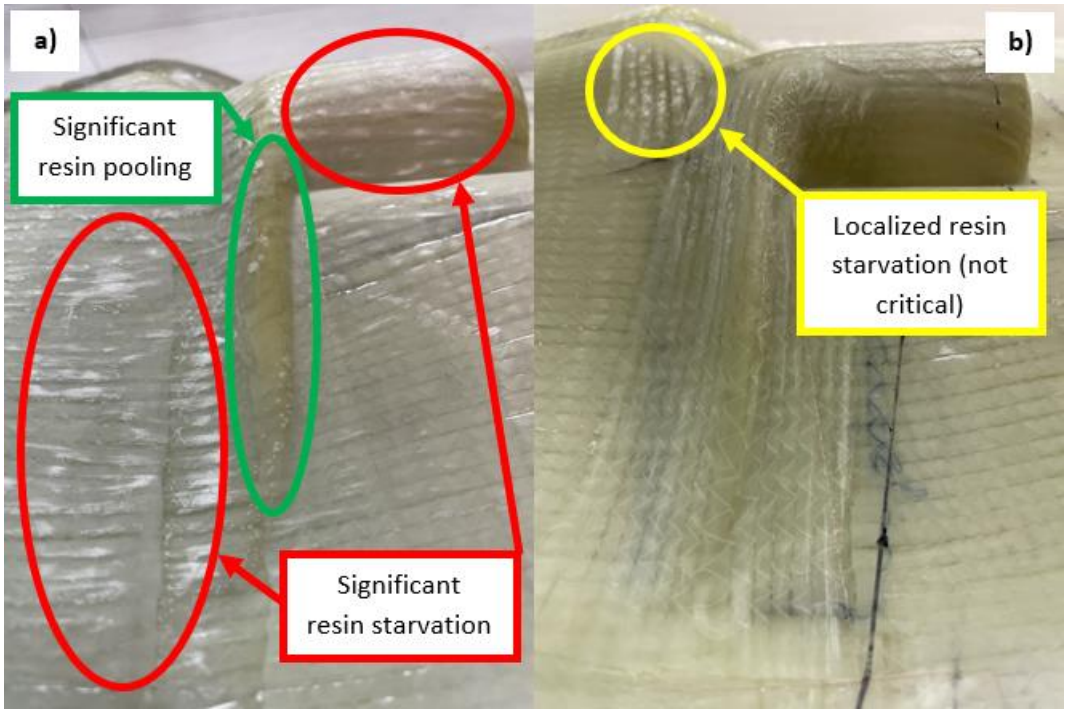


Figure 5.7: Comparison between poor- and high-quality blade shell root; (a) poor-quality blade shell root with resin pooling encircled in green and poor laminate wet-out encircled in red, and (b) high quality blade shell root without resin pooling. Some regions of the blade shell experienced poor wet-out (encircled in yellow), but these regions were also thicker due to reinforcement strips during layup and were not a structural concern.

5.5. Blade Bonding and Post-Processing

Without a dedicated alignment tool for blade shell bonding, alignment of the proof-of-concept turbine blade was done by eye. After grinding the blade shells to ensure a smooth overlap for the bonding surfaces, the blade was marked and secured with C-clamps to ensure that the perimeter of the shells (particularly around the trailing edge) did not contain any interferences. Once the trial fitment was completed, the blade was ready for bonding.

Using the bonding techniques developed during DCB and ENF testing, 4 beads of adhesive were applied on each bonding surface. This was sufficient adhesive quantity to achieve the target

bond-line thickness with minimal excess squeeze-out. A spatula was used to distribute the adhesive evenly across the face of the bonding surfaces. Without an alignment tool, the shells were adjusted by-hand. The blades were subsequently clamped together, and the adhesive was allowed to polymerize overnight. The post-processing procedure for the bonded blade involved cosmetic work with a belt sander to ensure that the aerodynamic surfaces were smooth. The adhesive would polymerize in a gummy manner if the bonding surface was excessively narrow, or the pressure was insufficient during polymerization. Otherwise, the adhesive would polymerize as a hard plastic if the bonding area was secured properly. In either instance, the belt sander adequately removed the excess resin to clean the aerodynamic surfaces.

5.6. Blade Shell Bonding Results



Figure 5.8: Bonded micro-generating wind turbine blade made with GF UD-NCF reinforced thermoplastic resin.

The blade shell bonding was completed as a proof-of-concept exercise instead of a structural representation of the full-scale blade (Figure 5.8). Nonetheless, the limitations of the current blade design for full-scale assembly were exposed during the proof-of-concept exercise. The leading edge of the blade posed significant design challenges. Unlike the trailing edge that overlapped two surfaces with complimentary concavities, the leading edge created a steep approach angle from the top and bottom shells that meant the adhesive would have to be bonded along the thickness of the composite, significantly reducing the joint integrity. A visual representation of the bonding surfaces is shown in the schematic in Figure 5.9.

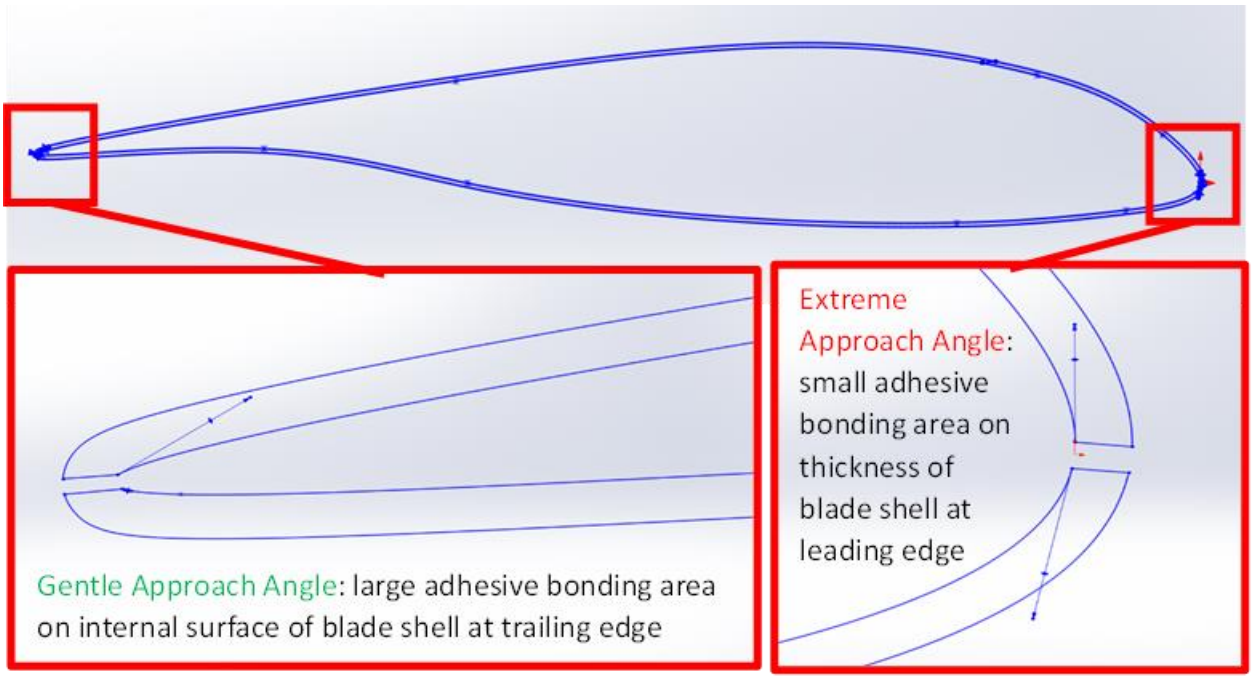
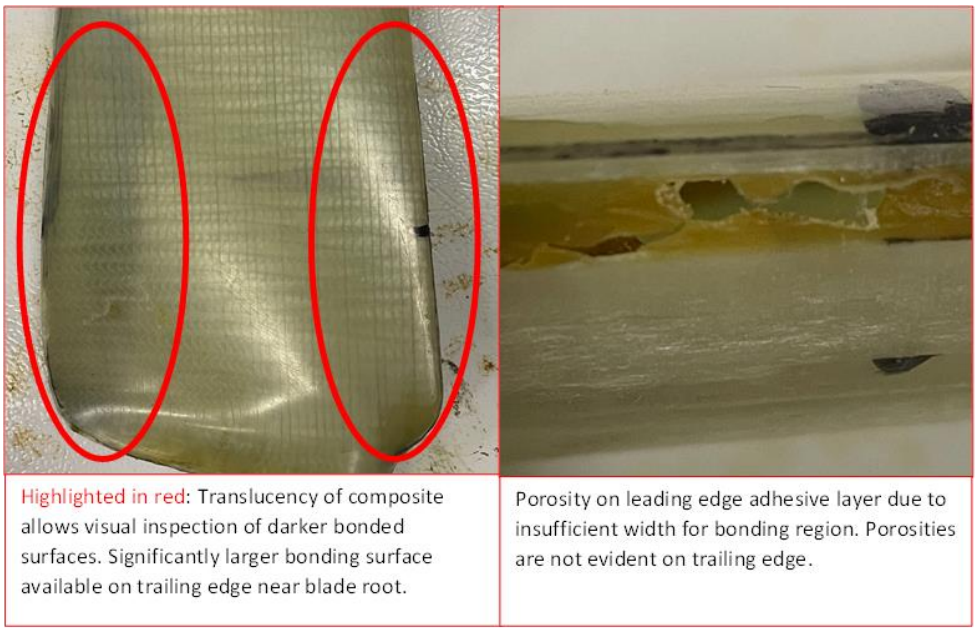


Figure 5.9: Comparison between the bonding surfaces for the trailing edge (that allows for a strong, wide adhesive joint along the internal geometry of the blade shells) and the leading edge (that forms a weak adhesive joint along the thickness of the blade shells).

The translucency of the composite provided a visual indication of the integrity of the bonded surfaces. Observing the leading-edge bond directly, there were obvious porosities and cracks in the adhesive layer. Adhesive characterization work showed that the Bostik MMA adhesive changed colour depending on the degree of polymerization. If sufficient pressure was applied to the bonding surface and the width of the adhesive area was sufficiently large, the MMA adhesive would polymerize into a hard, green plastic material. Without a good contact area, the MMA adhesive would polymerize into a rubbery, brown material that was incapable of supporting load. The bonded leading edge of the blade shell was dominated by this poorly polymerized rubbery material. Altogether, the proof-of-concept blade assembly highlighted the need for a redesign of the blade assembly procedure. The defects observed during the adhesive joining of the blade are highlighted in Figure 5.10. The blade shell assembly concepts are presented in Appendix A3.



Highlighted in red: Translucency of composite allows visual inspection of darker bonded surfaces. Significantly larger bonding surface available on trailing edge near blade root.

Porosity on leading edge adhesive layer due to insufficient width for bonding region. Porosities are not evident on trailing edge.

Figure 5.10: Defects observed during adhesive joining of micro-generating wind turbine blade shells.

Chapter 6: Discussion

6.1. Flat Panel VARTM Processing

Compared to the setup outlined by Rosso [21], process quality and consistency were improved by increasing the power of the vacuum pump, placing pleats in the vacuum bag film that limited bridging, minimizing the planform area of the distribution mesh, and using a spiral infusion line from the inlet gate instead of a point inlet. These modifications were introduced to mitigate defect formation stemming from transverse flow, dual-scale flow, resin starvation caused by the race-tracking effect, and inconsistent compaction pressure [11], [42]. The elimination of resin starvation around the inlet of the mold implies improved laminate compaction uniformity due to the implementation of a pleated vacuum bag technique.

A primary requirement for a high-quality VARTM part was a pump that could create a nearly perfect vacuum, allowing for the transport of voids out of the laminate stack. Transverse flow defects were mitigated by reducing the surface area covered by the distribution mesh to reduce the discrepancy between the flow velocities through the distribution mesh and the laminate stack [11]. Additionally, the width of the distribution mesh was adjusted to delay the flow front from reaching the edges of the laminate and reduce the race-tracking effect, reducing the risk of resin starvation. An infusion spiral was incorporated at the inlet to quickly distribute the resin across the width of the laminate and create a uniform flow front. Finally, pleats were added to the vacuum bagging procedure to improve process quality and repeatability by maximizing the laminate compaction and preventing the vacuum bag from bridging, which may lead to resin pooling and void formation as shown by Bloom et al [42].

V_f analysis showed that the inclusion of an un-dissolved polymeric veil in a UD-NCF decreased the V_f of the composite panels by 8.2%. For the panels without a veil, the V_f was measured around 46.2%, which was comparable with results from van Oosterom et al. for glass fiber UD-NCF composite parts produced via SCRIMP processes (47.5%). The areal density of the fabric may have adversely affected fiber nesting by increasing the resistance of the laminate stack to compaction, contributing to lower V_f values [26]. Additional improvements in part quality may be found by cyclically compacting the laminate stack. For instance, the CAPRI process has shown

that compaction and relaxation cycles can further increase fabric nesting prior to infusion [49], [52], [54].

6.2. Adhesive Testing

The performed DCB and ENF tests revealed that the MMA adhesive and surface preparation method used for the glass fiber/thermoplastic substrates represent a suitable adhesive joint. The load-bearing capabilities of the MMA adhesive increased with increasing bond-line thickness at RT for both Mode I and Mode II tests, while the stiffness of the samples remained consistent for all bond-line thicknesses considered. The adhesive experienced highly ductile failure at room temperature, characterized by a large process zone (approximately 15mm length) with significant whitening. Conversely, at low temperature conditions, the adhesive experienced reductions in peak load and displacement at failure for both Mode I and Mode II test conditions when compared to the RT conditions. Additionally, the adhesive failure mode transitioned from highly ductile to highly brittle, characterized by stick-slip behavior in the load-displacement curve and sudden crack propagation. The bond-line thickness did not have a noticeable effect on adhesive performance at low temperatures; however, the elastic stiffness of the adhesive increased at low temperature when compared to RT conditions. Numerical simulations using an ABAQUS cohesive element model showed consistency with the experimental trials. Similar to observations made by Dehaghani, it was found that the calibrated DCB model was not sensitive to the peak traction and initial stiffness values of the bilinear TSL [63]. Thus, additional tests are required to extract these values. However, the peak response of the load-displacement curve for a ductile response might be better captured by a trilinear (trapezoidal) TSL.

Microscopic fractography was used to investigate the failure modes of the adhesive for each failure condition. While the fracture surfaces for the Mode I samples at room temperature implied a tearing failure mode, the Mode II samples showed hackle formations indicative of shear deformation. The Mode I fracture surfaces at low temperature showed a distinct crack propagation pattern that oscillated between substrate surfaces in a wave formation. Such an oscillatory adhesive fracture surface was observed by Chen et al., who found that the amplitude and frequency of the oscillations was correlated with the degree of residual stress present in the adhesive layer prior to destructive testing [114].Topographic characterization showed that these oscillations spanned the full thickness of the adhesive layer, and high magnification microscopic fractography for the LT

samples showed that the failure mode was not at the adhesive interface. Thus, it was theorized that discrepancies in thermal expansion between the adhesive and the composite was contributing to residual stress formation in the adhesive layer and reducing the load-bearing capabilities of the joint at low temperatures. This theory was further supported by Mode II testing at low temperature, which showed that the joint was consistently experiencing fiber tear failure within the composite. High magnification assessment showed shear cusps and hackle formations at the fibers, demonstrating brittle shear failure.

6.3. Blade Manufacturing

Having developed a suitable VARTM process for flat panel trials and establishing the adhesive joint performance, a full-scale blade was produced as a proof-of-concept. The VARTM process was adopted for the pressure and suction sides of the blade shells with minimal modifications to the underlying flat panel procedure, confirming the suitability of the infusion layout proposed by Broad [97]. Processing inconsistencies during the blade infusion trials were predominantly observed around the root of the blade due to the complexity of the blade root geometry. Thus, the fabric layers were cut to enhance drapeability while retaining structural performance via overlapped reinforcement strips. With careful consideration for fabric drapeability and mold conformity, laminate compaction was improved, lowering the void content of the parts and enabling the production of high-quality blade shells.

Due to the geometry of the blade shells, the leading edge of the blade was not conducive to structural adhesive joining. The angle created by the pressure and suction surface geometries meant that the thickness of the composite shells was used as the bonding surface, contributing to incomplete polymerization of the adhesive characterized by large cracks and voids. Conversely, the trailing edge of the adhesive formed a sufficiently large bonding surface area.

Production of a blade shell with an optimized stacking sequence was not completed during this thesis. Thus, the mechanical properties of the blade shells are not representative of an optimized design for the expected service conditions. Additionally, the structural reinforcement of the blade was not investigated, and a hollow small blade structure may be susceptible to higher deflection than a blade structure with reinforcement within the internal cavity, as shown by Veludurthi et al. [119]. Kong et al. observed that a foam core structure can supply sufficient structural support even if traditional web and spar structures cannot be placed within small blade cavities [120]. Thus, a

potential solution for structural blade reinforcement after adhesive bonding is an expanding foam, provided that the foam is compatible with a thermoplastic resin system (for instance, polyurethane). Verification of full-scale blade performance should be performed in future work.

Chapter 7: Conclusions

The goal of this thesis was to develop a cost-effective manufacturing process for micro-generating wind turbine blades consisting of a glass fiber unidirectional non-crimp fabric (UD-NCF) reactive thermoplastic composite material system. Vacuum-assisted resin transfer molding (VARTM) processes were used to produce blade shells that were subsequently assembled via adhesive joining. To ensure that the underlying VARTM process was sound, a reliable manufacturing process for flat panels was first developed. The key findings from the flat panel manufacturing process are listed below.

- The inclusion of pleats in the VARTM setup yielded the greatest increase in part quality and repeatability by allowing the vacuum bag to conform to the mold and ensure that the laminate was compacted tightly, with proper fiber nesting.
- Spiral line tubing allowed increased control of the resin flow prior to the penetration of the laminate stack, preventing resin starvation.
- The orientation of the high permeability distribution media had a significant effect on infusion time and part quality.
- The efficiency of the vacuum pump influenced part quality significantly.
- Acid digestion was incapable of providing a reliably quantitative marker for fiber volume fraction, V_f, and void volume fraction, V_c, measurements.

Mode I and Mode II adhesive tests were performed to characterize the bond strength during assembly with the relevant findings listed below.

- Double-cantilever beam (DCB) testing showed that the MMA adhesive transitioned from highly ductile cohesive failure at room temperature to brittle cohesive failure at low temperature. At room temperature (RT), the adhesive sustained higher loads with thicker bond-lines. The low temperature (LT) fracture surfaces exhibited a distinct oscillatory crack propagation pattern, implying that the disparity in thermal expansion coefficients between the adhesive and substrate were inducing residual stresses in the adhesive layer.
- End-notched flexural (ENF) testing showed that the methacrylate adhesive transitioned from highly ductile cohesive failure at RT to brittle substrate failure at LT. The RT load-displacement curves showed that the adhesive could sustain higher loads at thicker bond-

lines. The LT load-displacement curves failed in the elastic region with a higher elastic stiffness than the RT specimens. The LT specimens experienced fiber-tear failure, indicating that the specimen failure was within the substrate and may have been caused by residual stresses during cooling.

- RT-DCB tests conducted with an epoxy instead of methacrylate adhesive showed that the lower surface energy and reactivity of a thermoplastic composite required a specialized adhesive formulation; otherwise, the adhesive would fail at the substrate interface.

Combining all the studies to complete the full assembly of the micro-generating turbine blade, the following conclusions were made.

- The fabric layup and conforming the laminate along the geometry of the mold was critical for ensuring a high-quality blade infusion. Cut lines were incorporated for each fabric layer and with additional reinforcement strips to the UD-NCF fabric to conform to sharp geometries without causing resin pooling and weakening the shell structure.
- Bonding the leading edge of the blade would require significant revisions to the mold to allow the blade shells to create a structural bond. The concavity of the blade shells meant that the shells could only mate along the thickness of the composite, creating a weak bond with significant cracks and porosities in the adhesive layer.

7.1. Recommendations for Future Work

Recommendations for the flat panel processing include:

- Investigating the void content of the samples using a dedicated computer tomography (CT) scanner to quantifiably determine the quality of the manufacturing process. If the void content can be accurately characterized, trials with a degassing chamber should be repeated to investigate if resin degassing prior to infusion would decrease the V_C of the panels.
- Future vacuum infusion trials should use a non-veiled fabric with a lower areal density to determine if the theoretical increase in drapability translates to a higher V_f. The higher areal and linear density of the current non-veiled fabric may increase resistance to compaction and lower V_f. Thus, future tests should investigate a non-veiled fabric with the TEX number and areal weight of the current veiled fabric.

- Trials investigating CAPRI, VAP, or DBVP techniques should be investigated to determine if the V_f can be further increased without negatively affecting the panel quality.

Recommendations for future MMA adhesive testing are shown below:

- The DCB tests should be redone to determine the elastic stiffness of the adhesive. This would allow a comparison between the elastic stiffnesses of the adhesive at varying temperatures during normal loading and allow the MBT method to be applied to the elastic regions of RT and LT samples and provide a direct comparison in fracture toughness.
- A data extraction scheme should be developed for the ENF tests to determine the fracture toughness at RT and LT. This data reduction scheme could either use DIC or adopt one of the effective crack lengths schemed developed in the literature.
- Modifications to the surface treatment method should be investigated (including grit blasting or laser etching) to determine whether there is an impact to the low temperature Mode I and Mode II fracture behaviour.

Recommendations for the full-scale turbine blade manufacturing are given below:

- Trials should be repeated with an appropriate blade stacking sequence instead of the $[0_4]$ sequence used in this study to determine if changes in the fiber orientation would affect the inter- and intra-laminar flow and induce porosities.
- The blade shell molds must be modified to create a bonding surface between the pressure and suction sides along the leading edge. Possible solutions are provided in Appendix A3.
- An alignment tool should be developed to hold the blade shells in the correct alignment during bonding without squeezing the adhesive layer excessively.
- Once the blade assembly has been optimized, and the blades are infused with the correct stacking sequence, stiffness and deflection tests should be performed to benchmark the thermoplastic material system.

References

[1] "Reduce Your Diesel Dependency with a Home Wind Turbine," Borrum Energy Solutions. [Online]. Available: https://borrumenergysolutions.ca/pages/reduce-your-diesel-dependency-with-a-home-wind-turbine

[2] "Clean Energy for Rural and Remote Communities Program," Government of Canada. [Online]. Available: https://natural-resources.canada.ca/reducingdiesel

[3] M. Quitoras, "Rethinking energy policy in Canada's remote communities," Pembina Institute. [Online]. Available: https://www.pembina.org/blog/rethinking-energy-policy-canadas-remote-communities#:~:text=The energy transition in remote,generation from colonial governments and

[4] "Wind explained - Electricity generation from wind," U.S. Energy Information Administration. [Online]. Available: https://www.eia.gov/energyexplained/wind/electricity-generation-from-wind.php

[5] "The Anorra Home Wind Turbine," Borrum Energy Solutions2. [Online]. Available: https://borrumenergysolutions.ca/pages/the-anorra

[6] L. Mishnaevsky, K. Branner, H. Petersen, J. Beauson, M. McGugan, and B. Sørensen, "Materials for Wind Turbine Blades: An Overview," *Materials*, vol. 10, no. 11, p. 1285, Nov. 2017, doi: 10.3390/ma10111285.

[7] "Small Wind Guidebook," WINDExchange U.S. Department of Energy. [Online]. Available: https://windexchange.energy.gov/small-wind-guidebook

[8] R. E. MURRAY, D. SWAN, D. SNOWBERG, D. BERRY, R. BEACH, and S. ROONEY, "Manufacturing a 9-Meter Thermoplastic Composite Wind Turbine Blade," in *American Society for Composites 2017*, Lancaster, PA: DEStech Publications, Inc., Nov. 2017. doi: 10.12783/asc2017/15166.

[9] P. Liu and C. Y. Barlow, "Wind turbine blade waste in 2050," *Waste Management*, vol. 62, pp. 229–240, Apr. 2017, doi: 10.1016/j.wasman.2017.02.007.

[10] R. Goseki and T. Ishizone, “Poly(methyl methacrylate) (PMMA),” in *Encyclopedia of Polymeric Nanomaterials*, Berlin, Heidelberg: Springer Berlin Heidelberg, 2015, pp. 1702–1710. doi: 10.1007/978-3-642-29648-2_244.

[11] S. G. Advani and E. M. Sozer, *Process Modeling in Composites Manufacturing*. CRC Press, 2010. doi: 10.1201/b13142.

[12] B. A. Strong, *Fundamentals of Composites Manufacturing - Materials, Methods, and Applications (2nd Edition)*, Second. Society of Manufacturing Engineers (SME), 2008.

[13] K. K. Chawla, *Composite Materials*. New York, NY: Springer New York, 2012. doi: 10.1007/978-0-387-74365-3.

[14] D. S. Cousins *et al.*, “Infusible Thermoplastic Composites for Wind Turbine Blade Manufacturing: Fatigue Life of Thermoplastic Laminates under Ambient and Low-Temperature Conditions,” *Adv Eng Mater*, vol. 25, no. 11, Jun. 2023, doi: 10.1002/adem.202201941.

[15] W. Obande, D. Mamalis, D. Ray, L. Yang, and C. M. Ó Brádaigh, “Mechanical and thermomechanical characterisation of vacuum-infused thermoplastic- and thermoset-based composites,” *Mater Des*, vol. 175, p. 107828, Aug. 2019, doi: 10.1016/j.matdes.2019.107828.

[16] W. D. Callister Jr, “Materials Science and Engineering - An Introduction (5th ed.),” *Anti-Corrosion Methods and Materials*, vol. 47, no. 1, Feb. 2000, doi: 10.1108/acmm.2000.12847aae.001.

[17] D. Snowberg, “IACMI Project 4.2: Thermoplastic Composite Development for Wind Turbine Blades,” Dec. 2021.

[18] M. Bodaghi, C. H. Park, and P. Krawczak, “Reactive Processing of Acrylic-Based Thermoplastic Composites: A Mini-Review,” *Front Mater*, vol. 9, Jun. 2022, doi: 10.3389/fmats.2022.931338.

[19] R. E. Murray, J. Roadman, and R. Beach, “Fusion joining of thermoplastic composite wind turbine blades: Lap-shear bond characterization,” *Renew Energy*, vol. 140, pp. 501–512, Sep. 2019, doi: 10.1016/j.renene.2019.03.085.

[20] D. Wood, *Small Wind Turbines*. in Green Energy and Technology. London: Springer London, 2011. doi: 10.1007/978-1-84996-175-2.

[21] M. Rosso, “Process Development and Characterizaation of Novel VARTM Fiber-reinforced Thermoplastic Composites,” Master’s thesis, Politecnico di Torino, Turin, Italy, 2020.

[22] S. V. Hoa, *Principles of the Manufacturing of Composite Materials*. DEStech Publications, Inc., 2018.

[23] K. van Rijswijk and H. E. N. Bersee, “Reactive processing of textile fiber-reinforced thermoplastic composites – An overview,” *Compos Part A Appl Sci Manuf*, vol. 38, no. 3, pp. 666–681, Mar. 2007, doi: 10.1016/j.compositesa.2006.05.007.

[24] Y. Qin, J. Summerscales, J. Graham-Jones, M. Meng, and R. Pemberton, “Monomer Selection for In Situ Polymerization Infusion Manufacture of Natural-Fiber Reinforced Thermoplastic-Matrix Marine Composites,” *Polymers (Basel)*, vol. 12, no. 12, p. 2928, Dec. 2020, doi: 10.3390/polym12122928.

[25] “Liquid thermoplastic resin for tougher composites.” Arkema, 2021. [Online]. Available: https://www.arkema.com/files/live/sites/shared_arkema/files/downloads/products-documentations/liquid-thermoplastic-resinfor-tougher-composites.pdf

[26] S. V. Lomov, *Non-crimp fabric composites: Manufacturing, properties and applications*. Woodhead Publishing Limited, 2011.

[27] C. D. Rudd, A. C. Long, K. N. Kendall, and C. G. E. Mangin, *Liquid Moulding Technologies Resin Transfer Moulding, Structural Reaction Injection Moulding and Related Processing Techniques*. Woodhead Publishing Limited, 1997.

[28] F. J. Schirmaier, K. A. Weidenmann, L. Kärger, and F. Henning, “Characterisation of the draping behaviour of unidirectional non-crimp fabrics (UD-NCF),” *Compos*

Part A Appl Sci Manuf, vol. 80, pp. 28–38, Jan. 2016, doi: 10.1016/j.compositesa.2015.10.004.

[29] B. Martin, S. Comas-Cardona, C. Binetruy, N. Billon, J.-L. Bouvard, and P. Lucas, "Influence of fabrics' design parameters on the morphology and 3D permeability tensor of quasi-unidirectional non-crimp fabrics," *Compos Part A Appl Sci Manuf*, vol. 90, pp. 470–479, Nov. 2016, doi: 10.1016/j.compositesa.2016.08.013.

[30] S. M. García-Rodríguez, J. Costa, V. Singery, I. Boada, and J. A. Mayugo, "The effect interleaving has on thin-ply non-crimp fabric laminate impact response: X-ray tomography investigation," *Compos Part A Appl Sci Manuf*, vol. 107, pp. 409–420, Apr. 2018, doi: 10.1016/j.compositesa.2018.01.023.

[31] A. Sandoval, "Characterizing the deformation response of a unidirectional non-crimp fabric for the development of computational draping simulation models," Master's thesis, University of Waterloo, Waterloo, Canada, 2020.

[32] K. Bilge, G. Başer, E. Binbir, and M. Papila, "Effect of yarn number on the strength and failure developes of non-crimp glass fiber composites," in *ECCM 2012*, Venice, 2012.

[33] F. J. Schirmaier, D. Dörr, F. Henning, and L. Kärger, "A macroscopic approach to simulate the forming behaviour of stitched unidirectional non-crimp fabrics (UD-NCF)," *Compos Part A Appl Sci Manuf*, vol. 102, pp. 322–335, Nov. 2017, doi: 10.1016/j.compositesa.2017.08.009.

[34] E. Kunze, S. Galkin, R. Böhm, M. Gude, and L. Kärger, "The impact of draping effects on the stiffness and failure behavior of unidirectional non-crimp fabric fiber reinforced composites," *Materials*, vol. 13, no. 13, pp. 1–34, 2020, doi: 10.3390/ma13132959.

[35] S. SCHÄFER, "Investigation of the compaction behavior of uni- and bidirectional non-crimp fabrics," May 2023, pp. 331–338. doi: 10.21741/9781644902479-36.

[36] Z. Yousaf, P. Potluri, and P. J. Withers, “Influence of Tow Architecture on Compaction and Nesting in Textile Preforms,” *Applied Composite Materials*, vol. 24, no. 2, pp. 337–350, Apr. 2017, doi: 10.1007/s10443-016-9554-8.

[37] S. Sharma and D. A. Siginer, “VARTM Process Improvement for Repeatable and Improved Mechanical Properties of Composite Laminates,” in *Volume 9: Heat Transfer, Fluid Flows, and Thermal Systems, Parts A, B and C*, ASMEDC, Jan. 2009, pp. 45–50. doi: 10.1115/IMECE2009-12593.

[38] B. X. Chai *et al.*, “Simulation-based optimisation for injection configuration design of liquid composite moulding processes: A review,” *Compos Part A Appl Sci Manuf*, vol. 149, p. 106540, Oct. 2021, doi: 10.1016/j.compositesa.2021.106540.

[39] C. Polowick, “Optimizing Vacuum Assisted Resin Transfer Moulding (VARTM) Processing Parameters to Improve Part Quality,” Master’s thesis, Carleton University, Ottawa, Canada, 2013.

[40] N. C. Correia, F. Robitaille, A. C. Long, C. D. Rudd, P. Šimáček, and S. G. Advani, “Analysis of the vacuum infusion moulding process: I. Analytical formulation,” *Compos Part A Appl Sci Manuf*, vol. 36, no. 12, pp. 1645–1656, Dec. 2005, doi: 10.1016/j.compositesa.2005.03.019.

[41] M. Haider, P. Hubert, and L. Lessard, “An experimental investigation of class A surface finish of composites made by the resin transfer molding process,” *Compos Sci Technol*, vol. 67, no. 15–16, pp. 3176–3186, Dec. 2007, doi: 10.1016/j.compscitech.2007.04.010.

[42] L. D. Bloom, M. A. Napper, C. Ward, and K. Potter, “A study of the pressure distribution in the hand layup and vacuum bagging processes,” in *ECCM16*, Seville, 2014.

[43] M. Seyednourani, M. Yildiz, and H. S. Sas, “A two-stage optimization methodology for gate and vent locations and distribution media layout for liquid composite molding process,” *Compos Part A Appl Sci Manuf*, vol. 149, p. 106522, Oct. 2021, doi: 10.1016/j.compositesa.2021.106522.

[44] E. Shi and J. Montesano, “A Comparative Study on Mechanical Properties and Failure Mechanisms of a Non-crimp Fabric Reinforced Reactive Thermoplastic Composite Material at Room and Low Temperatures,” *in preparation*.

[45] V. R. Kedari, B. I. Farah, and K. T. Hsiao, “Effects of vacuum pressure, inlet pressure, and mold temperature on the void content, volume fraction of polyester/e-glass fiber composites manufactured with VARTM process,” *J Compos Mater*, vol. 45, no. 26, 2011, doi: 10.1177/0021998311415442.

[46] M. A. Yalcinkaya, E. M. Sozer, and M. C. Altan, “Fabrication of high quality composite laminates by pressurized and heated-VARTM,” *Compos Part A Appl Sci Manuf*, vol. 102, 2017, doi: 10.1016/j.compositesa.2017.08.017.

[47] M. Bodaghi, R. Costa, R. Gomes, J. Silva, N. Correia, and F. Silva, “Experimental comparative study of the variants of high-temperature vacuum-assisted resin transfer moulding,” *Compos Part A Appl Sci Manuf*, vol. 129, p. 105708, Feb. 2020, doi: 10.1016/j.compositesa.2019.105708.

[48] N. Kuentzer, P. Simacek, S. G. Advani, and S. Walsh, “Correlation of void distribution to VARTM manufacturing techniques,” *Compos Part A Appl Sci Manuf*, vol. 38, no. 3, pp. 802–813, Mar. 2007, doi: 10.1016/j.compositesa.2006.08.005.

[49] D. Droste *et al.*, “Investigation of the compaction behaviour of a quasi-unidirectional non-crimp fabric during the vacuum infusion process,” *J Compos Mater*, vol. 56, no. 16, pp. 2509–2524, Jul. 2022, doi: 10.1177/00219983221092011.

[50] V. K. Dhimole, P. Serrao, and C. Cho, “Review and Suggestion of Failure Theories in Voids Scenario for VARTM Processed Composite Materials,” *Polymers (Basel)*, vol. 13, no. 6, p. 969, Mar. 2021, doi: 10.3390/polym13060969.

[51] M. A. Yalcinkaya, E. M. Sozer, and M. C. Altan, “Dynamic pressure control in VARTM: Rapid fabrication of laminates with high fiber volume fraction and improved dimensional uniformity,” *Polym Compos*, vol. 40, no. 6, pp. 2482–2494, Jun. 2019, doi: 10.1002/pc.25130.

[52] S. van Oosterom, T. Allen, M. Battley, and S. Bickerton, “An objective comparison of common vacuum assisted resin infusion processes,” *Compos Part A Appl Sci Manuf*, vol. 125, p. 105528, Oct. 2019, doi: 10.1016/j.compositesa.2019.105528.

[53] W. Li *et al.*, “Process and Performance Evaluation of the Vacuum-Assisted Process,” *J Compos Mater*, vol. 38, no. 20, pp. 1803–1814, Oct. 2004, doi: 10.1177/0021998304044769.

[54] C. Niggemann, Young Seok Song, J. W. Gillespie, and D. Heider, “Experimental Investigation of the Controlled Atmospheric Pressure Resin Infusion (CAPRI) Process,” *J Compos Mater*, vol. 42, no. 11, pp. 1049–1061, Jun. 2008, doi: 10.1177/0021998308090650.

[55] A. Hindersmann, “Confusion about infusion: An overview of infusion processes,” *Compos Part A Appl Sci Manuf*, vol. 126, p. 105583, Nov. 2019, doi: 10.1016/j.compositesa.2019.105583.

[56] J. R. Hutchinson, P. J. Schubel, and N. A. Warrior, “A cost and performance comparison of LRTM and VI for the manufacture of large scale wind turbine blades,” *Renew Energy*, vol. 36, no. 2, pp. 866–871, Feb. 2011, doi: 10.1016/j.renene.2010.07.025.

[57] S. Black, “Reusable vacuum membranes: Coming of age?,” CompositesWorld.

[58] M. A. Sunilpete and R. M. Cadambi, “Development of Cost Effective Out-of-Autoclave Technology – Vacuum Infusion Process with Tailored Fibre Volume Fraction,” *Mater Today Proc*, vol. 21, pp. 1293–1297, 2020, doi: 10.1016/j.matpr.2020.01.165.

[59] M. Amirkhosravi, M. Pishvar, and M. Cengiz Altan, “Fabricating high-quality VARTM laminates by magnetic consolidation: experiments and process model,” *Compos Part A Appl Sci Manuf*, vol. 114, 2018, doi: 10.1016/j.compositesa.2018.09.003.

[60] M. Amirkhosravi, M. Pishvar, and M. C. Altan, “Void reduction in VARTM composites by compaction of dry fiber preforms with stationary and moving magnets,” *J Compos Mater*, vol. 53, no. 6, 2019, doi: 10.1177/0021998318791311.

[61] J. Klingen, *Adhesive Bonding in Five Steps*. Wiley, 2022. doi: 10.1002/9783527832262.

[62] S. Ebnesajjad, *Handbook of Adhesives and Surface Preparation*. Elsevier, 2011. doi: 10.1016/C2010-0-65918-9.

[63] R. Dehaghani, “Experimental and Numerical Assessment of Adhesively Bonded Non-Crimp Fabric Carbon Fiber/Epoxy Composite Joints,” *UWSpace*, 2021, [Online]. Available: http://hdl.handle.net/10012/16937

[64] J. Zhang, M. de Souza, C. Creighton, and R. J. Varley, “New approaches to bonding thermoplastic and thermoset polymer composites,” *Compos Part A Appl Sci Manuf*, vol. 133, p. 105870, Jun. 2020, doi: 10.1016/j.compositesa.2020.105870.

[65] P. Davies, W. J. Cantwell, P.-Y. Jar, P.-E. Bourban, V. Zysman, and H. H. Kausch, “Joining and repair of a carbon fibre-reinforced thermoplastic,” *Composites*, vol. 22, no. 6, pp. 425–431, Nov. 1991, doi: 10.1016/0010-4361(91)90199-Q.

[66] H. Mason, “Surface treatment for adhesive bonding: Thermoset vs. thermoplastic composites,” Composites World. [Online]. Available: https://www.compositesworld.com/articles/surface-treatment-for-adhesive-bonding-thermoset-vs-thermoplastic-composites

[67] W. Brockmann, P. L. Geiß, J. Klingen, and B. Schröder, *Adhesive Bonding*. Wiley, 2008. doi: 10.1002/9783527623921.

[68] A. Baldan, “Adhesively-bonded joints and repairs in metallic alloys, polymers and composite materials: Adhesives, adhesion theories and surface pretreatment,” *J Mater Sci*, vol. 39, no. 1, pp. 1–49, Jan. 2004, doi: 10.1023/B:JMSC.0000007726.58758.e4.

[69] A. Marques *et al.*, “Review on Adhesives and Surface Treatments for Structural Applications: Recent Developments on Sustainability and Implementation for Metal

and Composite Substrates," *Materials*, vol. 13, no. 24, p. 5590, Dec. 2020, doi: 10.3390/ma13245590.

[70] R. E. Murray, S. Jenne, D. Snowberg, D. Berry, and D. Cousins, "Techno-economic analysis of a megawatt-scale thermoplastic resin wind turbine blade," *Renew Energy*, vol. 131, pp. 111–119, Feb. 2019, doi: 10.1016/j.renene.2018.07.032.

[71] W. Obande, C. M. Ó Brádaigh, and D. Ray, "Continuous fibre-reinforced thermoplastic acrylic-matrix composites prepared by liquid resin infusion – A review," *Compos B Eng*, vol. 215, p. 108771, Jun. 2021, doi: 10.1016/j.compositesb.2021.108771.

[72] A. Laganà *et al.*, "Reproducing reality. Recreating bonding defects observed in transparent poly(methyl methacrylate) museum objects and assessing defect formation," *J Cult Herit*, vol. 48, pp. 254–268, Mar. 2021, doi: 10.1016/j.culher.2020.11.002.

[73] L. F. M. da Silva, T. N. S. S. Rodrigues, M. A. V. Figueiredo, M. F. S. F. de Moura, and J. A. G. Chousal, "Effect of Adhesive Type and Thickness on the Lap Shear Strength," *J Adhes*, vol. 82, no. 11, pp. 1091–1115, Nov. 2006, doi: 10.1080/00218460600948511.

[74] E. M. Petrie, "The fundamentals of adhesive joint design and construction," *Metal Finishing*, vol. 106, no. 11, pp. 55–57, Nov. 2008, doi: 10.1016/S0026-0576(08)80314-5.

[75] M. D. Banea and L. F. M. da Silva, "Adhesively bonded joints in composite materials: An overview," *Proceedings of the Institution of Mechanical Engineers, Part L: Journal of Materials: Design and Applications*, vol. 223, no. 1, pp. 1–18, Jan. 2009, doi: 10.1243/14644207JMDA219.

[76] F. J. P. Chaves, L. F. M. da Silva, M. F. S. F. de Moura, D. A. Dillard, and V. H. C. Esteves, "Fracture Mechanics Tests in Adhesively Bonded Joints: A Literature Review," *J Adhes*, vol. 90, no. 12, pp. 955–992, Nov. 2014, doi: 10.1080/00218464.2013.859075.

[77] T. Anderson, *Fracture Mechanics Fundamentals And Applications*, 3rd ed. Taylor & Francis Group, 2005.

[78] "ASTM D5528/D5528M-21 - Standard Test Method for Mode I Interlaminar Fracture Toughness of Unidirectional Fiber-Reinforced Polymer Matrix Composites." ASTM International, 2022. doi: 10.1520/D5528_D5528M-21.

[79] "ASTM D7905/D7905M-19e1 - Standard Test Method for Determination of the Mode II Interlaminar Fracture Toughness of Unidirectional Fiber-Reinforced Polymer Matrix Composites." ASTM International, 2019. doi: 10.1520/D7905_D7905M-19E01.

[80] M. A. S. Santos and R. D. S. G. Campilho, "Mixed-mode fracture analysis of composite bonded joints considering adhesives of different ductility," *Int J Fract*, vol. 207, no. 1, pp. 55–71, Sep. 2017, doi: 10.1007/s10704-017-0219-x.

[81] A. Ferrarese, "DYNAMIC DELAMINATION TESTING OF A COMPOSITE MATERIAL," Master's thesis, Politecnico di Torino, Turin, Italy, 2020.

[82] R. Campilho, J. Ribeiro, R. Rocha, A. Leal, and F. Viana, "Validation of fracture envelopes of structural adhesives for mixed-mode strength prediction of bonded joints," *Frattura ed Integrità Strutturale*, vol. 13, no. 48, pp. 332–347, Mar. 2019, doi: 10.3221/IGF-ESIS.48.32.

[83] J. M. Arenas, J. J. Narbón, and C. Alía, "Optimum adhesive thickness in structural adhesives joints using statistical techniques based on Weibull distribution," *Int J Adhes Adhes*, vol. 30, no. 3, pp. 160–165, Apr. 2010, doi: 10.1016/j.ijadhadh.2009.12.003.

[84] A. D. Crocombe, "Global yielding as a failure criterion for bonded joints," *Int J Adhes Adhes*, vol. 9, no. 3, pp. 145–153, Jul. 1989, doi: 10.1016/0143-7496(89)90110-3.

[85] D. Castagnetti, A. Spaggiari, and E. Dragoni, "Effect of Bondline Thickness on the Static Strength of Structural Adhesives Under Nearly-Homogeneous Shear Stresses,"

J Adhes, vol. 87, no. 7–8, pp. 780–803, Jul. 2011, doi: 10.1080/00218464.2011.597309.

[86] B. Watson, "Characterizing and Modeling the Effects of Mode Mixity and Bond Line Thickness on the Traction-Separation Response of Structural Adhesive Joints," PhD Thesis, University of Waterloo, Waterloo, Canada, 2021.

[87] Z. Jia, G. Yuan, H. Ma, D. Hui, and K. Lau, "Tensile properties of a polymer-based adhesive at low temperature with different strain rates," *Compos B Eng*, vol. 87, pp. 227–232, Feb. 2016, doi: 10.1016/j.compositesb.2015.10.013.

[88] S. Nam, Y. H. Yu, I. Choi, C. S. Bang, and D. G. Lee, "Fracture toughness improvement of polyurethane adhesive joints with chopped glass fibers at cryogenic temperatures," *Compos Struct*, vol. 107, pp. 522–527, Jan. 2014, doi: 10.1016/j.compstruct.2013.08.015.

[89] J. Moller, R. Hunter, J. Molina, A. Vizán, J. Peréz, and L. F. M. da Silva, "Influence of the temperature on the fracture energy of a methacrylate adhesive for mining applications," *Applied Adhesion Science*, vol. 3, no. 1, p. 14, Dec. 2015, doi: 10.1186/s40563-015-0041-5.

[90] C. Chen, H. Li, T. Wang, and L. Wang, "Influence of Structural Configurations on the Shear Fatigue Damage of the Blade Trailing-Edge Adhesive Joint," *Applied Sciences*, vol. 10, no. 8, p. 2715, Apr. 2020, doi: 10.3390/app10082715.

[91] Y. Geng, J. Jiang, and N. Chen, "Local impregnation behavior and simulation of non-crimp fabric on curved plates in vacuum assisted resin transfer molding," *Compos Struct*, vol. 208, pp. 517–524, Jan. 2019, doi: 10.1016/j.compstruct.2018.10.054.

[92] P. Simacek and S. G. Advani, "Desirable features in mold filling simulations for Liquid Composite Molding processes," *Polym Compos*, vol. 25, no. 4, pp. 355–367, Aug. 2004, doi: 10.1002/pc.20029.

[93] F. Sánchez *et al.*, "Fast and reliable gate arrangement pre-design of resin infusion processes," *Compos Part A Appl Sci Manuf*, vol. 77, pp. 285–292, Oct. 2015, doi: 10.1016/j.compositesa.2015.04.018.

[94] M. Seyednourani, M. Yildiz, and H. S. Sas, “A two-stage optimization methodology for gate and vent locations and distribution media layout for liquid composite molding process,” *Compos Part A Appl Sci Manuf*, vol. 149, p. 106522, Oct. 2021, doi: 10.1016/j.compositesa.2021.106522.

[95] M. Mahendran, “An Improved Mouldless Manufacturing Method for Foam-Core Composite Sandwich Structures,” Master’s thesis, Carleton University, Ottawa, Canada, 2010.

[96] M. F. Mohsin, “Process Modeling of Thermoplastic Composites for Wind Turbine Blade,” Master’s thesis, Politecnico di Torino, Turin, Italy, 2021.

[97] A. I. Broad, “Development of Vacuum Assisted Composites Manufacturing Technology for Wind Turbine Blade Manufacture,” Master’s thesis, University of Central Lancashire, Preston, England, 2012.

[98] Arkema, “Liquid thermoplastic resin for tougher composites.” 2021.

[99] P. Khalili, R. Kádár, M. Skrifvars, and B. Blinzler, “Impregnation behaviour of regenerated cellulose fabric Elium® composite: Experiment, simulation and analytical solution,” *Journal of Materials Research and Technology*, vol. 10, pp. 66–73, Jan. 2021, doi: 10.1016/j.jmrt.2020.12.024.

[100] Y. Suzuki, D. Cousins, J. Wassgren, B. B. Kappes, J. Dorgan, and A. P. Stebner, “Kinetics and temperature evolution during the bulk polymerization of methyl methacrylate for vacuum-assisted resin transfer molding,” *Compos Part A Appl Sci Manuf*, vol. 104, pp. 60–67, Jan. 2018, doi: 10.1016/j.compositesa.2017.10.022.

[101] R. E. Murray *et al.*, “Manufacturing and Flexural Characterization of Infusion-Reacted Thermoplastic Wind Turbine Blade Subcomponents,” *Applied Composite Materials*, vol. 26, no. 3, pp. 945–961, Jun. 2019, doi: 10.1007/s10443-019-9760-2.

[102] A. S. Verma, N. P. Vedvik, Z. Gao, S. G. P. Castro, and J. J. E. Teuwen, “Bondline Thickness Effects on Damage Tolerance of Adhesive Joints Subjected to Localized Impact Damages: Application to Leading Edge of Wind Turbine Blades,” *Materials*, vol. 14, no. 24, p. 7526, Dec. 2021, doi: 10.3390/ma14247526.

[103] M. G. Droubi, C. Fosbrooke, J. McConnachie, and N. H. Faisal, “Indentation based strength analysis of adhesively bonded leading-edge composite joints in wind turbine blades,” *SN Appl Sci*, vol. 1, no. 7, p. 691, Jul. 2019, doi: 10.1007/s42452-019-0735-6.

[104] M. Mahran Kasem, “On the Design and Manufacture of Wind Turbine Blades,” in *Wind Turbines - Advances and Challenges in Design, Manufacture and Operation*, IntechOpen, 2022. doi: 10.5772/intechopen.104490.

[105] “Textile Structure 7003677 Technical Datasheet,” *Saertex*.

[106] C. A. Escalante-Velázquez, S. M. A. Jiménez, S. Piedra, and S. Ledesma, “Experimental Characterization of the Effect of a Spray Adhesive on the Velocity of Impregnation of a Resin on Carbon Fiber Fabrics Utilizing the VARTM Manufacturing Technique,” *Fibers and Polymers*, vol. 23, no. 2, pp. 478–487, Feb. 2022, doi: 10.1007/s12221-021-0363-9.

[107] F. Helber, M. Szcesny, S. Carosella, and P. Middendorf, “ENHANCEMENT ON AUTOMATED PREFORMING FOR COMPOSITE STRUCTURES,” in *ICCM22*, Melbourne, Australia, 2019.

[108] M. Afendi, W. M. Banks, and D. Kirkwood, “Bubble free resin for infusion process,” *Compos Part A Appl Sci Manuf*, vol. 36, no. 6, pp. 739–746, Jun. 2005, doi: 10.1016/j.compositesa.2004.10.030.

[109] S. van Oosterom, A. Schreier, M. Battley, S. Bickerton, and T. Allen, “Influence of dissolved gasses in epoxy resin on resin infusion part quality,” *Compos Part A Appl Sci Manuf*, vol. 132, p. 105818, May 2020, doi: 10.1016/j.compositesa.2020.105818.

[110] C. Rogers, “Introduction to Vacuum Infusion,” Explore Composites. [Online]. Available: https://explorecomposites.com/articles/lamination/introduction-to-vacuum-infusion/#:~:text=Vacuum infusion works because resin,out from under your bag.

[111] Bostik S.A., “Bostik FIT30 45 TWO COMPONENT METHACRYLATE ADHESIVE - Safety Datasheet.” 2021.

[112] P. Gálvez, R. Carbas, R. Campilho, J. Abenojar, M. Martínez, and da S. LFM, "Fracture toughness in Mode I (G IC) for ductile adhesives," *J Phys Conf Ser*, vol. 843, p. 012008, May 2017, doi: 10.1088/1742-6596/843/1/012008.

[113] D. Brown, W. Christian, and R. M. Hanson, "Tracker Video Analysis and Modeling Tool." Free Software Foundation, Inc., 2023.

[114] B. Chen and D. A. Dillard, "The effect of the T-stress on crack path selection in adhesively bonded joints," *Int J Adhes Adhes*, vol. 21, no. 5, pp. 357–368, Jan. 2001, doi: 10.1016/S0143-7496(01)00011-2.

[115] S. Omairey, N. Jayasree, and M. Kazilas, "Defects and uncertainties of adhesively bonded composite joints," *SN Appl Sci*, vol. 3, no. 9, p. 769, Sep. 2021, doi: 10.1007/s42452-021-04753-8.

[116] H. Jin, K. Nelson, B. Werner, and T. Briggs, "Mechanical Strength of Composites with Different Overlap Lengths," *Sandia National Laboratories*, 2018.

[117] O. Falcó, J. A. Mayugo, C. S. Lopes, N. Gascons, and J. Costa, "Variable-stiffness composite panels: Defect tolerance under in-plane tensile loading," *Compos Part A Appl Sci Manuf*, vol. 63, pp. 21–31, Aug. 2014, doi: 10.1016/j.compositesa.2014.03.022.

[118] J. Tang *et al.*, "Staggered ply discontinuities for tailoring the tensile behavior of hybrid carbon fiber/self-reinforced polypropylene composites: A study of pattern parameters," *Compos Part A Appl Sci Manuf*, vol. 125, p. 105551, Oct. 2019, doi: 10.1016/j.compositesa.2019.105551.

[119] A. Veludurthi and V. Bolleddu, "Evaluation of Small Wind Turbine Blades with Uni-Vinyl Foam Alignments Using Static Structural Analysis," *Energy Engineering*, vol. 117, no. 4, pp. 237–248, 2020, doi: 10.32604/EE.2020.011304.

[120] C. Kong, S. Choi, H. Park, and S. Kim, "Design of Foam Core Sandwich Composite Blade for A Small Scale Wind Turbine System Considering Fatigue Life," in *ICCM17*, Edinburgh, 2009.

[121] P. U. Haselbach and K. Branner, “Effect of Trailing Edge Damage on Full-Scale Wind Turbine Blade Failure,” in *ICCM International Conferences on Composite Materials*, Copenhagen, 2015.

[122] B. K. Edwards, “Composite Manufacturing of Small Wind Turbine Blades - Utility Scale Methods Applied to Small Wind,” Master’s thesis, California Polytechnic State University, San Luis Obispo, United States, 2009.

Appendix A1

The step-by-step acid digestion process is outlined below:

1. Approximately 1” x 1” specimen was cut from a panel using a wet saw.
2. The length and width of the specimen was measured using Vernier calipers at 3 locations per dimension. The thickness of the specimen was measured using a Mitutoyo micrometer at 9 locations. The averaged values for each dimension were used to compute the sample volume.
3. The weight of the specimen was measured to the nearest 0.0001g using a Sartorius CP 124 S balance.
4. $75mL$ of nitric acid was poured into a beaker and heated via hot plate to 80°C to avoid excessive off-gassing and spills from bubbling. The nitric acid was placed under a vent throughout the acid digestion process.
5. The specimen was placed in the beaker and mixed with a glass stir stick for 10 minutes to begin breaking down the acrylic matrix. Near the end of the stirring procedure, the resin started to exhibit a slightly gelatinous consistency.
6. The specimen was allowed to sit in 10-minute intervals and then stirred for 1-minute. This procedure was repeated for 3 hours until the fibers were freed from the matrix suspension. For UD-NCF fabrics with a veil that did not decompose in the nitric acid, one layer of the veil was recovered from the laminate and placed on the edge of the beaker. This piece of the veil was used to calculate the total veil mass for the 4-layer specimen to avoid overestimating the V_f.
7. After 3 hours in the acid bath, the contents of the beaker were poured through a filter, allowing the residual acid to be drained from the fibers. Once the acid was drained, distilled water was drained through the filter to clean the fibers.
8. The fibers were placed in an oven at 100°C for 30 minutes to dry the fibers from any residual water.
9. The dried fibers and the recovered veil were separately measured on the mass scale to 0.0001g. The measured mass of the veil was subtracted from the measured mass of the fibers to calculate the net mass of the fibers within the sample.

Recall Equation 1 that described the method for computing V_f. V_c could be computed using the following algorithm. First, the theoretical volume of the matrix $V_{m\,th}$ was computed as:

$$V_{m\,th} = V - V_f, V_f = \frac{M_f}{\rho_f}$$

(9)

where V was the initial volume of the specimen. Then, the mass of the resin M_m was:

$$M_m = M_i - M_f$$

(10)

Then, the volume of the matrix could be computed using the density of the Elium® matrix listed in Table 3-1 as:

$$V_m = \frac{M_m}{\rho_m}$$

(11)

The total volume of the voids in the specimen was computed as:

$$V_v = V_{m\,th} - V_m$$

(12)

Thus, the V_c as a percentage of the specimen volume could be computed as:

$$V_c = \frac{V_v}{V} \cdot 100$$

(13)

Appendix A2

The step-by-step grinding and polishing process is outlined below:

1. An approximately 1” x 1” specimen was cut from a panel using a wet saw. The specimen was divided in two along the diagonal to allow a transverse and longitudinal view of the fiber tows under the microscope.
2. The surfaces of the specimen were adjusted with a rotary grinder until the specimen halves stood upright without any tilting. This ensured that the specimen was perfectly square prior to cold mounting.
3. Each half of the specimen was held in an omega (binding) clip and placed in a silicone mold with 1.25” in diameter. This was the required sample diameter for the semi-auto polishing machine.
4. LECOSET 7008 resin powder and hardener liquid was mixed in a 2:1 weight ratio for 90 seconds under a fume hood. The resin was mixed slowly to avoid bubble formation.
5. Due to the resin cure speed, the resin was poured quickly into the silicone mold under the fume hood. Around 10g of resin were used per mold.
6. The resin was allowed to cure under the fume hood for 1 hour before handling.
7. The demolded specimen contained one surface that may not be smooth. Thus, the rougher top surface was machined on a lathe until it became flush with the bottom surface.

Once the resin was fully cured, the specimen was ready for rotary grinding. Unlike the semi-auto polishing machine that holds the specimen in place at a specified force, rotary grinding was done manually with periodic checks to ensure that the force was evenly distributed across the surface of the specimen to avoid distorting the specimen shape. The rotary grinding table was set at 400rpm, and the specimen underwent 5 passes at gradually increasing sandpaper grits of 180, 320, 400, 600, and 1200. The specimen was wet sanded at each grit for at least two minutes, and the orientation of the specimen relative to the table – either along the width or length of the specimen – alternated between passes. Microscopic analysis between passes confirmed that an even layer of material was removed across the surface.

Once the grinding procedure was completed, the specimen was placed in a Struers Tegramin-20 semi-auto polishing machine. Struers uses default polishing schedules for a variety of common

material types. For a GFRP, the regular CFRP polishing schedule was sufficient, and required the following 2-step procedure:

1. The specimen was held with 25N of load on the Struers Dac pad with a Diap and Dac3 suspension for 3 minutes. The table and specimen cartridges were co-rotated at 150rpm.
2. The specimen was held with 25N of load on the Struers Nap pad with a Diap and Nap-B1 suspension for 1 minute. The table and specimen cartridges were co-rotated at 150rpm.

Appendix A3

Taking inspiration from the literature, solutions to the poor joint fitment at the leading edge of the blade are proposed in this section. Since the mold was originally designed for an autoclave process with prepreg fabrics wrapped around a CNC foam core, optimization of the adhesive bonding surface geometry was not a preliminary requirement for the mold design. Making use of the findings from the DCB and ENF experimental adhesive trials, a redesigned lap joint should prioritize a flange overlap width of around 1" along the entire edge of the blade shells. Due to the aerodynamic profile of the blade, the geometry of the trailing edge naturally lends itself to adhesive bonding, and the requisite 1" flange width could be accomplished by grinding the internal geometries of the shells [121]. The geometric comparisons between the leading and trailing edges were demonstrated in Figure 5.9.

Unlike small-scale blades, industrial-scale blades can take advantage of root and spar structures that provide additional structural support to the blade shell adhesive joints [104]. Edwards acknowledged the geometric limitations of a small wind turbine blade by developing a two-part mold that allowed one of the shells to be directly infused with a flange lip for adhesive bonding [122]. Similarly, Wood recommended the use of a glue dam for small-scale blades to allow a single strap joint configuration on the leading edge [20]. Thus, various manufacturing solutions will be proposed for improving the blade shell adhesive bonding surfaces. There are two regions of the blade where the geometry of the shell edges created an insufficient lap joint: the leading edge, and the base of the blade that sweeps from the cylindrical root to the trailing edge. These regions are highlighted in Figure A3.1.

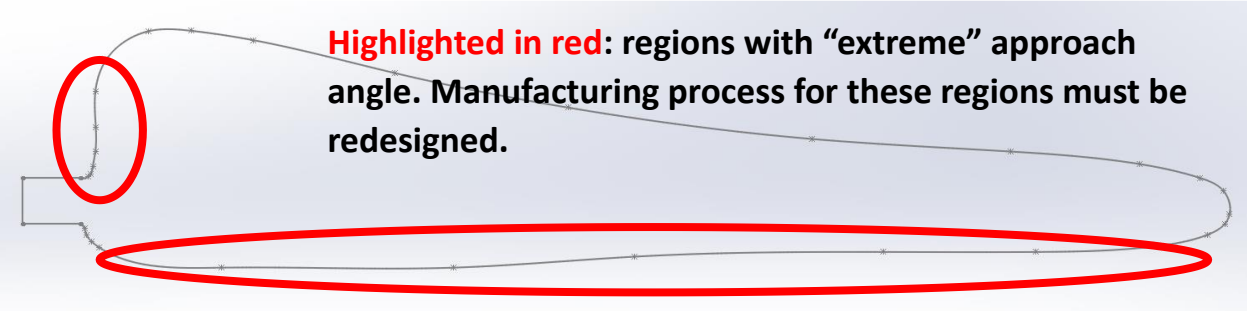


Figure A3.1: Regions of the blade with an extreme approach angle that require a redesigned assembly procedure.

The first solution proposed that the leading edge of the blade shell receive additional fabric reinforcement to increase the localized thickness and form a structural butt joint. The blade shell thickness with 4 layers of fabric was 2.6mm; to achieve the target joint width of 1," the localized thickness along the leading-edge would have to increase by a factor of ten. This solution would be comparatively easy to implement since the current mold would not require any modifications to accommodate the new joint geometry. However, manufacturing precision would be greatly affected as the leading-edge dimensions would be heavily reliant on the skills of the operator. At best, the procedure would require significant grinding after demolding to ensure that the shells are flush with each other; at worst, the operator might fabricate an insufficiently thick bonding surface, rendering the part out-of-specification. Additionally, increased shell thicknesses risk void formation during the infusion. A schematic of the first solution is shown in Figure A3.2.

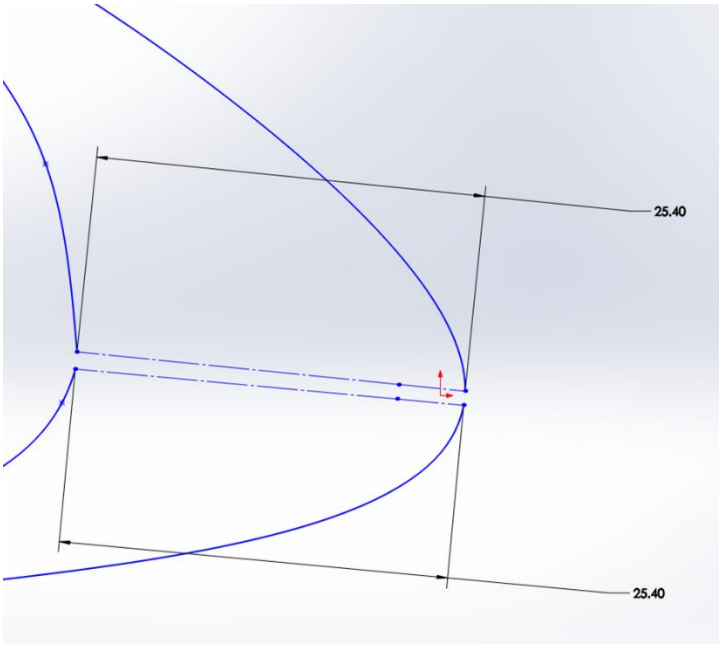


Figure A3.2: Solution #1 to improve the leading-edge bonding surfaces proposes additional fiber reinforcement near the leading edge to physically increase the localized thickness of the shell.

The second solution was inspired by the bonding solution described by Edwards, who proposed converting one of the blade shell molds into a multi-piece tool allowing the bonding flange to be infused directly [122]. Edwards paired this infusion solution with a wooden alignment fixture to precisely bond the adhesive shells together. However, there were drawbacks that limited the feasibility of this method for the current work. Primarily, the creation of an inverted flange effectively rendered the current investigative work for a reliable VARTM process null. The

techniques developed for pleating and layup would need to be revised, and the modified solution would require a longer setup time due to the greater complexity of the part. While the second bonding solution yields greater merit than the first due to the higher projected part quality and consistency, the need for increased operator training during the infusion setup is a net negative. A schematic of the second solution is shown in Figure A3.3.

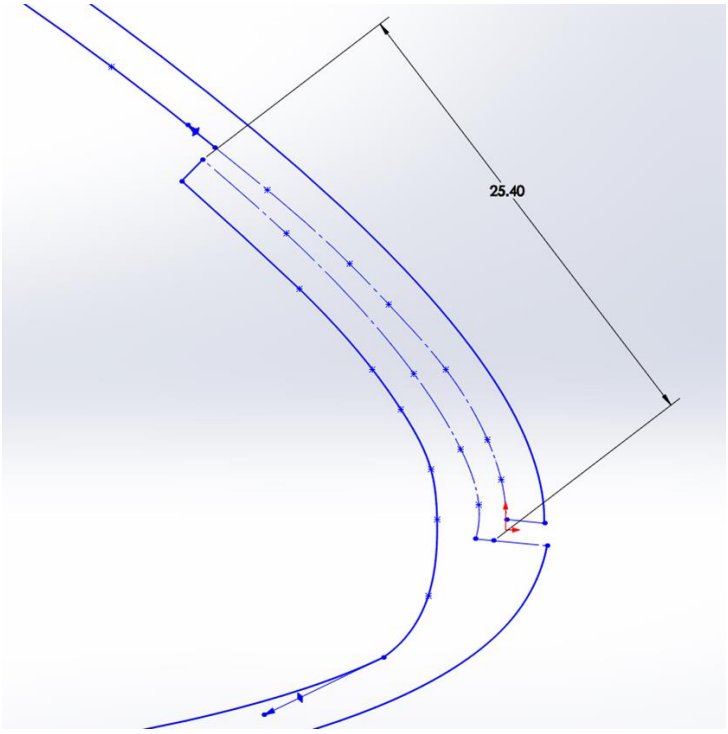


Figure A3.3: Solution #2 to improve the leading-edge bonding surfaces proposes creating a two-part mold for one of the blade shell halves. The flange mold is bolted to one of the rigid molds during the infusion and subsequently removed during demold.

The theoretical problems with the infusion setup posed by the second solution served as an inspiration for the third solution. Instead of infusing the flange lip directly into a shell, the lip would be produced as a separate part and subsequently adhesively bonded to both shells. This approach was inspired by the glue-dam solution proposed by Wood [20]. The ease of implementation of solution three would be a major benefit, since the blade shell infusion procedure would not require any modifications to the process outlined in this work. Furthermore, the mold manufacturing process for the glue dam would be straightforward since the mold cavity could simply be a cut-out of an existing blade. While the third solution might suffer some structural losses compared to the second solution (where the flange is an integrated piece of the blade shell),

the advantages in manufacturing feasibility would be significant. A schematic of the third solution is shown in Figure A3.4.

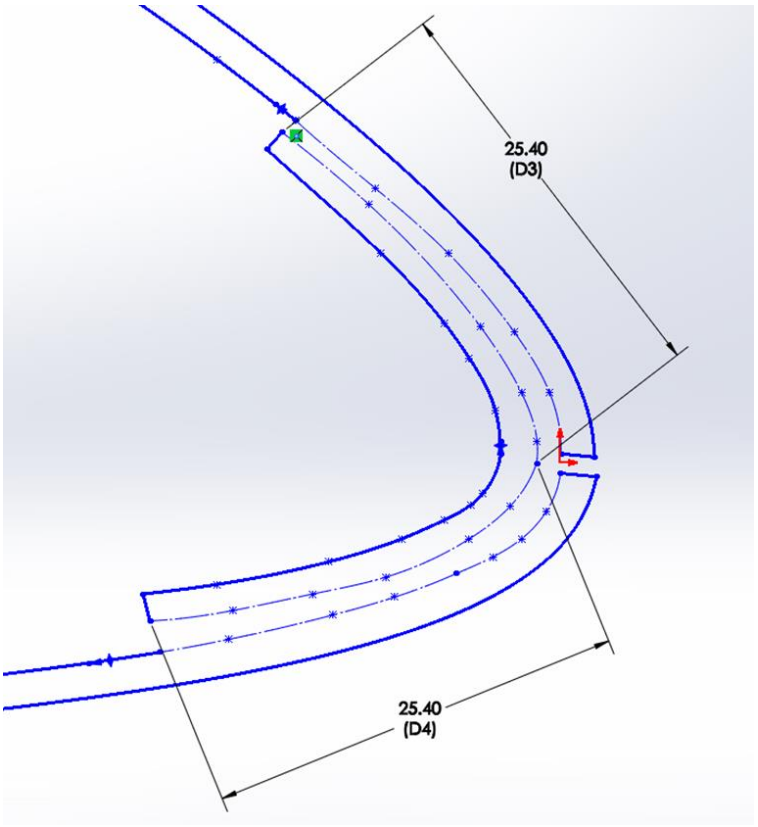


Figure A3.4: Solution #3 to improve the leading-edge bonding surfaces proposes an independently infused flange that is bonded to each shell during assembly (i.e, three separate pieces are created and then assembled).